

# Optimization of Multistage Hydraulic Fracturing Treatment for Maximization of the Tight Gas Productivity

Doctoral Thesis

(Dissertation)

to be awarded the degree

Doctor of Engineering (Dr.-Ing.)

submitted by

Mengting Li, M. Sc.

from Sichuan, China

approved by the Faculty of Energy and Economic Sciences,

Clausthal University of Technology,

Date of oral examination

03 Dec. 2018

#### Dean

Prof. Dr. rer. nat, habil. Bernd Lehmann

<in case: >Chairperson of the Board of Examiners

Supervising tutor

Prof. Dr.-Ing. habil. Michael Z. Hou

Reviewer

Prof. Dr.-Ing. habil. Olaf Kolditz

## Declaration

I hereby	confirm	that I	have	written	this	doctoral	thesis	independently	by myself.	All
informati	on taken f	rom otl	her sou	irces and	l bein	g reprodu	ced in t	his thesis are clo	early referen	ced.
										_
	Date							Nai	me	

#### Acknowledgements

The present work was developed during my work as a research associate in the Department of Energy Resources and Storage of the Energy Research Center Lower Saxony, which is a scientific institution of the Technical University of Clausthal.

For the continuous scientific support and the professional suggestions as well as for the tireless engagement and the utmost care in the editorial revision I would like to thank my supervisor Prof. Dr.-Ing. habil. Michael Zhengmeng Hou. I also would like to thank Prof. Dr.-Ing. habil. Olaf Kolditz for the friendly willingness to take over the correspondence and valuable information on the final design.

I would like to thank all employees in the research group Rock Mechanics for the good cooperation and the friendly support.

Special thanks also to Mrs. Dr. Hedwig Doloszeski (DGMK, Hamburg), Dr. Dominik Soyk (DGMK, Hamburg), Dipl.-Ing. M. Köhler (ENGIE E & P Germany GmbH, Lingen), Dr. med. A. Bencic and Dipl.-Geophys. D. Leuchtmann (DEA German Erdoel AG, Hamburg), Dr. B.C. Seabrook (ExxonMobil Production Germany GmbH, Hanover) for informative discussions and critical reviews.

I also would like to thank my husband, Dr.-Ing. Yang Gou cordially for his all-round support and subject specific advice.

Last but not least, I would like to thank my lovely family in China (especially my grandparents in heaven), for their support and encouragement through all these years.

Clausthal-Zellerfeld, Juni 2018

Mengting Li

#### **Abstract**

Hydraulic fracturing technology is usually required to allow tight gas to escape from the low-permeability reservoir and flow through the wellbore to the surface. So far, there are no numerical tools in the petroleum industry which can optimize the whole process from geological modeling, hydraulic fracturing until production simulation with the same 3D model with consideration of the thermo-hydro-mechanical coupling. In addition, optimization design should be considered from the perspective of production, especially for multiple hydraulic fractures. Thus, the simulation of the production phase with created fractures in one model is very important for the optimization design.

In this dissertation, a workflow and a numerical tool chain were developed for design and optimization of multistage hydraulic fracturing in horizontal well with regard to a maximum productivity of the tight gas wellbore. Frac-Simulator was developed to match the fracturing operation history automatically and optimize the hydraulic fracturing with consideration of thermal effect and gel-breaking. The temperature change will affect the fracture propagation process directly through the thermal stress as well as expansion or shrinkage. The temperature can also influence the fluid properties (gel breaking) as well. In order to maximize the productivity of the above mentioned tight gas wellbore, Frac-Produ Simulator was developed for the simulation of the gas production. The change of stress tensor  $\sigma_{ij}$  and the fracture conductivity  $F_{CD}$  during gas production are also taken into account.

After the verification of the developed Simulators, a full 3D reservoir model is generated based on a real tight gas field in the North German Basin. After the history matching of the stimulation phase, the same 3D reservoir model is generated, including formations and the created fractures with their own fracture geometries and proppant concentration. The bottomhole pressure development derived from the measured treating pressure was used as input data for the stress sensitive reservoir simulation. Through analysis of simulation results, a new calculation formula of  $F_{CD}$  was proposed, which takes the proppant position and concentration into account and can predict the gas production rate of each fracture more accurately. However, not only

F<sub>CD</sub> but also proppant distribution and hydraulic connection of stimulated fractures to the well, geological structure and the interaction between fractures are determinant for the gas production volume of each fracture. Hence, the relationship between gas production rates from each fracture in the later production is different from that at the beginning.

For the sensitivity analysis numerical simulations were carried out with different design parameters, including proppant type, viscosity of the injection fluid and injection time. The results show that the influences of proppant type on fracture geometry and fracture conductivity is much larger than that of the viscosity of the injection fluid, while the influences of the injection time are the smallest. For the optimal fracture treatment design different numerical simulations with varied fracture number/spacing and treatment schedule were performed. The results show that the injection rate is not the higher the better. If it is too high, the fracture width will become wider and the proppant will settle down easier to the bottom, which leads to insufficient hydraulic connection between fracture and wellbore. The fracture spacing should also not be too small, otherwise the influence area/drainage radius is not enough. Thus, there is no unique criterion to determine the optimal number and spacing of the fractures, it should be analyzed firstly in detail to the actual situation and decided then from case to case.

### **Table of contents**

De	clar	atio	on	3
Ac	kno	wle	dgements	iv
Ab	stra	ct		v
Ta	ble	of c	ontents	vii
Lis	st of	figu	ıres	X
Lis	st of	tab	les	xix
1	Int	trod	luction	1
1	l <b>.</b> 1	Mo	tivations and objectives	1
1	1.2	The	esis outline	5
2	Ti	ght	gas field Leer in the North German Basin	9
2	2.1	No	rth German Basin	9
2	2.2	Tig	tht gas sandstone and Rotliegend sandstone	11
2	2.3	His	storical field development	13
3	Fu	nda	mentals of hydraulic fracturing and application in Leer	18
3	3.1	Fra	acturing fluids, well types and fracture orientation	18
3	3.2	Pro	ocedure and stages of hydraulic fracturing	21
3	3.3	Bot	ttomhole pressure record	23
3	3.4	For	rmation characterization	28
	3.4	.1	Well and reservoir testing	29
	3.4	.2	Rock properties from well logs	33
	3.4	.3	Reservoir properties from well logs	46
	3.4	.4	Minifrac test	55
3	3.5	Fra	acture conductivity lab testing	64
4	Me	odel	ing of hydraulic fracturing	67
4	<b>1.</b> 1	His	storical development of hydraulic fracture modeling	68
	4.1	.1	Modelling of penny-shaped fractures	68
	4.1	.2	2D model	70
	4 1	3	Planar 3D and pseudo-3D models	75

4.2	Re	al 3D hydraulic fracture modeling with coupled THM effects	81
4.	2.1	Governing equations for mechanical deformation	82
4.	.2.2	Fracture propagation	85
4.	.2.3	Governing equations for solid-liquid two phase flow in the fracture	87
4.	.2.4	Flow interaction between the fracture and the formation	89
4.	.2.5	Governing equations for the heat transport	90
4.	2.6	Coupled THM effects between each of the processes	92
		opment of the Frac- and FracProdu-Simulator for the optimizate hydraulic fracturing	
5.1	Ü	OO simulator optiSLang	
5.2	Th	e coupled Frac-Simulator optiSLang-FLAC3D <sup>plus</sup>	98
5.3		rification of the Frac-Simulator	
5.	.3.1	Problem definition	99
5.	.3.2	Sensitivity analysis	101
5.	.3.3	Global optimization	103
5.	.3.4	Local optimization	104
5.	.3.5	Check uniqueness of the solution	106
5.4	Re	servoir simulator TMVOCMP	106
5.5	Th	e coupled FracProdu-Simulator optiSLang-FLAC3D <sup>plus</sup> -TMVOCMP	107
5.6	Ve	rification of the developed FracProdu-Simulator	111
5.	.6.1	Sensitivity analysis	112
5.	.6.2	Global optimization	114
5.	.6.3	Local optimization	115
5.	6.4	Check uniqueness of the solution	116
6 C	ptin	nization of the hydraulic fracturing operation in the tight gas re	eservoir
Leer	•••••		118
6.1	Nu	merical simulation of the hydraulic fracturing	118
6.	1.1	Simulation results of frac-stage 1	122
6.	.1.2	Simulation results of frac-stage 2	127
6.	1.3	Simulation results of frac-stage 3	133

6.1	.4	Simulation results of frac-stage 4	138
6.1	.5	Summary	143
6.2	Nu	merical simulation of the gas production	145
6.3	Pro	oposal of a new calculation formula of $\mathbf{F}_{\text{CD}}$	148
6.4	Sei	nsitivity analysis	150
6.4	1.1	Proppant type	150
6.4	1.2	Viscosity of the injection fluid	152
6.4	1.3	Injection time/rate	154
6.4	1.4	Summary	156
6.5	Op	timization of the treatment schedule and fracture number/spacing	156
7 C	oncl	usions and outlook	169
Refere	ence	S	173

# List of figures

Figure 1.1 Natural gas productions by type in the United States, China and Canada, 2012 an	ıd
2040 (EIA 2016)	1
Figure 1.2 Cross-sectional views of the hydraulic fracturing (Economides & Nolte, 2000)	3
Figure 1.3 Flow chart of this thesis	7
Figure 2.1 The North German Basin located in Western Europe, represented as the gree	n
region defined by USGS	9
Figure 2.2 Stratigraphic units of the North German Basin through time (Wikipedia 2017_1) 1	1
Figure 2.3 Conventional, near tight and tight gas sand definition based on the in-sit	tu
permeability (Rezaee et al. 2012)1	2
Figure 2.4 Prospect Location Map: Ostfriesland Licenses & Gas Fields (Koehler 2004) 1	3
Figure 2.5 Gas Field Leer – Structure Map – Top Wustrow-Sandstone (Koehler & Kereke	es:
2006b1	4
Figure 2.6 Target Tight gas bearing in Bahsen- and Wustrow-Member sandstones (Koehle	9 <i>r</i>
2004)	5
Figure 2.7 Leer Z4: Geological W-E-cross section trough the central Leer block with PreSDI	M
seismic (Koehler & Kerekes 2006a)1	6
Figure 2.8 Layout: Frac- and test equipment of Project Leer Z4 (Koehler & Kerekes 2006)	b)
1	7
Figure 3.1 Horizontal and vertical drilling (Crone 2015)	9
Figure 3.2 Fracture orientation: horizontal fracture and vertical fracture as a function of th	e
primary stress state (modified from Martin 2017)2	0
Figure 3.3 Fracture development as function of wellbore orientation (modified from Rahim e	∋t
al. 2012)2	:1
Figure 3.4 Hydraulic fracturing procedure in the reservoir (modified from Tip of the Mi	itt
Watershed Council 2013)2	2
Figure 3.5.4 hottomhole pressure record (Yew & Weng 2015)	<i>1</i>

Figure 3.6 The evolution of the form factor $C_d$ with the entrance erosion (modified from Crump
and Conway 1988)26
Figure 3.7 The fracture twists and turns to consistent with the preferred direction of
propagation (Economides & Nolte 2000)27
Figure 3.8 Nonalignment of perforations and the fracture plane causes pinch points
(Economides & Nolte 2000)
Figure 3.9 Analysis of pressure buildup data on a semi log plot. Arrows denote beginning and
end of semi log linear trends (Economides & Nolte 2000)
Figure 3.10 Log-log plot of pressure buildup data (Economides & Nolte 2000)31
Figure 3.11 Dimensionless type curves of pressure drawdown and pressure derivative for an
infinite-acting reservoir with wellbore storage and skin effect (Bourdet et al., 1983)
Figure 3.12 Radial flow geometries (Economides & Nolte 2000)
Figure 3.13 Porosity-classified logging data together with the field function with parameter
Height above FWL (Koehler 2008)38
Figure 3.14 In-situ Permeability Distribution from Core Data of Rotliegendes sandstones: Lee
Z and other Ostfriesland Wells (Koehler 2008)39
Figure 3.15 Typical variation of relative permeability as a function of water saturation (Dake
1982). S <sub>or</sub> = residual oil saturation
Figure 3.16 Mercury injection capillary pressure functions of different porosity class
Rotliegendes sandstones measured at lab-conditions (Häfner et al. 2006)41
Figure 3.17 Lab-conditions gas-brine relative permeability functions of the different porosity
class Rotliegendes sandstones correlated from mercury injection capillary pressure functions
(Häfner et al. 2006)
Figure 3.18 Correlation between dynamic Young's modulus (E <sub>d</sub> ) and ratio of static/dynamic
Young's modulus (E <sub>s</sub> /E <sub>d</sub> ) test data on sandstones cores (Koehler 2005)
Figure 3.19 Depth-dependent pressure profile with fluid types and fluid contact (Economides
& Nolte 2000)
Figure 3.20 An ideal temperature log (Davis et al. 1997)

Figure 3.21 Stress regimes with spatial distribution of stresses ( $\sigma_0$ = equal-stress constant)
(Economides & Nolte 2000)
Figure 3.22 Comparison of the stress orientation of Leer Z with that in Northern Germany from
world stress map (Heidbach et al. 2016)
Figure 3.23 Stress Direction - Borehole Studies: re-oriented cores investigations and wellbore
breakouts (Koehler 2005)
Figure 3.24 Wireline stress tool (Economides & Nolte 2000)
Figure 3.25 Typical pressure behavior of Minifrac Tests (modified from Fekete Associates Inc.
2012)
Figure 3.26 Pressure and injection rate record obtained into a sand and immediately
underlying shale (Evans et al. 1989)58
Figure 3.27 Typical flow regimes (Fekete Associates Inc. 2012)
Figure 3.28 Pressure decline analysis (Nolte 1982 & 1988a)
Figure 3.29 Flowback and pressure rebound: (a) influence of flowback rate on pressure
response (Nolte 1982 & 1988a) and (b) recommended approach for closure pressure
estimation (Plahn et al. 1997)61
Figure 3.30 A 1 <sup>st</sup> datafrac, a minifrac and a 2 <sup>nd</sup> datafrac for fracture specific data estimation of
frac-stage 1 (modified from Koehler 2005)
Figure 3.31 ISIP and closure pressure estimation of frac-stage 1 (Koehler 2005) 63
Figure 3.32 Conductivity cell stack, from API RP-19D (2008)66
Figure 4.1 Schematic representation of a penny-shaped fracture (Hu & Garagash 2010) 69
Figure 4.2 Schematic representation of a 2D fracture parameters in Eqs. (4.4) to (4.6) (Liu et
al. 2015)70
Figure 4.3 Schematic representation of a PKN fracture (Economides & Nolte 2000)71
Figure 4.4 Schematic representation of a KGD fracture (Economides & Nolte 2000)74
Figure 4.5 Schematic demonstration of the cell-based pseudo-3D fracture geometry (Adachi
et al. 2007)78
Figure 4.6 Definition of variables for the fracture containment problem (modified from

Economides & Nolte 2000)79
Figure 4.7 Schematic demonstration of the fracture geometry based on lumped p3D mode
(Adachi et al. 2007)
Figure 4.8 Demonstration of fracture elements in the geometrical model (left); load condition
in one fracture element at the frozen time point (right) (Zhou et al. 2014)84
Figure 4.9 Classification and geometrical relationship of the fractured elements, partially
fractured elements with the fracture tip and non-fractured elements (modified from Zhou et a
2014)
Figure 4.10 Convective heat exchange between flowing fluid and solid rock formation 92
Figure 4.11 Schematic demonstration of the coupling effects between the sub-processes in
hydraulic fracturing94
Figure 5.1 Basic data flow of optiSLang (Dynardo, 2014)9
Figure 5.2 Flowchart of optiSLang sensitivity analysis (a) and single-objective optimization (b
(modified from Dynardo 2014)98
Figure 5.3 Coupling concept of the simulator optiSLang-FLAC3D <sup>plus</sup>
Figure 5.4 Flowchart of the simulator optiSLang-FLAC3D <sup>plus</sup> for hydraulic fracturing simulation
Figure 5.5 (a) Generic 3D ¼ model for the numerical simulations; (b) Hydraulic fracturing
treatment schedule
Figure 5.6 (a) Fracture geometry by hydraulic fracturing at the end of the injection; (b
Comparison of the evolution of the reference BHP and the simulated one in the sensitivit
analysis102
Figure 5.7 3D plot of single response with respect to the most important variables 103
Figure 5.8 (a) Comparison of the evolution of the reference BHP and the simulated one in the
global optimization; (b) Objective value of the singly simulated optimization design 104
Figure 5.9 (a) Comparison of the evolution of the reference BHP and the simulated one in the
global optimization; (b) Objective value of the singly simulated optimization design 105
Figure 5.10 Optimizer identified design (input) parameters $\mu_0$ and f

Figure 5.11 Parallel coordinates plot of the 58 design simulations in local optimization 106
Figure 5.12 Coupling concept of the simulator optiSLang-FLAC3D <sup>plus</sup> -TMVOCMP
Figure 5.13 Flowchart of the simulator optiSLang-FLAC3D <sup>plus</sup> -TMVOCMP for gas production
simulation
Figure 5.14 Fracture zone Permeability calculation based on superposition
Figure 5.15 The relationship between closure stress and permeability/fracture conductivity
based on the different proppant size (CARBO Ceramics, 2006) 110
Figure 5.16 Coupled THM effects during production simulation (Gou et al. 2014) 110
Figure 5.17 (a) Generic 3D 1/2 model for the numerical simulations; (b) Gas production
treatment schedule and calculated Bottomhole Pressure111
Figure 5.18 (a) Comparison of the evolution of the reference BHP and the simulated one in
the sensitivity analysis
Figure 5.19 3D plot of single response with respect to the most important variables 114
Figure 5.20 (a) Comparison of the evolution of the reference BHP and the simulated one in
the global optimization; (b) Objective value of the single simulated optimization design 115
Figure 5.21 (a) Comparison of the evolution of the reference BHP and the simulated one in
the global optimization; (b) Objective value of the singly simulated optimization design 116
Figure 5.22 Optimizer identified design (input) parameters a
Figure 5.23 Parallel coordinates plot of the 34 design simulations in local optimization 117
Figure 6.1 ½ 3D model geometry and geological stratigraphy
Figure 6.2 Initial stress and pore pressure of 4 fracturing stages
Figure 6.3 Comparison of the calculated BHP from the measured treating pressure and the
simulated during the main fracturing 1
Figure 6.4 Fracture pattern with width distribution (a) and proppant mass distribution pro area
(b) at shut-in ( $t = 80 \text{ min}$ ) and closure ( $t = 1000 \text{ min}$ ) during the main fracturing 1
Figure 6.5 (a) Temporal developments of the fracture half-length and height during the main
fracturing 1; (b) Temporal developments of the fracture and the proppant concentration at
perforation during the main fracturing 1

Figure 6.6 Comparison between FLAC3D <sup>plus</sup> and FracPro by the fracture geometry at shut-in
and closure during the main fracturing 1
Figure 6.7 Comparison of the fracture volume and the injection volume in the main fracturing
during the main fracturing 1125
Figure 6.8 Comparison between FLAC3D <sup>plus</sup> and FracPro by the injection volume, fracture
volume and leak-off at shut-in and closure during the main fracturing 1
Figure 6.9 Fracture pattern with Fluid viscosity (a) and reservoir temperature (b) at shut-in (
= 80 min) and closure (t = 1000 min) during the main fracturing 1
Figure 6.10 Comparison of the calculated BHP from the measured treating pressure and the
simulated during the main fracturing 2
Figure 6.11 Fracture pattern with width distribution (a) and proppant mass distribution pro area
(b) at shut-in ( $t = 87 \text{ min}$ ) and closure ( $t = 650 \text{ min}$ ) during the main fracturing 2
Figure 6.12 Fracture width, proppant volume concentration and proppant mass per unit area
along the fracture length at shut-in ( $z = -4439 \text{ m}$ ) during the main fracturing 2
Figure 6.13 (a) Temporal developments of the fracture half-length and height during the mair
fracturing; (b) Temporal developments of the fracture and the proppant concentration as
perforation during the main fracturing 2130
Figure 6.14 Comparison between FLAC3D <sup>plus</sup> and FracPro by the fracture geometry at shut-
in and closure during the main fracturing 2131
Figure 6.15 Comparison of the fracture volume and the injection volume during the main
fracturing 2131
Figure 6.16 Comparison between FLAC3D <sup>plus</sup> and FracPro by the injection volume, fracture
volume and leak-off at shut-in and closure during the main fracturing 2
Figure 6.17 Fracture pattern with Fluid viscosity (a) and reservoir temperature (b) at shut-in (
= 87 min) and closure (t = 650 min) during the main fracturing 2
Figure 6.18 Comparison of the calculated BHP from the measured treating pressure and the
simulated during the main fracturing 3
Figure 6.19 Fracture pattern with width distribution (a) and proppant mass distribution pro area

(b) at shut-in ( $t = 100 \text{ min}$ ) and closure ( $t = 1000 \text{ min}$ ) during the main fracturing 3
Figure 6.20 Fracture width, proppant volume concentration and proppant mass per unit area
along the fracture length at shut-in ( $Z = -4432m$ ) during the main fracturing 3
Figure 6.21 (a) Temporal developments of the fracture half-length and height during the main
fracturing; (b) Temporal developments of the fracture and the proppant concentration a
perforation during the main fracturing 3136
Figure 6.22 Comparison between FLAC3Dplus and FracPro by the fracture geometry at shut
in and closure during the main fracturing 3136
Figure 6.23 Comparison of the fracture volume and the injection volume in the main fracturing
during the main fracturing 3137
Figure 6.24 Comparison between FLAC3D <sup>plus</sup> and FracPro by the injection volume, fracture
volume and leak-off at shut-in and closure during the main fracturing 313
Figure 6.25 Fracture pattern with Fluid viscosity (a) and reservoir temperature (b) at shut-in (
= 100 min) and closure (t = 1000 min) during the main fracturing 3
Figure 6.26 Comparison of the calculated BHP from the measured treating pressure and the
simulated during the main fracturing 4139
Figure 6.27 Fracture pattern with width distribution (a) and proppant mass distribution pro area
(b) at shut-in ( $t = 110 \text{ min}$ ) and closure ( $t = 740 \text{ min}$ ) during the main fracturing 4
Figure 6.28 (a) Temporal developments of the fracture half-length and height during the main
fracturing; (b) Temporal developments of the fracture and the proppant concentration a
perforation during the main fracturing 4140
Figure 6.29 Comparison between FLAC3Dplus and FracPro by the fracture geometry at shut
in and closure during the main fracturing 414
Figure 6.30 Comparison of the fracture volume and the injection volume during the main
fracturing 414
Figure 6.31 Comparison between FLAC3D <sup>plus</sup> and FracPro by the injection volume, fracture
volume and leak-off at shut-in and closure during the main fracturing 4 142
Figure 6.32 Fracture pattern with Fluid viscosity (a) and reservoir temperature (b) at shut-in (

= 110 min) and closure (t = 740 min)
Figure 6.33 Comparison of the simulated BHP and the BHP derived from the measured
treating pressure
Figure 6.34 The dimensionless fracture conductivity of the main fractures 1 to 4 at closure
Figure 6.35 ½ 3D model geometry and geological stratigraphy including four created fractures
Figure 6.36 Comparison of the simulated gas rate and in-situ measured gas rate 147
Figure 6.37 Comparison of the contribution of each fracture to the total production rate 147
Figure 6.38 Pore pressure distribution in the reservoir near the fractures at $t = 3.5$ a 148
Figure 6.39 Comparison of the contribution of each fracture to the total production rate at the
beginning
Figure 6.40 Comparison of the fracture geometry and volume at closure with three different
types of proppants
Figure 6.41 Comparison of the fracture conductivity contour and derived dimensionless
fracture conductivity (modified) at closure with three different types of proppants
Figure 6.42 Varied viscosity of the injection fluid +50% (Var. 3); -50% (Var. 4)
Figure 6.43 Comparison of the fracture geometry and volume at closure with varied viscosity
of the injection fluid
Figure 6.44 Comparison of the fracture conductivity contour and derived dimensionless
fracture conductivity at closure with varied viscosity of the injection fluid
Figure 6.45 Varied injection time +20 min (Var. 5); -20min (Var. 6)
Figure 6.46 Comparison of the fracture geometry and volume at closure with varied injection
time/rate
Figure 6.47 Comparison of the fracture conductivity contour and derived dimensionless
fracture conductivity at closure with varied injection time/rate
Figure 6.48 Variation of numbers of fracture treatments (3 - 5) and fracture spacing (120 – 169
m) with the corresponding fracture location (e.g. $y = 478$ m) and adopted treatment schedule

(e.g. "Frac-stage 4")	
Figure 6.49 $^{1\!\!/}$ 3D model geometry and geological stratigraphy including created fractures of	
varied fracture spacing and injection volume163	
Figure 6.50 Pore pressure distribution at t=3.5 years by varied fracture number and injection	
volume	

## List of tables

Table 3.1 lab-conditions material parameter of the geo-model for the case study (Ha	ifner et al.
2006)	42
Table 3.2 Parameter of the relative permeability capillary pressure correlation for	mulas for
laboratory conditions	43
Table 5.1 Comparison of the different sensitivity analysis methods	96
Table 5.2 Mechanical and hydraulic properties of the rock formations in the calculat	ion model
	100
Table 6.1 Mechanical and hydraulic properties of the rock formations in the calculat	ion model
	119
Table 6.2 Comparison of F <sub>CD</sub> and initially gas rate	149
Table 6.3 Contribution of each farcture for the total produced gas volume	150
Table 6.4 Variations with varied fracture location (y) and injection volume	158
Table 6.5 Fracture geometry of the basic and varied fracture stimulation	158
Table 6.6 Comparison of the produced gas volume	165

#### 1 Introduction

#### 1.1 Motivations and objectives

Energy is one of the most critical factors for the economic development. Due to the world's increasing energy consumption and the climate change, the strategic energy storage draws a lot of attention (Kolditz et al. 2015). Tight gas has become one of the most important fields in unconventional natural gas exploration and development. Large-scale development and utilization of tight gas in the United States not only boosted the rapid recovery of US natural gas production, but also promoted the progress of tight gas exploration and development in many countries (Figure 1.1). The application of horizontal drilling and hydraulic fracturing technologies made it possible to develop the U.S. tight and shale gas resource, contributing to nearly doubling of the estimates for the total U.S. technically recoverable natural gas resources over the past decade. Tight gas, shale gas, and coalbed methane resources in Canada and China account for about 80% of total production in 2040 in those countries.

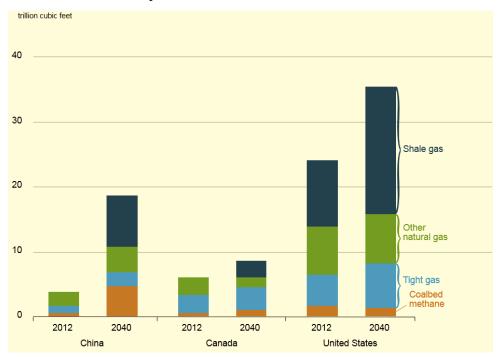


Figure 1.1 Natural gas productions by type in the United States, China and Canada, 2012 and 2040 (EIA 2016)

Tight gas reservoir is known as "tight" because it has a low permeability (less than 0.1 md) and is usually composed of so-called hard rocks like sandstone. Tight gas reservoirs require stimulation because the permeability of the formation is simply not high enough for the well to produce natural gas, of course, taking the economic aspects into account. To increase the wellbore/reservoir connection by means of a high contact area and to enhance the well permeability capacity (net thickness  $\times$  permeability) to a technically possible maximum hydraulic fracture height ( $h_f$ ), hydraulic fracturing (Figure 1.2) is referred to as a suitable reservoir stimulation technique on tight gas reservoirs. Especially under difficult conditions and limited reservoir connection, more obvious on completed horizontal wells, multiple hydraulic fracture treatments were performed to develop an economic well productivity and to access sufficient dynamic gas-in place volumes.

For the hydraulic fracturing treatment design many parameters should be taken into consideration. The main design parameters are treatment schedule (e.g. injection rate/volume/ time, proppant concentration, total injected proppant mass and proppant injection time), fluid properties (e.g. type, density, viscosity and additives), proppant properties (e.g. type, density, diameter, strength and hydraulic conductivity under closure stress) etc. These parameters are determined by geological conditions, rock mechanical and hydraulic properties, temperature, in-situ stress state, reservoir pressure, stress and conductivity requirements etc. Actually, the optimal number and spacing of fracture treatments are based on the reservoir permeability, the length of the well section within the potential layer (distance between the two border fractures), net thickness, fracture half-length, fracture conductivity, the expected compartments (estimated by means of LWD interpretations: sub-seismic faults and/or facies changes), vertical to horizontal permeability anisotropy ( $(k_v/k_h)$ -ratio) and the drainage radius (or assumed reservoir borders) (Koehler & Kerekes 2006a). The optimization can be achieved through numerical simulation.

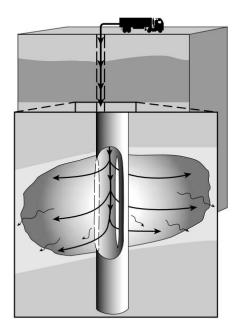


Figure 1.2 Cross-sectional views of the hydraulic fracturing (Economides & Nolte, 2000)

Modern experimental equipment, fast development of computer techniques and the simulation methods make the study of coupled THMC processes possible. Different numerical codes have been developed in recent years, which are able to consider all the process together, such as OpenGeoSys (Kolditz et al. 2012), DuMu<sup>x</sup> (Flemisch et al. 2011), COMSOL Multiphysics (COMSOL 2012) etc. Based on the experimental results and analysis a bank of benchmarks of coupled THMC processes have been set up (Kolditz et al. 2016). Hydraulic fracturing involves many physical processes such as stress change and deformation of rock formation induced by pore pressure change in fractures and pores, fluid flow within fracture and formation including their interactions, fracture propagation, proppant transport and settling inside the fracture. These processes are very complicated, and the mathematical modeling of these Multiphysics processes is a challenging task. From 1950s the first theoretical models of hydraulic fracturing were created and then gradually developed, e.g. KGD (plane strain) (Khristianovic & Zheltov 1955, Geertsma & Klerk 1969) and PKN 2D models (Perkins & Kern 1961, Nordgren 1972), lumped and cell based pseudo 3D models as well as planar 3D model. They were solved by analytical, semi-analytical or fully numerical methods respectively (Adachia et al. 2007, Economides & Nolte 2000, Siebrits & Peirce 2002). However, due to the complexity of the

involved coupled processes as well as the challenges from mathematical modeling of this Multiphysics process, much work is still to be done in the future.

In the petroleum industry there are many standard tools for the design of hydraulic fractures and prediction of gas productions. E.g. reservoir model generation, hydraulic fracturing simulation and gas production simulation are usually carried out using Petrel, FracPro, MFrac as well as ECLIPSE separately. Petrel is a product of Schlumberger, which used to build 3D geological models of petroleum reservoirs (Schlumberger 2014). MFrac used semi-analytic methods and formulated between a pseudo-3D and full 3-D type model with an applicable halflength to half-height aspect ratio greater than about 1/3 (Meyer 1989). MFrac accounts for the coupled parameters affecting fracture propagation and proppant transport (Meyer 2012). However, MFrac does not consider the hydro-mechanical conditions under contact condition after fracture closure. The simulation is forced to stop when the proppant reaches its maximum value of the compacting factor, even when the most upper part of the fracture area is still open without proppant (full closure is not yet reached). That means, the area of the proppant placement is underestimated. In fact, the fluid pressure within the fracture under contact could be smaller than the normal stress perpendicular to the fracture wall. Therefore, it is difficult to simulate the compact proppant at the upper part of the fracture during the closure process. The simulated fracture geometry is too ideal. ECLIPSE is also a product of Schlumberger, which is used to simulate the production of black oil, compositional, thermal, and streamline reservoir. Unfortunately, ECLIPSE can only be used in the reservoir simulation. It is not capable for geomechanical simulation. In ECLIPSE the fracture can only be considered through an equivalent continuum approach and the fracture properties are independent on the stress conditions. So far, there are no numerical tools in the petroleum industry which can optimize the whole process from geological modeling, hydraulic fracturing until production simulation with the same 3D model with consideration of the thermo-hydro-mechanical coupling. There are always conversion and adaption of the results from different stages with different softwares. The optimization of a single fracture during the stimulation phase does not represent the performance of the whole horizontal well. In the petroleum industry, the fractures are normally designed one after another. 3D production simulation will not be performed during this phase. However, the fractures will influence each other during the production. Therefore, optimization design should also be considered from the perspective of production, especially for multiple hydraulic fractures. The simulation of the production phase with the created fractures in one model is very important for the optimization design.

In this dissertation, the complete modeling from multiple hydraulic fractures initiation to production with the same full 3D simulation model, as well as smoothly integration of the simulated multiple fracture geometries and conductivities into production simulation was performed. It was realized based on the hydraulic fracturing model developed by Zhou and Hou (2013), Zhou et al. (2014), Li et al. (2016) and Feng et al. (2016).

The objective of this thesis therefore is the optimization study of tight gas production by using multistage hydraulic fracturing technology based on numerical simulations and the measured data from the tight gas reservoir Leer in the North German Basin.

#### 1.2 Thesis outline

In the framework of this thesis the concept and tools were developed for the optimization study of tight gas production by using multistage hydraulic fracturing technology.

The fundamental of the whole concept was the numerical model for the hydraulic fracturing and the associated reservoir simulation model for the gas production. Such concept was realized by coupling of the previously developed 3D hydraulic fracturing model in FLAC3D<sup>plus</sup>, the multiphase multicomponent flow model in TOUGH2MP, as well as the software optiSLang for sensitivity analysis and robust design optimization. With these tools, 3D simulation model can be generated according to the measured geological and geophysical data of the tight gas field and verified against the measured treatment and production data. Based on the verified models, numerical simulations with varied parameters can be carried out for the optimization of tight gas production regarding the whole process from the beginning of the stimulation until the end of the production.

Figure 1.3 describes the whole concept and flow chart of this thesis. Firstly, the Frac-Simulator FLAC3D<sup>plus</sup>-optiSLang was developed for the history matching of multi-stage hydraulic fracturing phase. Then the FracProdu-Simulator FLAC3D<sup>plus</sup>-TMVOCMP-optiSLang was developed for the history matching of the gas production phase. Both tools were verified by numerical simulation examples. As the case study the natural gas field Leer located in the North German Basin was selected. A full 3D hydraulic fracturing model was generated based on the geological and geophysical data of this gas field. For the stimulation phase, the bottomhole pressure (BHP) development derived from the measured treating pressure (WHP) was set as the goal of history matching. After the history matching a corresponding full 3D reservoir simulation model was generated based on the data from the gas field, including the created hydraulic fractures with their own geometry and proppant distribution obtained during the hydraulic fracturing simulation. For the history matching of the production phase, the bottomhole pressure (BHP) development derived from measured well head pressure (WHP) was used as input data for the stress sensitive reservoir simulation. The gas production rate was set as the goal of history matching. To maximize the productivity of the tight gas wellbore, numerical simulations were carried out with different design parameters, including proppant type (density, diameter as well as stress-dependent conductivity), viscosity of the injection fluid and injection time to obtain their sensitivities. At the last stage, the treatment schedule and fracture spacing were varied based on the history matched model. Various numerical simulations of hydraulic fracturing and subsequent reservoir simulations were carried out for the optimization goal. A new dimensionless fracture conductivity was proposed to better evaluate the hydraulic fracturing treatment results.

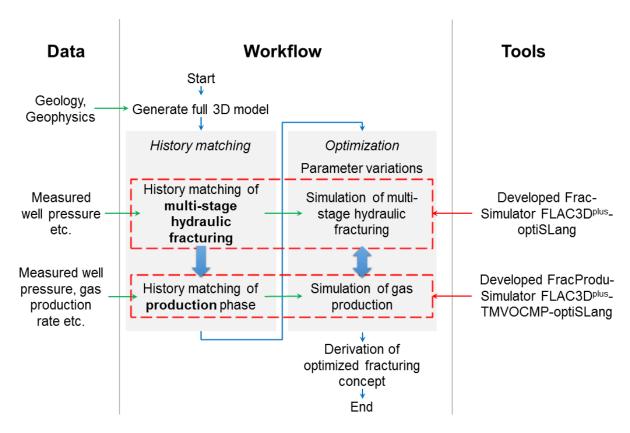


Figure 1.3 Flow chart of this thesis

The following contents are integrated in this thesis.

In Chapter 2, the research location, geological conditions are introduced. The development history, including the drilling of horizontal wells and hydraulic fracturing are reviewed.

Chapter 3 introduces the fundamentals of hydraulic fracturing and application in Leer, such as fracturing fluids, well types and fracture orientation, procedure and stages of hydraulic fracturing, bottomhole pressure record, formation characterization (from well test and well logging) and fracture conductivity lab testing.

In Chapter 4, the historical development of hydraulic fracturing modeling is introduced, e.g. penny-shaped fractures, 2D, planar 3D and pseudo-3D. A real 3D model with FLAC3D<sup>plus</sup> is used as the basic simulator for the numerical simulation in this dissertation.

In Chapter 5, the developed Frac- and FracProdu-Simulators optiSLang-FLAC3D<sup>plus</sup> and optiSLang-FLAC3D<sup>plus</sup>-TMVOCMP for the optimization of multistage hydraulic fracturing treatment were introduced. After the basic introduction, verifications of the simulators were

performed.

In Chapter 6, numerical simulations with the developed simulators were performed for the history matching of the stimulation and production phase. By analyzing and comparing the simulation results, a new calculation formula of dimensionless fracture conductivity F<sub>CD</sub> was proposed for better prediction of the subsequent production phase, which is recommended to use in fracturing treatment design. Based on the history matched stimulation model and production model, sensitivity analysis with consideration of proppant type, viscosity of the injection fluid and injection time/rate, variations of the treatment schedule and fracture number/spacing, were performed to optimize the tight gas production. Then the optimized parameter design was applied for the production in a tight gas reservoir in the North German Basin.

The innovation of this study lies in the following points. On one hand the complete modeling from multiple fractures initiation to production with the same 3D simulation model, as well as the smoothly integration of the simulated multiple fractures geometry and conductivities into production simulation was realized. On the other hand, a new calculation formula of dimensionless fracture conductivity  $F_{CD}$  was proposed for a better fracture treatment design.

#### 2 Tight gas field Leer in the North German Basin

#### 2.1 North German Basin

The North German Basin (Figure 2.1) is a passive-active rift basin located in central and west Europe, lying within the southeastern most portions of the North Sea and the southwestern Baltic Sea and across terrestrial portions of northern Germany, Netherlands, and Poland (Hubscher et al. 2010). The North German Basin is a sub-basin of the Southern Permian Basin that accounts for a composite of intra-continental basins composed of Permian to Cenozoic sediments, which have accumulated to thicknesses around 10–12 kilometers (Scheck & Bayer 1999, Gemmer et al. 2003).

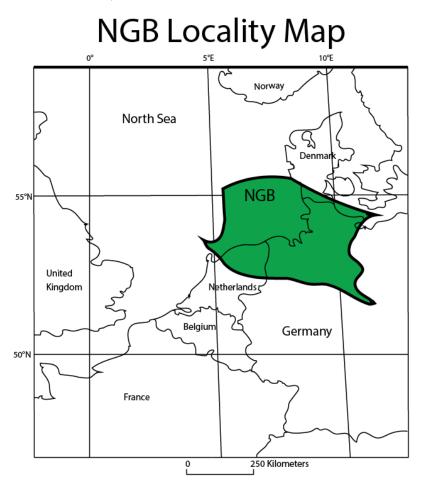


Figure 2.1 The North German Basin located in Western Europe, represented as the green region defined by USGS

The evolution of the North German Basin experienced the following phases: Initial rifting, main phase of subsidence, secondary rifting, doming, tertiary rifting, inversion and final subsidence. The initiation of the Northern German Basin took place in the Late Carboniferous approximately 295-285 Ma (million years ago) in association collapse of the Variscan Orogeny due to wrenching tectonics in the over-thickened crust in the northern foreland of the Variscan Orogeny (Ziegler 1993, Brink 2005, Van Wees 2000). The last phase of subsidence occurred during the Cenozoic.

The stratigraphy sequence of sediments recorded the depositional history of the North German Basin, which make up the basin. The sedimentary basin was assembled above the Lower Paleozoic crystalline basement formed during the Caledonian Orogeny about 420-400 Ma (Sajjad, 2013).

Figure 2.2 breaks down the stratigraphic units of the North German Basin through time. The lowermost stratigraphic unit of the North German Basin is the lower Rotliegend group, which is from Permian of the Paleozoic era and composed primarily ignimbrites, rhyolites, and andesites, while also having minor amounts basalts (George 1993). Rotliegend is also the target formation of the tight gas field Leer, which was studied in this thesis.

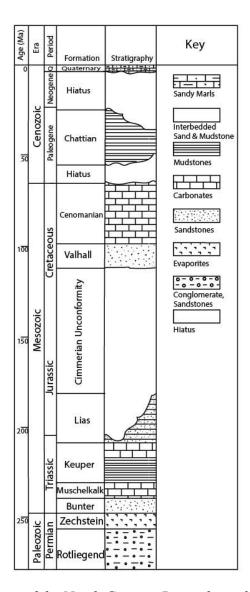


Figure 2.2 Stratigraphic units of the North German Basin through time (Wikipedia 2017 1)

#### 2.2 Tight gas sandstone and Rotliegend sandstone

Currently, most of the natural gas is from suitably porous rocks in conventional reservoirs. The gas flow into the well does not require any extra technological intervention. In tight gas reservoirs, however, the natural gas is in the pore spaces of relatively impermeable sandstone strata (permeability between 0.01 - 0.1 mD and porosity < 10%, Figure 2.3), where it must be "mobilized" before it can be extracted. This is where hydraulic fracturing is used: millimeterthin flow paths, known as fractures, are created in the reservoir by a pressurized liquid. When injection is stopped and hydraulic pressure removed from the well, proppants hold the fractures

open and thus prevent the fractures from closing. This created and propped paths could increase the gas production by many hundreds of percent in some cases.

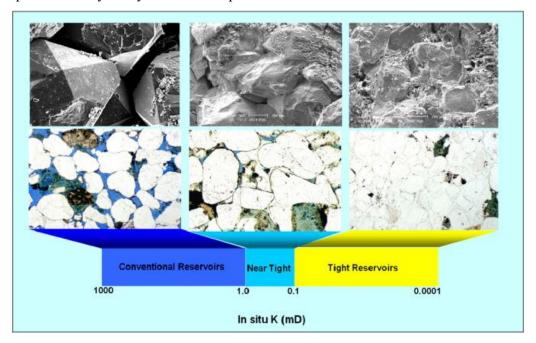


Figure 2.3 Conventional, near tight and tight gas sand definition based on the in-situ permeability (Rezaee et al. 2012)

Rotliegend sandstone is a kind of tight gas sandstone. It is a lithostratigraphic unit of latest Late Carboniferous, the Early Permian, and the Middle Permian to early Late Permian age (STDK 2016). It lies in the subsurface of large areas in Central and West Europe. The Rotliegend mainly consists of sandstone layers and is usually covered by the Zechstein. In the north of Germany and in the Netherlands the Rotliegend is usually subdivided into two groups: A Lower Rotliegend Group (mostly volcanic rocks: tuffs and basaltic lavas) and an Upper Rotliegend Group (sandstones and siltstones).

The structure of the studied natural gas field Leer near the German/Dutch border is in a structural high block, which is located at a depth of about 4400 m TVDss. The gas bearing Upper Rotliegend sandstones are mainly composed of aeolian dunes and sandflat deposits with occasionally interbedded mudflats and sparse fluvial deposits. The depositional setting of the Bahnsen-, Wustrow- and Ebstorf-Member can generally be characterized by a desert plain system (Koehler & Kerekes 2006a).

#### 2.3 Historical field development

The gas reservoir Leer lies in the North German Basin (Figure 2.4). According to Koehler & Kerekes (2006a), the Leer structure is located about 5 km SSE of the city Leer, which belongs to the Ostfriesland trend of the North German Rotliegend Play as well as.

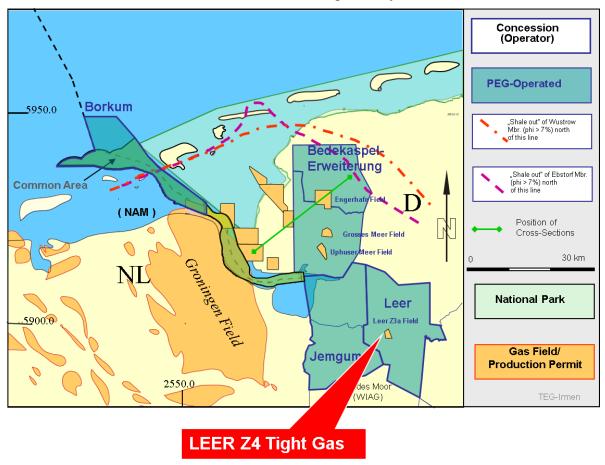


Figure 2.4 Prospect Location Map: Ostfriesland Licenses & Gas Fields (Koehler 2004)

The exploration well Leer Z2 (Figure 2.5) for the gas production was drilled in 1971, which proved gas bearing "tight" sandstones in Bahsen- and Wustrow-Member (Figure 2.6). A dynamic original gas in-place (OGIP) is only 5 Mio. m³ (Vn). So, Leer Z2 well was plugged and abandoned, because it didn't reach an economic production. After that a vertical well Leer Z3 (Figure 2.5) was drilled in 1982. However, it reached the same unsatisfied results. Until 1996 Leer Z3 well produced only 20.4 Mio. m³ (Vn). The well had accessed a dynamic OGIP of 180 - 220 Mio.m³ (Vn). In 1997 the first successful well project was gained by the fracture

stimulated sidetrack Leer Z3a (Figure 2.5) of the prior Leer Z3. It was stimulated by a proppant fracture treatment with 70 tons of CarboProp 20/40. The sidetrack had proven a dynamic OGIP of 600 Mio.m<sup>3</sup> (Vn). But because of the compartmentalization the dynamically allocated OGIP is not sufficient for new conventional vertical stimulated well projects. The positive results of the fracture stimulated sidetrack Leer Z3a actuated the further development of the Leer block to reach more compartments. (Koehler & Kerekes 2006a)

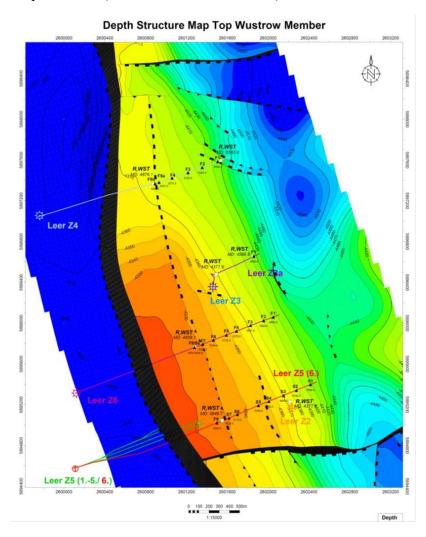


Figure 2.5 Gas Field Leer – Structure Map – Top Wustrow-Sandstone (Koehler & Kerekes 2006b

The target tight gas layer lies in two types of sandstones: Bahsen- and Wustrow-Member (Figure 2.5).

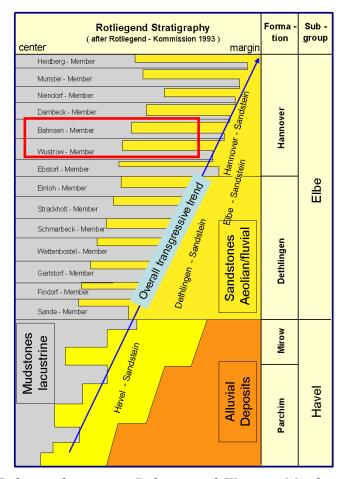


Figure 2.6 Target Tight gas bearing in Bahsen- and Wustrow-Member sandstones (Koehler 2004)

Thanks to the development of the drilling and fracturing technology a horizontal well with multiple transverse fractures were accessed the reservoir in 2005, which was verified by a new seismic survey for the potential Leer Rotliegend structure.

Based on literature studies and experiences of different "tight gas" researches and projects from Germany and other countries, the horizontal well project Leer Z4 (Figure 2.5) was launched. The research object of this dissertation focuses on Leer Z4. To estimate the maximum stress (the PFP direction), re-oriented cores investigations and well breakouts were performed. The NNW-SSE direction of the main stress direction is in accordance to the DGMK study 593-5 (Müller 2004). The horizontal well Leer Z4 was drilled with an Azimuth of 76° in an ENE direction, which is additionally the direction of the maximum wellbore stability.

A 680 m long horizontal well section was drilled at the depth of about 4500 m, which lies in

the Wustrow-Member of the Rotliegend structure in Leer Z4 (Figure 2.7). A large fault was observed at the beginning of the horizontal section of the well through seismic exploration (Figure 2.5). This fault is not permeable and would be regarded as a close boundary during the later gas production.

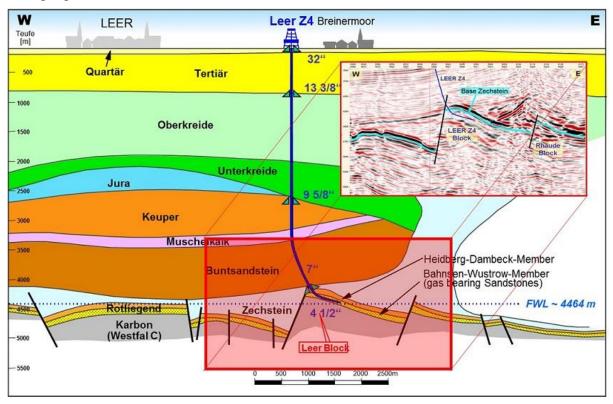


Figure 2.7 Leer Z4: Geological W-E-cross section trough the central Leer block with PreSDM seismic (Koehler & Kerekes 2006a)

Figure 2.8 shows the onsite layout: Frac- and test equipment of Project Leer Z4.

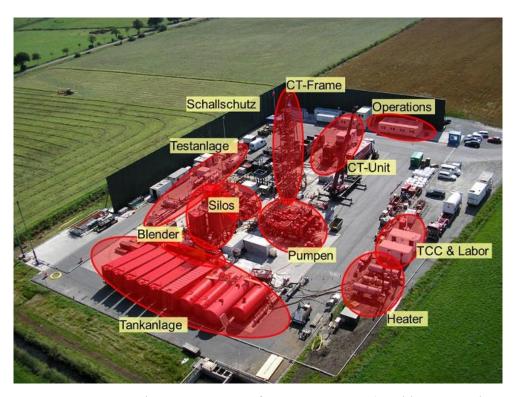


Figure 2.8 Layout: Frac- and test equipment of Project Leer Z4 (Koehler & Kerekes 2006b)

# 3 Fundamentals of hydraulic fracturing and application in Leer

# 3.1 Fracturing fluids, well types and fracture orientation

The typical composition of hydraulic fracturing fluid is about 99.5% water with proppant as well as 0.5% chemicals additives (Ground Water Protection Council 2009, Hartnett-White 2011). The exact formulation varies depending on the well. Proppants, which are granular materials, props the created flow paths, so that they remain open. Typical proppants are silica sand, resin-coated sand, bauxite, and man-made ceramics. The selection of the proppants depends on the formation permeability and required grain strength. If the stress in some formations is great enough to crush the grains of the natural silica sand, higher-strength proppants such as bauxite or ceramics will be used. Silica sand is the most commonly used proppant, though ceramic proppants of uniform size and shape are believed to be more effective. Chemical additives are required to enable the proppants to be carried into the fractures. They thicken the fluid and enable it to transport the filling material (proppants) evenly through the flow paths. Without a carrying fluid, the filling material would immediately sink to the bottom of the well and block the wellbore. The most commonly used chemical additives are gels, gel breakers, biocides, friction reducers, surfactants and salt. Gels make the water more viscous and ensure that filling material such as small ceramic spheres stay suspended instead of just sinking to the bottom. Gel breakers return the water to a more liquid state, so that the fracturing fluid can be pumped back more easily to accelerate the closure process.

For fracture stimulation of Leer Z4 all injected fluids were heated up to about 50° to reduce the completion stress. And 4% KCl was added to the fluids for clay protection. To maintain high fracture conductivity under high closure stress environment high strength sintered bauxite proppants in 20/40 mesh size (CarboHSP 20/40) were applied. The stimulations were performed using a low polymer fracturing fluid for high temperature (150°C) named as Sirocco gels and was provided by the service company Halliburton (Koehler & Kerekes 2006a). The technological breakthroughs in drilling and completion technology made the horizontal

wellbores (Figure 3.1) much more economical since the early 2000s. Particularly in shale formations, which is much deeper (about 2000 m) than conventional gas reservoir and do not have sufficient permeability to produce economically with a vertical well. Horizontal well increased wellbore exposure to formation than conventional vertical wellbores.

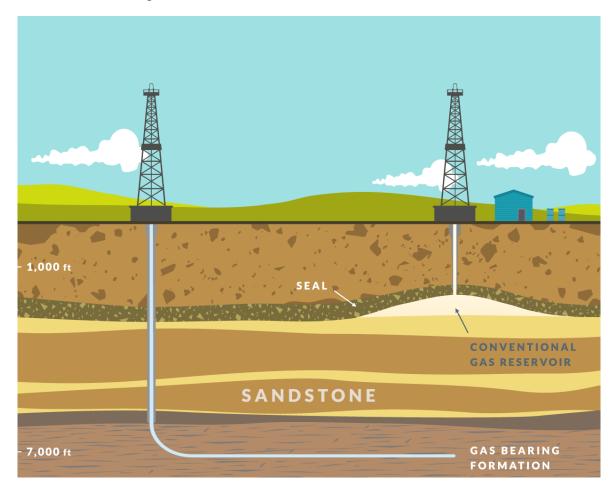


Figure 3.1 Horizontal and vertical drilling (Crone 2015)

Fracture orientation depends on the in-situ stress state of the formation. Hydraulic fractures will always propagate perpendicular to the minimum principal stress. Based on the experience, horizontal fractures will occur at depth less than 600 m because the overburden stress at these depths is the minimum principal stress. In this case, horizontal fractures are formed (Figure 3.2) and fractures are parallel to the bedding plane of the formation.

As depth increases beyond approximately 600 m, overburden stress increases by approximately 0.23 bar/m, making the overburden stress the dominant stress. That means the horizontal

confining stress is now the least principal stress. Since hydraulically induced fractures propagate in the direction perpendicular to the least stress, vertical fractures are formed (Figure 3.2).

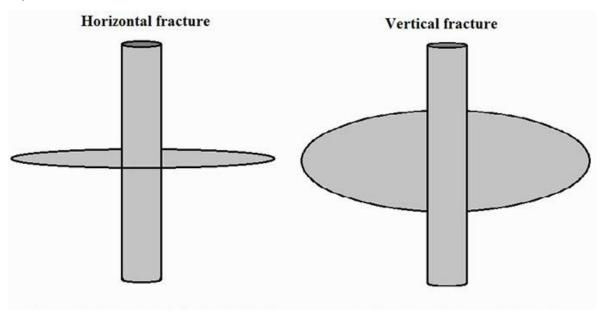


Figure 3.2 Fracture orientation: horizontal fracture and vertical fracture as a function of the primary stress state (modified from Martin 2017)

Besides, the vertical factures development is also depending on the wellbore orientation. If a horizontal well is drilled in the direction of minimal horizontal stress, the fractures created by hydraulic fracturing will be perpendicular to the wellbore. These are transverse fractures. When the well is drilled along the maximal horizontal stress, the fractures created will be parallel to the wellbore. They are longitudinal fractures (Figure 3.3).

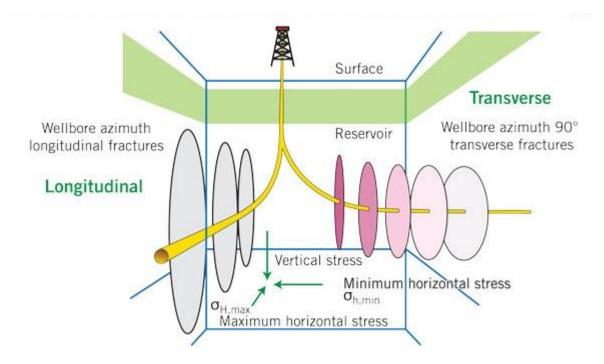


Figure 3.3 Fracture development as function of wellbore orientation (modified from Rahim et al. 2012)

At the same time, the multi-stage and multi-cluster per stage fracture treatments (Figure 3.3) in horizontal wellbores create a large stimulated reservoir volume (SRV) that increases both the production and the estimated ultimate recovery (EUR) (Bruce et al. 2010). It should be noted that each fracture should have sufficient length and conductivity, to maximize the production performance from horizontal wells with multiple fractures. In addition, each fracture needs to be properly cleaned up after the treatment. The interference occurring between fractures should be minimized based on the placement and the total number of the factures. This requires proper fracture treatment design.

# 3.2 Procedure and stages of hydraulic fracturing

The oil and gas industry defines hydraulic fracturing as the actual process of injecting highpressured fluids in underground to create fractures. It is not a part of the drilling process, but a technique used after the well drilling. The procedure of hydraulic fracturing is listed below

# (Figure 3.4):

- 1. Wellbore (vertical or horizontal) drilling till target formation
- 2. Production casing inserted into borehole, then surround with cement
- 3. Casing is perforated blasting with small holes through pipe, cement and formation rock
- 4. After perforation, the well is hydraulically fractured with high-pressured fracturing fluids (water, sand and chemical additives)
- 5. Oil and gas flow back up the pipeline to the wellhead through the sand propped man-made fractures.

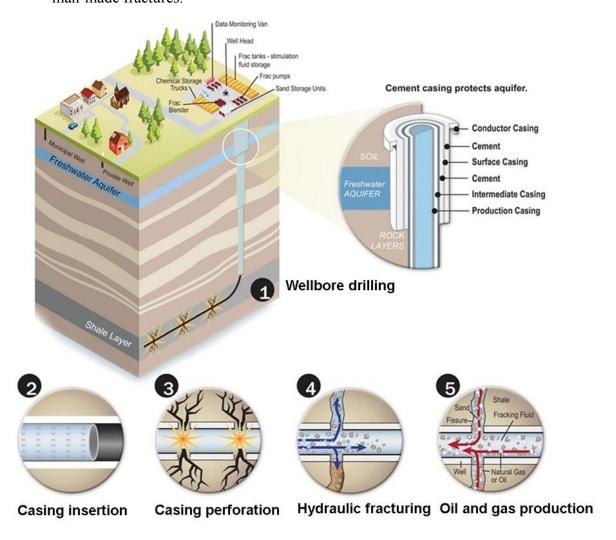


Figure 3.4 Hydraulic fracturing procedure in the reservoir (modified from Tip of the Mitt Watershed Council 2013)

Hydraulic fracturing happens in steps called stages. A typical hydraulic fracture program will follow the stages below.

- 1. Data stage: to estimate the fracture specific data (like closure pressures, friction data and leakoff) all intervals were examined by a Formation Breakdown within a first Data Frac, a Mini Frac and a second Data Frac.
- Pad stage: Approximately hundreds cubic meters of slick water without proppant fills
  the wellbore to break the formation and initiate the hydraulic fracturing of the target
  formation.
- 2. Proppant stage: A mixture of water and proppant (sand, ceramic etc.) is fed into the wellbore. The proppant will be carried by the fracturing fluid into the formation and deposited, to prop the fracture and hold it open once the pressure is reduced.
- 3. Flush stage: A volume of fresh water is pumped down the wellbore to flush out any excess proppant that may be present in the wellbore.

# 3.3 Bottomhole pressure record

When pumping continues, hydraulically induced fracture propagates from the wellbore into reservoir. At the same time, the fracturing fluid leaks off from the fracture into the surrounding rock medium. It is important to observe that the opening of the fracture is maintained by the net pressure (fluid pressure minus the minimum in-situ stress), while the fluid leak-off rate from the fracture is caused by the difference between the fluid pressure and the reservoir pressure. (Yew & Weng 2015)

A typical bottomhole pressure record is illustrated in Figure 3.5. The maximum pressure is named as initial breakdown pressure  $P_b$ . When a fracture is initiated at the borehole surface, the pressure drops but not always in the field. The almost constant pressure is the propagation pressure  $P_{prog}$ , which causes the fracture propagation into the reservoir. The pressure drops immediately after the stop of the pumping due to the vanishing frictional pressure loss, which occurs normally in the pipe and perforation. After that the fluid pressure continues to decrease

slowly to the reservoir pressure due to leak off process. The transition point after pumping is called the shut-in pressure  $P_{\rm si}$  or the instantaneous shut-in pressure, ISIP. However, the fracturing fluid continues to leak off from the fracture surface and the fracture width continues to decrease. This will stop until the fluid pressure inside the fracture reaches equilibrium with the minimum in-situ stress. At this point, the fracture closes and is propped by the proppant. The fracture closure pressure, which can be determined from the pressure decline analysis, is taken as a measure of the minimum in-situ stress.

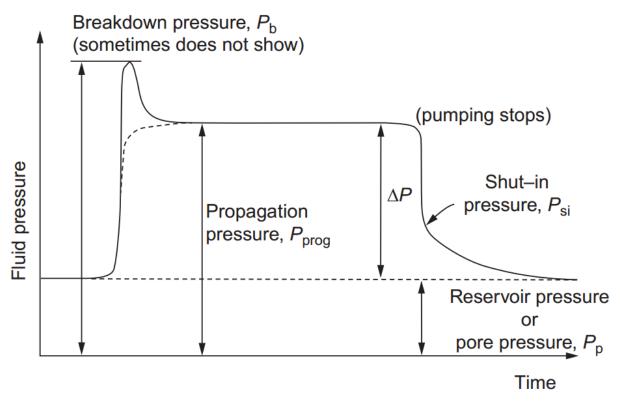


Figure 3.5 A bottomhole pressure record (Yew & Weng 2015)

During the hydraulic stimulation the bottomhole pressure is sum of all the pressure acting on the bottomhole. It is derived from the directly measured well head pressure (WHP) plus the hydrostatic pressure minus the near-wellbore friction pressure loss and fluid flow pressure loss in the wellbore (Eqs. (3.1) - (3.2), Economides & Nolte 2000).

$$BHP = WHP + \rho_{fluid}gh - \Delta p_{near\ wellbore} - \Delta p_{flow}$$
 (3.1)

$$\Delta p_{near\ wellbore} = \Delta p_{Perfo} + \Delta p_{tort} + \Delta p_{misalign}$$
(3.2)

where BHP is the bottom hole pressure [Pa], WHP is the well head pressure [Pa],  $\rho_{fluid}$  is the fluid density [kg/m³], g is the gravitational acceleration [m/s²], h is the true vertical depth [m],  $\Delta p_{near\ wellbore}$  is the near-wellbore friction pressure loss [Pa],  $\Delta p_{Perfo}$  is the perforation friction [Pa],  $\Delta p_{tort}$  is the fracture turning (i.e., tortuosity) friction [Pa],  $\Delta p_{misalign}$  is the perforation misalignment friction [Pa],  $\Delta p_{flow}$  is the fluid flow pressure loss in the wellbore [Pa].

Especially with a well path in the direction of the minimum stress direction, orthogonal to the preferred fracture plain (PFP), transverse fractures will be formed. In this situation the connection area between well and fracture is minimum but crucial. To get a relatively good fracture-to-well contact "big hole"-perforations and high fracture conductivity in the near wellbore environment should be established (Koehler & Kerekes 2006). Romero (1995) has proposed the perforation friction for linear fluids as (Eq. (3.3)):

$$\Delta p_{Perfo} = C_1 \cdot \frac{q_{Injection}^2 \cdot \rho_{fluid}}{n_{Perfo}^2 \cdot C_d^2 \cdot d_{Perfo}^4}$$
(3.3)

Where  $C_I$  is 0.2369 ("oil field"-units) and 2.2446 · 10<sup>8</sup> (for SI-units),  $q_{Injection}$  is the total flow rate [m³/s],  $\rho_{fluid}$  is the fluid density [kg/m³],  $n_{Perfo}$  is the number of effective perforations [-] (from step rate down tests),  $d_{Perfo}$  is the perforation diameter at the casing [m] and  $C_d$  is the Form factor [-] ( $C_d \le 0.89$ ,  $C = 0.56+1.65 \cdot 10^4 \cdot M$ , with M = Proppant quantity, that has passed the perforation, in kg). The Form factor shows the effect of the perforation entrance erosion on the friction pressure (Figure 3.6).

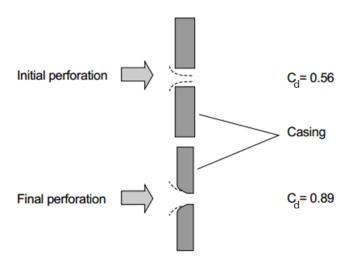


Figure 3.6 The evolution of the form factor  $C_d$  with the entrance erosion (modified from Crump and Conway 1988)

Tortuosity is a rotating channel that connects the wellbore and the main fracture. When the wellbore orientation is not designed properly in the stress field, tortuosity is the main phenomenon affecting the execution of a hydraulic fracturing treatment (Figure 3.7). The fracture width is proportional to the net pressure (difference between the pressure in the fracture and the minimum stress). When the fracture opens, if the stress to prevent it from opening is greater than the minimum in-situ stress, the fracture width becomes smaller than the non-turned fracture. If the ratio of the stress to stop the fracture opening to the minimum in-situ stress is higher than 1.5, then the fracture mouth acts as a nozzle (Economides & Nolte 2000). Although the fluid can flow in, the pressure drop is larger due to the narrowing of the fracturing width at the well. This reduction in fracture width along the reorientation path restrict the fluid flow and may cause near-wellbore sand screen out

S.

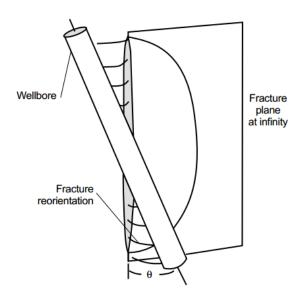


Figure 3.7 The fracture twists and turns to consistent with the preferred direction of propagation (Economides & Nolte 2000)

The perforation design (i.e., hole size, spacing, and orientation) is very different. In fact, there are very few cases in which the perforation is truly consistent with the preferred fracture plane unless detailed work is done on the directions of the stress at a well (Economides & Nolte 2000). Nolte (1988a) pointed out that if the fracture does not initiate at the perforations, the fluid must communicate with the fracture along the narrow channel at the edge of the casing. This will inevitably result in higher treating pressures due to the width restrictions of the fractures (Figure 3.8).

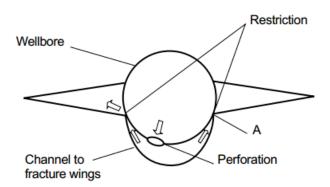


Figure 3.8 Nonalignment of perforations and the fracture plane causes pinch points (Economides & Nolte 2000)

#### 3.4 Formation characterization

The in-situ stress state, especially the minimum in-situ stress is one of the most important parameters in hydraulic fracturing. At typical reservoir depths, the fracturing pressure (fluid pressure inside the fracture) is a strong function of the minimum in-situ stress (or closure stress). The net pressure is the most robust and usually the unique parameter that is available for obtaining information on fracture geometry. An error in closure stress measurement can lead to a significant error in the estimation of the net pressure, and consequently, the fracture geometry. The efficiency of a fracturing treatment is a function of wellbore inclination with respect to the principal stress direction and magnitude (Martins 1992a; Pearson 1992).

In industry, well testing has been used for decades to determine essential formation properties and to assess wellbore conditions. There are many different types of tests that can be utilized to collect this information, depending on the test time, the well location, the well type, and the formation type. Conventional tests (e.g. flow/buildup or injection/falloff) can satisfy the most part of our needs. However, under certain conditions, especially in very low permeable formations, conventional tests are not feasible any more. Since for these formations, massive stimulation is required to obtain economic production. Therefore, it is extremely important to establish the formation pressure and permeability prior to the main stimulation. A minifrac test

has proved to be convenient and feasible for this purpose.

### 3.4.1 Well and reservoir testing

There are three major developments during the evolution period of well and reservoir testing. They are the semi logarithmic straight line (Horner analysis), log-log diagnostic plot and log-based derivative (Economides & Nolte 2000).

As the first development, Horner (1951) presented the important equation for buildup analysis with semi logarithmic approximation. According to this model, the shut-in pressure  $p_{ws}$  in psi can be calculated with the assumption of the infinite-acting radial flow.

$$p_{ws} = p_i - \frac{162.6qB\mu}{kh}\log\frac{t_p + \Delta t}{\Delta t}$$
(3.4)

where  $p_i$  is the initial reservoir pressure in psi, q is the rate during the flowing period in STB/D, B is the formation volume factor in RB/STB,  $\mu$  is the viscosity in cp, k is the permeability in md, h is the reservoir thickness in ft,  $t_p$  is the producing (flowing) time in hr, and  $\Delta t$  is the time since shut-in in hr.

A semi logarithmic plot of log ( $[t_p + \Delta t]/\Delta t$ ) versus  $p_{ws}$  should form a straight line (Figure 3.9) with the slope equal to

$$m = -\frac{162.6qB\mu}{kh} \tag{3.5}$$

from which the unknown permeability k, or kh if h is also not known, can be determined.

From the extension of the correct straight line to t = 1 hr, the value of the pressure  $p_{1hr}$  can be extracted, and Horner suggests that the skin effect s can be calculated by

$$s = 1.151 \left( \frac{p_{1hr} - p_{wf(\Delta t = 0)}}{m} - \log \frac{k}{\phi \mu c_t r_w^2} + 3.23 \right)$$
 (3.6)

The value of  $p_{wf}(\Delta t = 0)$  is the last value of the bottomhole flowing pressure, m is the slope of the line,  $\phi$  is the porosity (unitless),  $c_t$  is the total compressibility in psi<sup>-1</sup>,  $r_w$  is the wellbore radius in ft, and the constant 3.23 is to account for oilfield units and the conversion from ln to log.

The problem of the Horner semi logarithmic analysis is, several straight lines can be obtained (Figure 3.9). It is often difficult to identify, which one is the correct one.

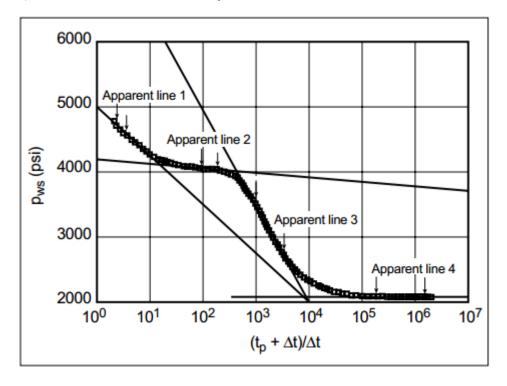


Figure 3.9 Analysis of pressure buildup data on a semi log plot. Arrows denote beginning and end of semi log linear trends (Economides & Nolte 2000)

The second major development of the log-log plot resolved the problem of Horner's analysis. It was proposed by H. J. Ramey for the diagnosis of the well pressure transient response. Figure 3.10 shows the typical Log-log curve of the pressure buildup test. However, there are still problems with the log-log plot of pressure difference versus time. The determination of reservoir and well variables are dependent on the time duration for a full development of infinite-acting radial flow, the specific geometries and features of the reservoir.

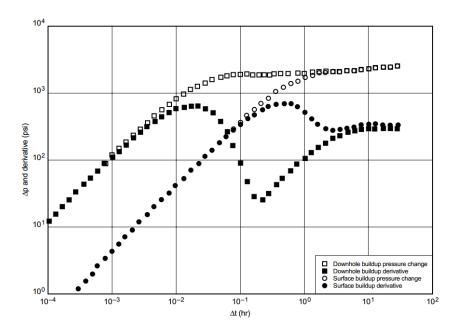


Figure 3.10 Log-log plot of pressure buildup data (Economides & Nolte 2000)

The third method is based on the dimensionless pressure derivative. In this method not only, the pressure but also the pressure derivative is used. This method overcomes the problem of multiple solutions in the previous solutions, because the pressure derivative is more clear and definitive than the pressure itself. Figure 3.11 shows the dimensionless type curve for pressure drawdown and derivative.

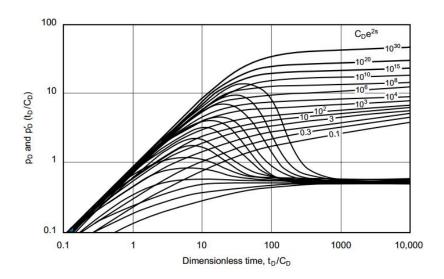


Figure 3.11 Dimensionless type curves of pressure drawdown and pressure derivative for an infinite-acting reservoir with wellbore storage and skin effect (Bourdet et al., 1983)

By comparing the measured pressure transient data with the pressure type curves discussed in the previous section, the flow pattern can be recognized, which can also be used to determine the reservoir parameters.

There are different flow types, including radial flow, linear flow, spherical flow etc. As an example, the parameter determination for the radial flow is discussed. The radial flow (Figure 3.12) is characterized by flow converging to a line at the center of a circular cylinder (Economides & Nolte 2000). The pressure response in the radial flow are dependent on the reservoir permeability, skin effect, reservoir pressure, the effective radius of the cylinder as well as the radial of the outer boundary.

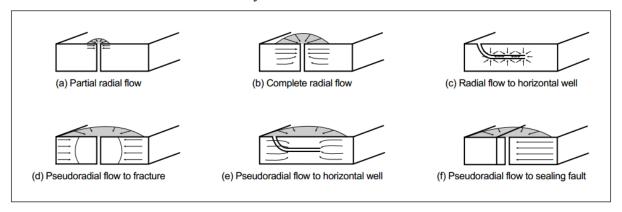


Figure 3.12 Radial flow geometries (Economides & Nolte 2000)

With the help of the semi logarithmic plot of pressure versus elapsed time, the reservoir permeability can be determined using:

$$k = \frac{1.151\alpha_p q B \mu}{mh} \tag{3.7}$$

where  $\alpha_p$  is a coefficient 141.2 in oilfield unit, m is the absolute value of the slope of a semi-log line.

With the method, the horizontal permeability can be determined in vertical wells (Economides & Nolte 2000). The horizontal permeability determined from analysis of the radial flow regime is the geometric mean of the maximum permeability  $k_x$  oriented parallel to the principal permeability axis, and of the minimum permeability  $k_y$  oriented perpendicular to it, as given by  $\sqrt{k_x k_y}$ .

In horizontal wells, the radial flow regime about the well (Figure 3.12c) represents the geometric mean of the horizontal permeability  $k_H$  (or  $\sqrt{k_x k_y}$ ) and the vertical permeability  $k_V$  (or  $k_z$ ), given by  $\sqrt{k_H k_V}$ , or, more precisely,  $\sqrt{k_Y k_z}$  (if the well is oriented parallel to the principal permeability axis). In this case, the equation for the slope of the semi log line is

$$\sqrt{k_y k_z} = \frac{1.151 \alpha_p q B \mu}{m_{epr} L_p} \tag{3.8}$$

where the subscript epr of m refers to early pseudo radial,  $L_p$  is productive length in ft.

# 3.4.2 Rock properties from well logs

Well logging is the practice of making a detailed record (measurement versus depth or time, or both) of the geologic formations penetrated by a borehole. There are two types of well logs (Patra 2016). The first one is based on visual inspection of samples brought to the surface, which is named geological logs. The other one is based on physical measurements made by instruments lowered into the hole, which is named geophysical logs.

To construct a simulation model of the reservoir formation and caprock, the properties of the rock formation layers must be obtained firstly. Each property in a layer has either a constant, averaged value, or has a linear distribution of the depth. These properties are either related to the fluid flow in the formation or related to the deformation of the formation.

There are several types of depths used in the oil field. True vertical depth (TVD) is the depth measured along the vertical. If a (zero) reference point is given, it is unique. Measured depth (MD) is the distance measured along the wellbore trajectory. This is not unique, because it depends on the way it is measured. MD during drilling is measured by the length of pipe that has gone into the ground. MD at wireline logging time is measured by the length of cable that has gone into the ground. Finally, logging-while-drilling (LWD) data are logged versus time, which complicates the issue because several measurements can be assigned to the same depth. TVD is required to design the treatment placement, MD is required to compute the fluid friction and fluid displacement (e.g. fracture height is related to properties in TVD, not in MD).

The temperature of the formation is critical for the performance of both matrix stimulation products and hydraulic fracturing fluids. The mud temperature obtained from wireline logging time is typically used for the estimation of the formation temperature.

Properties like porosity, permeability, and fluid types in the formation can also be determined from logs.

### **3.4.2.1** Lithology

The determination of minerals and fluids in the formation, especially their volumetric distribution, is important for the gas reservoir development. This can be achieved with lithological analysis. The most often used method for lithological analysis is shaliness indicator, which is based on gamma ray measurement. If the natural radioactivity of a formation is due to the clay minerals, high gamma ray values (>90 API units) indicate a shale, while low gamma ray values (<20 API units) indicate a clean sandstone. Values between these indicate a mixture of clay and sand (Economides & Nolte 2000).

The linear equation below relates quantitatively the gamma ray count to the concentration of potassium oxide (K<sub>2</sub>O) in percent:

$$GR_{API} = 15[K_2O] (3.9)$$

There are different tools for different combinations of minerals. From each of these methods the tool response TR can be characterized by an equation, which can be cast in a form involving the volumetric fraction of n minerals and a fluid volumetric fraction  $V_f$ .

$$TR = f(V_{mineral}^1, V_{mineral}^2, \dots, V_{mineral}^n, V_f)$$
(3.10)

## 3.4.2.2 Porosity determination

Porosity is the percentage of pore volume or void space, or that volume within rock that can contain fluids. The porosity of formation usually varies from nearly 0% for evaporites to up to Optimization of Multistage Hydraulic Fracturing Treatment for Maximization of the Tight Gas Productivity

40% for unconsolidated formations and even higher for chalk or diatomite. However, the porosity for tight gas sandstone is normally low, e.g. the average porosity of Leer tight gas reservoir, which was used for simulation in this dissertation, is 9.7% (Koehler 2008).

Porosity is classically divided into two groups: primary and secondary porosity. Primary porosity is the original space between the grains as well as sedimentary particles formed during the geological deposition, while secondary porosity is the void space created by tectonic forces or mineral dissolution. The correlations rely mostly on the primary porosity, not the secondary porosity. The total porosity is the volume that is not occupied by solid rock. A part of the pore volume is isolated or occupied by bounded water. The other part is interconnected, so that the fluid can flow through this part. This part is named as effective porosity.

In practice there are various methods for the determination of formation porosity (Economides & Nolte 2000). The porosity can be estimated from density, neutron, sonic, nuclear magnetic resonance (NMR) tools, resistivity etc. Density tools measure the electron density of a formation, which is extremely close to its bulk density  $\rho_b$ . The porosity can be determined with

$$\phi_D = \frac{\rho_{ma} - \rho_b}{\rho_{ma} - \rho_f} \tag{3.11}$$

where  $\rho_{ma}$  is the rock matrix density determined from the lithology,  $\rho_b$  is the buck density of the rocks,  $\rho_f$  is the fluid density (e.g. mud filtrate) which is dependent on temperature, pressure and salinity. Neutron tools measure an index of how much hydrogen is present in the formation. A simple average of neutron porosity  $\phi_N$  and density-based porosity  $\phi_D$  yields a good estimate of the effective porosity:

$$\phi_{eff} \cong \frac{1}{2}(\phi_N + \phi_D) \tag{3.12}$$

The pore fluid has large influences on the sonic wave propagation. The porosity can also be determined from the elastic properties of the solid and the fluid, especially from the travel times of sonic waves:

$$\phi_s = A \frac{\Delta t - \Delta t_{ma}}{\Delta t_f - \Delta t_{ma}} \tag{3.13}$$

where A is a constant and  $\Delta t$  denotes the measured transit time of a sonic wave in the formation. The transit time in the matrix  $\Delta t_{ma}$  is known from the lithology. The sonic porosity  $\phi_S$  is a strong function of the properties of the fluid in the pore space. Nuclear magnetic resonance (NMR) tools measure the relaxation time of protons. Extracting porosity from NMR measurements is complicated. However, the measured values are very close to  $\phi_{eff}$ , and the method is very suitable for the porosity estimation of shale formations. Finally is the porosity measurement from resistivity. If the resistivity of the rock matrix is assumed to be infinite compared with that of the fluid, the conductivity of the formation is proportional to the porosity. The formation factor F is defined as

$$F = \frac{R_o}{R_w} \tag{3.14}$$

where  $R_o$  is the resistivity of the formation, which is fully saturated with brine of resistivity  $R_w$ . Archie (1942) assumed that the formation factor is related to the total porosity by the relation

$$F = \frac{a}{\phi^m} \tag{3.15}$$

where a and m are constants depending on the type of the formations, e.g. a = 0.62 and m = 2.15 for clean sandstones. Therefore, if  $R_w$  is known, the total porosity can be estimated by Eqs. (3.14) and (3.15):

$$\phi = \left[\frac{aR_w}{R_o}\right]^{1/m} \tag{3.16}$$

This technique is not recommended, because it is greatly affected by the fluid saturation and conductive minerals in the matrix.

Finally, the best estimate of porosity is obtained from a combination of logs, using synergistic processing that accounts for the response of each tool and is tailor-made to the geologic environment.

#### 3.4.2.3 Saturation

Water saturation  $S_w$  is the fraction of the pore volume occupied by water. The saturation is important for the estimation of the gas/oil in place and calculation of relative permeability. It can also be used to estimate the compressibility of the formation fluid for computing the compressibility-controlled leak off.

The saturation can be calculated from the Archie's model (Archie 1942), namely

$$R_t = \frac{R_w A}{\phi^m S_w^n} \tag{3.17}$$

where  $R_t$  is the true resistivity of the formation,  $R_w$  is brine of resistivity, A is a constant, m is the cementation index (constant), and n is the saturation exponent (constant).

The water saturation  $S_w$  of Leer tight gas reservoir is a function of porosity and height above free water level (FWL). It is assumed that the water saturation and FWL has the following relationship

$$S_w = \frac{C_2}{H(\text{FWL})^x} \tag{3.18}$$

The parameter of this model can be determined by regression with measured data points. The final results are shown in Figure 3.13 (Koehler 2008). The average value of saturation, which was used in the numerical simulation in this dissertation, is 34%.

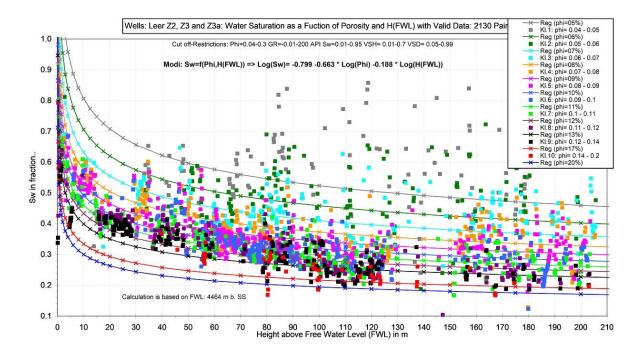


Figure 3.13 Porosity-classified logging data together with the field function with parameter: Height above FWL (Koehler 2008)

# 3.4.2.4 Permeability

Permeability is a measure of the ease with which fluids can flow through a formation. It is a tensor, and its value depends on the orientation of the flow. The permeability perpendicular to the bedding  $k_V$  (i.e., vertical) is usually at least 1 order of magnitude lower for sandstone reservoirs, which, it can be more than 2 orders of magnitude lower for laminated sandstone reservoirs (Economides & Nolte 2000). In some carbonate reservoirs, however,  $k_V$  can be equal to or larger than  $k_H$  (Economides & Nolte 2000).

Permeability can be estimated either by indirect or direct measurements (Economides & Nolte 2000). Direct measurements (formation testing) provide discrete measurements of permeability. It can either be determined from formation tests or well tests. Indirect measurements provide a continuous log of permeability that must be calibrated with the direct individual measurements (e.g., on cores or through formation testing).

The permeability can be determined from the following indirect measurements:

- a. Correlation to porosity and water saturation
- b. From lithology and porosity
- c. From the Stoneley wave

Obviously, porosity is a quantity related to permeability because permeability is derived from interconnected pores. Figure 3.14 listed the In-situ permeability distribution from core data of Leer Z and other Ostfriesland Wells. The permeability of Leer tight gas reservoir, which was used for simulation in this dissertation, is between 0.02 and 0.15 mD (Koehler 2008).

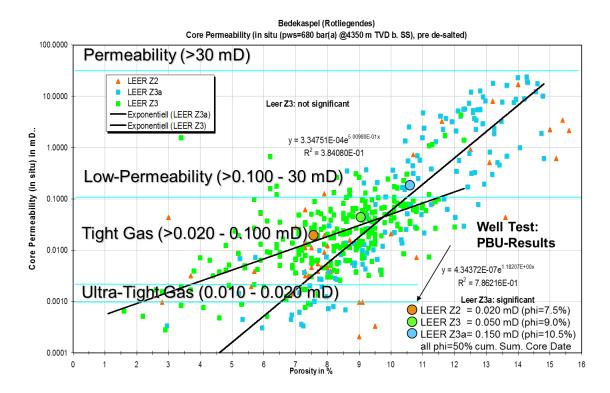


Figure 3.14 In-situ Permeability Distribution from Core Data of Rotliegendes sandstones: Leer Z and other Ostfriesland Wells (Koehler 2008)

When several fluids are present, it is customary to introduce relative permeability. The relative permeability to water  $k_{rw}$  is

$$k_{rw} = \frac{k_w}{k} \tag{3.19}$$

where k is the absolute (or "total") permeability of the formation for a single fluid,  $k_w$  is the effective permeability of the formation to water. Similarly, the relative permeability to oil  $k_{ro}$ 

relates the effective permeability to oil  $k_o$  to the total permeability k by

$$k_{ro} = \frac{k_o}{k} \tag{3.20}$$

Relative permeability typically depends on the water saturation of the formation  $S_w$  (Amyx et al. 1960, Figure 3.15).

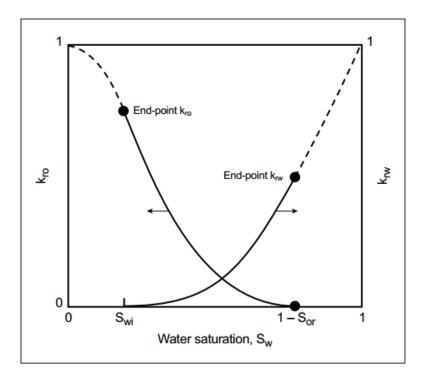


Figure 3.15 Typical variation of relative permeability as a function of water saturation (Dake, 1982).  $S_{or} = residual$  oil saturation.

Several experiments were performed by Häfner et al. 2006 to determine the capillary and twophase functions of Rotliegendes sandstones, which is the goal layer of later gas production in tight gas reservoir Leer. The material parameters (e.g. displacement threshold pressure  $P_d$  and exponent  $\lambda$ ) are estimated by fitting the Corey-Burdine equation to the measured capillary pressure data. Based on Corey's model, a modified form in terms of Corey-Brooks (1966) and Corey-Burdine (Corey 1954, Burdine 1953) correlations for the gas-water relative permeability and capillary pressure functions are represented as follows:

$$k_{rg} = a(1 - S_{gc} - S_w)^2 \left[ 1 - b(S_w - S_{wi})^{\frac{2}{\lambda} + 1} \right]$$
(3.21)

$$k_{rw} = c(S_w - S_{wi})^{\frac{2}{\lambda} + 3} \tag{3.22}$$

$$p_c = d(S_w - S_{wi})^{-\frac{1}{\lambda}} (3.23)$$

where

$$a = k_{rg}(S_{wi}) \cdot \left(1 - S_{wi} - S_{gc}\right)^{-2}$$

$$b = \left(1 - S_{wi} - S_{gc}\right)^{-\left(\frac{2}{\lambda} + 1\right)}$$

$$c = k_{rw}(S_{gc}) \cdot \left(1 - S_{wi} - S_{gc}\right)^{-\left(\frac{2}{\lambda} + 3\right)}$$

$$d = p_d \cdot \left(1 - S_{wi} - S_{gc}\right)^{\frac{1}{\lambda}}$$

The Figure 3.16 shows the set of capillary pressure functions of the Rotliegendes sandstones subdivided onto five porosity classes used as calculation basis. The parameters like  $S_{wi}$ ,  $S_{gc}$ ,  $P_d$  necessary for further calculations can not be directly measured by the mercury injection method and must be estimated from the measured mercury- $p_c$ -functions with reference to the known correlations and regression functions. The irreducible water saturations are estimated for the capillary pressure level of  $p_c$ =3MPa by truncation of the capillary pressure functions at this pressure level. The estimated values, which are used for the later case study of tight gas borehole Leer Z4 are shown in the 4-th column of the Table 3.1.

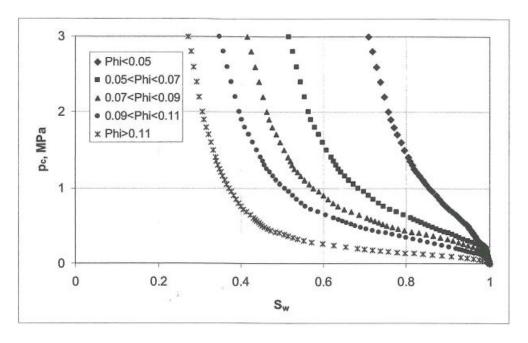


Figure 3.16 Mercury injection capillary pressure functions of different porosity class Optimization of Multistage Hydraulic Fracturing Treatment for Maximization of the Tight Gas Productivity

Rotliegendes sandstones measured at lab-conditions (Häfner et al. 2006)

The estimated critical gas saturations and the corresponding threshold pressures are shown in the table 7.7 (coloums 5 and 9).

Table 3.1 lab-conditions material parameter of the geo-model for the case study (Häfner et al. 2006)

Porosity	ka,	kw,	Swi	Sgc	krg(Swi)	krw(Sgc)	p <sub>d</sub> ,	Pth,	lambda
class	μD	μD					MPa	MPa	
1	2	3	4	5	6	7	8	9	10
ф>0.11	750	681	0.272	0.035	0.442	0.706	0.093	0.058	0.794
0.09< ф	180	103	0.348	0.020	0.313	0.476	0.216	0.107	0.781
<0.11									
0. 07< ф	58	24	0.415	0.025	0.215	0.314	0.263	0.173	0.794
<0.09									
0. 05< ф	22	6.3	0.516	0.042	0.099	0.186	0.338	0.264	0.763
<0.07									
ф<0.05	1.3	0.16	0.623	0.100	0.022	0.019	0.797	0.876	0.775

The specific water permebility in the column 3 of the Table 3.1 is calculated by Jones and Owens correlation (Eq. (3.24).

$$k_w = k_a^{1.32} \text{ [mD]}$$
 (3.24)

Where the absolute permeability ka is introduced in [mD].

The end-point relative gas permeabilities  $k_{rg}(S_{wi})$  (table (3.1), column 6) is calculated by using the following formula (Eq. (3.25).

$$k_{rg}(S_{wi}) = \left(1 - \frac{S_{wi}}{0.7}\right)^{1.5} (1 - S_{wi}^2)$$
 (3.25)

The endpoint relative water permeabilities  $k_{rw}(S_{gc})$  (Table 3.1, column 7) are calculated by using a form of Corey equation (Eq. (3.26)):

$$k_{rw}(S_{gc}) = \left(\frac{1 - \delta \cdot S_{gc} - S_{wi}}{1 - S_{wi}}\right)^4 \left(\frac{k_{w100}}{k_a}\right)$$
(3.26)

where  $\delta$  is a fitting parameter,  $k_a$  and  $k_w$  represent absolute permeability and specific water permeability.

The material parameters displacement threshold pressure  $p_d$  and exponent  $\lambda$  are estimated by fitting the Corey-Burdine equation to the measured capillary pressure data. They for each porosity class are showen in column 8 and 10 of the Table 3.1.

The gas-brine relative permeability and capillary pressure functions of water permeability can be calculated by Eqs. (3.21) to (3.23). These parameter groups used in calculations are summarized in Table 3.2.

Table 3.2 Parameter of the relative permeability capillary pressure correlation formulas for laboratory conditions

Porosity class	a	b	с	d MPa
ф > 0.11	0.921	3.64	5.35	0.059
$0.09 < \phi < 0.11$	0.784	5.12	6.09	0.120
$0.07 < \phi < 0.09$	0.686	7.70	7.71	0.127
0. 05< φ<0. 07	0.506	19.2	18.31	0.116
ф <0. 05	0.292	98.7	24.15	0.152

The Figure 3.17 shows the estimated relative permeability functions at laboratory stress conditions.

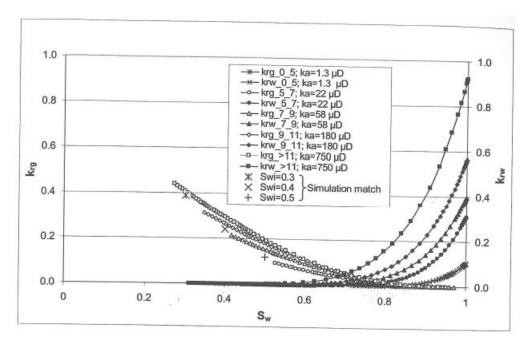


Figure 3.17 Lab-conditions gas-brine relative permeability functions of the different porosity class Rotliegendes sandstones correlated from mercury injection capillary pressure functions (Häfner et al. 2006)

# 3.4.2.5 Mechanical properties

The mechanical properties of the formation rock and the stress have large influences on the hydraulic fracturing geometry. The mechanical properties determined the stress change and the deformation in formations. They are not independent of each other.

The elastic properties of the formation can be determined with sonic logs (Economides & Nolte 2000). When a pressure pulse is generated in a wellbore, different types of wave will be generated in the rock formations. The two important waves for the determination of the elastic parameters of the medium are compressional waves (*P*-waves) and shear waves (*S*-waves). The sonic tool measures the characteristic propagation speed of *P*- and *S*-waves.

For isotropic media, there are only two independent elastic constants. The shear modulus G and Poisson's ratio v are related to the propagation speeds of the P and S waves  $u_p$  and  $u_s$ .

$$G = \rho_b u_s^2 \tag{3.27}$$

$$v = \frac{2u_s^2 - u_p^2}{2(u_s^2 - u_p^2)} \tag{3.28}$$

where  $\rho_b$  is the density of the formation.

The Young's modulus *E* is related to the above two constants as follows:

$$E = 2G(1+v) (3.29)$$

In numerical simulations, statically derived material properties (Young's modulus and Poisson's ratio) are representative of fracturing conditions, while dynamic properties are less expensive and easy to obtain. Therefore, before running numerical studies, the measured dynamic properties must be converted to static properties. In this study, the difference between dynamic and static Poisson's ratio is ignored because it is usually small for all practical purposes. The relationship between dynamic and static modules is usually in the form of a linear or exponential relationship. Many studies were performed on different locations and rock types to describe this relationship (Morales & Marcinew 1993, Lacy 1997, Bradford et al. 1998, Wang 2000, Mockovciakova & Pandula 2003). The dynamic Young's modulus, which was used for simulation of tight gas well Leer Z4 in this dissertation is converted to static Young's modulus in terms of HB curves (for porosity interval 0 - 14%) from Morales & Marcinew 1993.

$$E_s = E_d \cdot exp(0.2317 - 0.3352lnE_d) \tag{3.30}$$

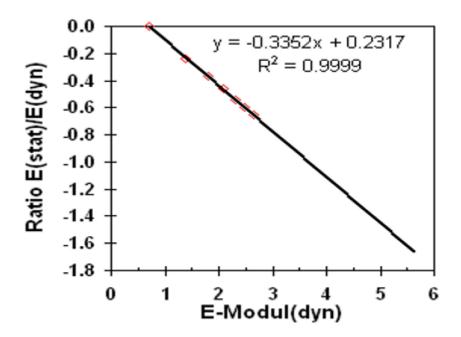


Figure 3.18 Correlation between dynamic Young's modulus  $(E_d)$  and ratio of static/dynamic Young's modulus  $(E_s/E_d)$  test data on sandstones cores (Koehler 2005)

## 3.4.3 Reservoir properties from well logs

## 3.4.3.1 Pore pressure

The pore pressure is the pressure of the fluid in the formation. The pore pressure has great influences on the hydraulic fracturing treatments as well as the production. It is also strongly related to the stress state of the formation.

The pore pressure of the formation can be measured either by well tests or obtained through the formation tester. During the measurement the formation tester and the formation will be sealed. Then the fluid is pumped from the formation so that the pressure in the formation tester is lower than the far field pore pressure. The formation fluid will flow under the pressure difference, until make the pressure in the tester reach equilibrium with the formation. The fluid pressure at the time of equilibrium serves as the approximate pore pressure.

The above-mentioned method is only a point-wise measurement. Various pressure test will be carried out, to generate a pore pressure profile with depth. The formation pore pressure usually

follows a hydrostatic pressure distribution, when there is no fluid flow under the effect of gravity, namely

$$\frac{dp}{dz_{TVD}} = \rho_f g \tag{3.31}$$

In an unproduced reservoir, there may be different fluid components, including gas, oil and water. If the depth-dependent pore pressure is plotted in a figure, there are various line segments with a slope given by the density of the fluid in the formation. The slope will change depending on the fluid, which enables the determination of fluid contacts (Figure 3.19).

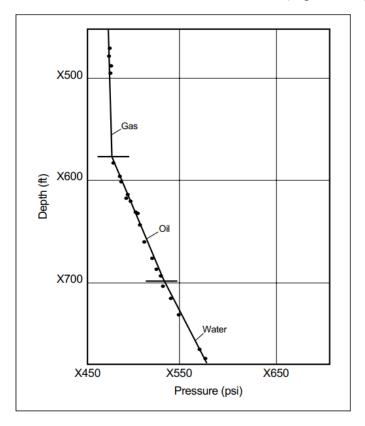


Figure 3.19 Depth-dependent pressure profile with fluid types and fluid contact (Economides & Nolte 2000)

# 3.4.3.2 Reservoir temperature

Formation temperature has large influences on the performance of both matrix stimulation products and hydraulic fracturing fluids. Like the pore pressure distribution, a temperature profile should be obtained. The wireline logging is the only test method that can obtain a

continuous well temperature curve (Economides & Nolte 2000).

The discrete point temperature test can be obtained by sampling the fluid in the formation testers. The temperature of the fluid sample is continuously monitored during the sampling process. It is currently the most accurate temperature measurement method. Another good method for estimating reservoir temperature is when the formation fluid is just beginning to flow after the perforation in the formation. The temperature at the bottom of the well is recorded by a slickline-conveyed gauge.

Since the hydraulic fracturing treatment are performed in deep underground, they cannot be seen and measured directly. In Cipolla & Wright (2000) various research methods (e.g. microseismic fracture mapping, surface and downhole tilt fracture mapping, temperature logging, borehole image logging, net pressure analysis, well testing, production analysis etc.) are introduced to overcome this problem. Among them only through microseismic fracture mapping, surface and downhole tilt fracture mapping methods can direct obtain approximate fracture geometry. In addition, temperature logs to estimate fracture height have been firstly discussed by Agnew 1966. It locates cold anomalies that indicates the location of the cold fracture fluid injection and warm anomalies that indicates warm-back after shut-in (Figure 3.20).

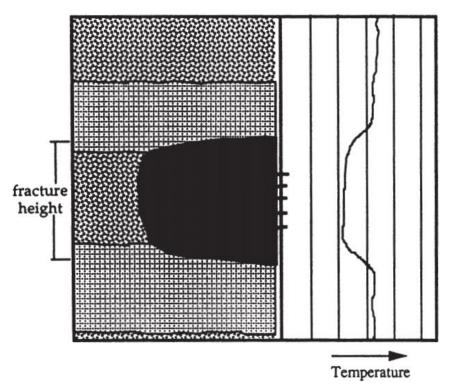


Figure 3.20 An ideal temperature log (Davis et al. 1997)

#### 3.4.3.3 In-situ stress state

The shape of hydraulic fractures is strongly dependent on the stress state in the earth. The stress is a tensor, and it can be described by three principal stresses, namely maximum principal stress  $\sigma_1$ , intermediate principal stress  $\sigma_2$  and minimum principal stress  $\sigma_3$ , and their mutually perpendicular directions. Because the three principal stresses are orthogonal, the two principal stress directions can fully describe them. The complete description of the stress state is very important, because the hydraulic fracture propagates along the direction perpendicular to the minimum principal stress. If  $\sigma_3$  is in the horizontal direction, the hydraulic fracture should be vertical; if  $\sigma_3$  is in the vertical direction, it will produce a horizontal fracture; if  $\sigma_3$  is in an inclined direction, the resulting hydraulic fracture is perpendicular to the slope.

In the hydraulic fracturing engineering application, the recommended method of measuring stress is as follows: First, assuming that it is far from a major fault, the in-situ stress measurement method is used for a reservoir with a depth of more than 610 m, because in this case, the overburden is one of the three principal stresses (Economides & Nolte 2000).

- Firstly, determine the value of  $\sigma_v$
- Secondly, determine the direction of  $\sigma_h$
- Finally, the relationship between the minimum stress value and the depth is determined and compared with overburden to determine which stress is  $\sigma_3$ .

These three steps are introduced in detail below.

The overburden is the weight of the column of overlying rocks. Although it cannot be directly measured, the integral along the depth of the bulk density can be easily calculated as follows, which is analogous to the determination of pore pressure under hydrostatic conditions:

$$\sigma_{\nu}(z_{TVD}) = \int_{0}^{z_{TVD}} \rho_{b} dz \tag{3.32}$$

The orientation of the principal stress can be obtained by different methods. The commonly used methods (Economides & Nolte 2000) are: World Stress Map, geologic maps, shear anisotropy, wellbore breakouts, drilling-induced fractures, tests on cores, population of natural fractures, hydraulic fracture diagnostics.

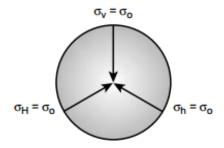
The minimum principal stress can only be measured indirectly, discontinuously. The laboratory analysis of the core can obtain the ratio of effective stresses acting on the formation during coring by measuring the strain. Micro-hydraulic fracturing technique (Haimson 1993) can be used for open- or cased holes. Closure pressure (or sometimes ISIP) obtained from a hydraulic fracturing calibration treatment can also estimate the minimum principal stress acting on the formation.

It is not easy to accurately estimate intermediate stress. It is normally determined in combination of the minimum principal stress, e.g. using the breakdown pressure to calculate intermediate pressure (Hubbert & Willis 1957). However, with the recent research on the breakdown process (Detournay & Carbonell 1994), it has been found that estimating the intermediate stress from the breakdown pressure is not reliable, so it should not be used for the stress analysis.

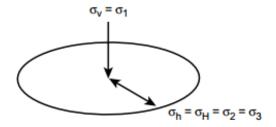
Due to the relationship of vertical and horizontal stresses, different stress regimes can be defined (Engelder 1993). Five in-situ stress states can be determined based on the principal

stresses (e.g. normal fault regime, thrust fault regime, strike-slip fault regime etc., Figure 3.21). The first one is lithostatic stress state, in which the three principal stresses are equal (i.e.), e.g. poorly consolidated shales, salt, extremely overpressured sediments. The second case is that the two horizontal principal stresses are equal and less than the overlying stress. In other stress regimes, the three principal stress values vary more or less, and in-situ stress measurements and borehole image analysis results indicate that this is the most common case. The difference in horizontal stresses may be due to the presence of tectonic stresses or certain geological phenomena such as folds and faults.

## Lithostatic State of Stress



## Equal Horizontal Stresses



## States of Stress and Fault Regimes

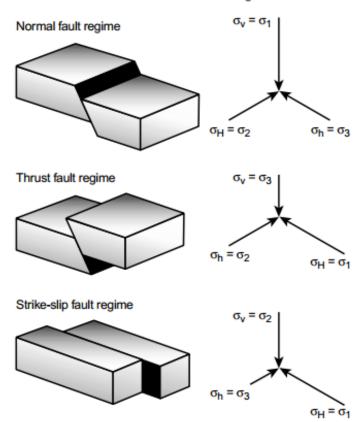


Figure 3.21 Stress regimes with spatial distribution of stresses ( $\sigma_0$ = equal-stress constant) (Economides & Nolte 2000)

There are also mathematical stress models for the continuous description of the horizontal stress of the target layer as a function of depth. These models consider not only the single measurement, but also the elastic or poro-elastic effects. Thus, the term "fracture-closure pressure" is synonymous with minimum horizontal stress. The continuous profile of  $\sigma_h$  or  $\sigma_{closure}$  can be obtained by the following equation (Leshchyshyn 2004), where the biot coefficient  $\alpha$  is used as a correction factor related to lithology:

$$\sigma_{total} = \left(\frac{v}{1 - v}\right) \cdot \left(P_z - \alpha_v \cdot P_p\right) + \alpha_h \cdot P_p + \sigma_t + \varepsilon_t \cdot E \tag{3.33}$$

where  $\sigma_h$  is total fracture closure stress, v is Poisson's ratio (from DSI-Log),  $P_z$  is lithostatic pressure (overburden pressure),  $\alpha_v$  is vertical Biot coefficient,  $P_p$  is pore pressure,  $\alpha_h$  is horizontal Biot coefficient,  $\sigma_t$  is tectonic stress,  $\varepsilon_t$  is tectonic strain, E is Young's Modulus. This model is suitable for sandstone, shale und carbonate with low porosity and permeability.

The In-situ stress conditions of well Leer Z are estimated and the results are comparable with that in Northern Germany from World Stress Map (Figure 3.22, Heidbach et al. 2016). The measured orientations of maximum in-situ horizontal stresses at the Leer site match with the regional trend in Northeast Germany.

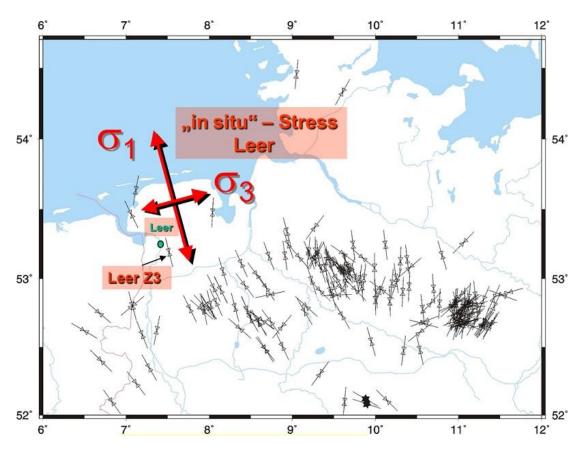


Figure 3.22 Comparison of the stress orientation of Leer Z with that in Northern Germany from world stress map (Heidbach et al. 2016)

Orientation of a horizontal well in direction of the minimum stress to create transverse multiple fractures parallel to the maximum stress orientation. The preferred hydraulic fracture propagation (PFP) in the case of Leer is an azimuth 166 °, it is approximately an NNW-SSE direction.

To estimate this maximum stress for the optimization of direction of horizontal drilling reoriented cores investigations and wellbore breakouts were performed (Figure 3.23). Wellbore
breakouts are stress-induced enlargements of the wellbore cross-section (Bell and Gough 1979).
When drilling, the material removed from the subsurface no longer supports the surrounding
rock. As a result, stress is concentrated in the surrounding rock (i.e., the wellbore wall).
Borehole breakout occurs when the stress around the borehole exceeds the stress required to
cause collapse of the borehole wall (Zoback et al. 1985; Bell 1990). Further investigations
carried out in the framework of the DGMK study 593-5 have confirmed this main direction of

stress (Müller et al. 2004). Thus, in-situ stress determines the direction of the hydraulic fractures and affects the final fracture geometries.

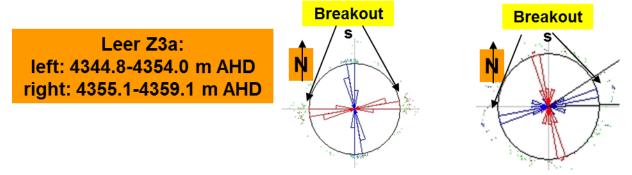


Figure 3.23 Stress Direction - Borehole Studies: re-oriented cores investigations and wellbore breakouts (Koehler 2005)

### 3.4.4 Minifrac test

A minifrac test is an injection/falloff diagnostic test performed without proppant before a main fracture stimulation treatment (Soliman et al. 2005). The intent is to break down the formation and create a fracture with a small volume of high-pressured fluids at a defined rate. Injection rate, pressure and falloff pressure are recorded for analysis.

The Minifrac test type supports pre-closure analysis, after-closure analysis, modeling, and step-down test analysis. Pre-closure analysis is used to determine instantaneous shut-in pressure (ISIP), fracture closure pressure ( $P_c$ ) and time ( $t_c$ ), fracture gradient (ISIP/TVD), net pressure ( $P_{net}$ ), and fluid efficiency ( $\eta$ ). Post-closure analysis is used to identify reservoir properties, such as reservoir pressure, transmissibility, and permeability.

To perform a minifrac test in an openhole, the selected test interval is isolated from the surrounding well using a packer arrangement (Figure 3.24).

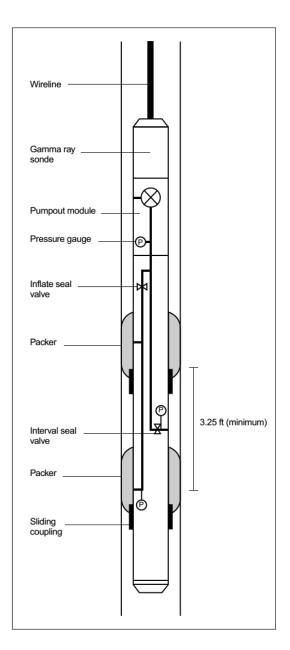


Figure 3.24 Wireline stress tool (Economides & Nolte 2000)

Fracturing fluid is then injected in the interval at a defined constant flow rate. During the injection, the wellbore is pressurized up to the initiation of a tensile fracture. Initiation of the fracture is usually recognized by a breakdown on the pressure versus time record, which is named breakdown pressure (Figure 3.25). However, sometimes breakdown pressure does not show while initiation occurs prior to breakdown. After breakdown, injection is continued until the pressure stabilizes. After shut-in, the pressure begins to decay. The fracturing fluid is usually a low-viscosity (non-gelled) fluid for low-permeable zones or a drilling mud for zones

with higher ranges of permeability. The amount and injection rate of the fluid is usually determined to achieve the pre-designed fracture size. Usually it is injected with less than 100-gal fluid at a flow rate from 0.25 to 25 gal/min (Economides & Nolte 2000).

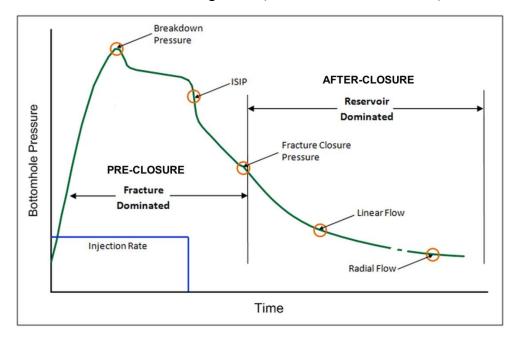


Figure 3.25 Typical pressure behavior of Minifrac Tests (modified from Fekete Associates Inc. 2012)

Usually several injection/fall-off cycles are performed until repeatable results are obtained (Evans et al. 1989, Figure 3.26). Using downhole shut-off devices, downhole pumps and downhole pressure gauges can make the most accurate measurement. A downhole shut-off tool and downhole pumps have the advantage of minimizing wellbore storage during pumping and shut-in (Thiercelin et al. 1993).

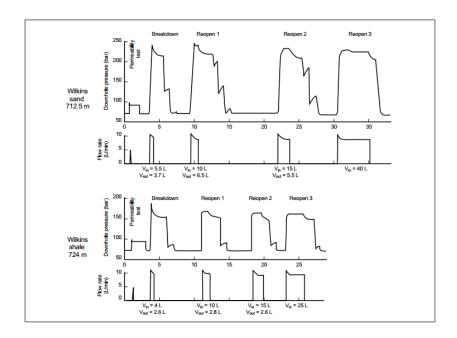


Figure 3.26 Pressure and injection rate record obtained into a sand and immediately underlying shale (Evans et al. 1989)

The minimum principal stress can be estimated using different techniques. The simplest one is to take the instantaneous shut-in pressure (ISIP) as an approximate minimum principal stress. However, when this method is used, errors of several hundred psi or more may occur, especially for areas that can generate very high net pressure or porous formations. Recently, the technique of determining the closure pressure has replaced the method of determining the minimum principal stress by the ISIP. Conceptually speaking, the closure pressure is the pressure at which the fracture surface is regular and the fracture can be completely closed.

The pressure behavior during the pre-closure period is fracture dominated. The pressure behavior during the after-closure period is reservoir dominated. During the after-closure period, if we can monitor falloff data for a few weeks we can also see reservoir dominated flow (linear/radial flow, Figure 3.27) for these tests. Linear flow regimes occur before radial flow, and their duration is dependent on the fracture half-length, or the productive length in the case of a horizontal well.

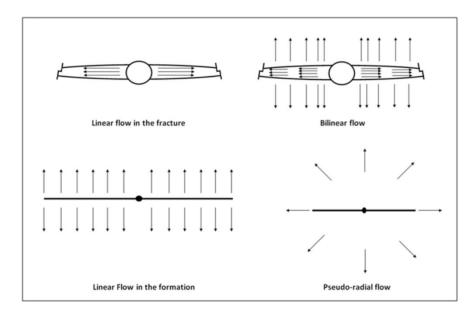


Figure 3.27 Typical flow regimes (Fekete Associates Inc. 2012)

In permeable formations, where the fracturing fluid leaks off from the fracture face, closure pressure is concluded when the pressure decline deviates from a linear dependence on the square root of shut-in time or the square root of the sum of shut-in time and injection time *ti* (Nolte 1982 & 1988a, Figure 3.28).

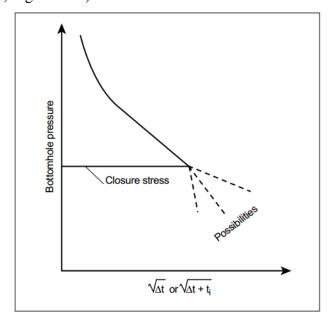


Figure 3.28 Pressure decline analysis (Nolte 1982 & 1988a)

An improved representation of fluid loss is provided using G-plot, which is introduced by

Castillo (1987) for closure inference along with specialized functions for the pressure. Additional examples of the G-plot based method are given by Shlyapobersky et al. (1988b). Although the G-plot provides a firmer foundation than the square-root plot, its derivation does not consider the well-established additional fracture extension and decay after shut-in (Economides & Nolte 2000).

To overcome the ambiguity of decline analysis, the pump-in/flowback (PI/FB) test was developed by Nolte (1979) to estimate the closure pressure before fracturing treatments. The test begins by injecting a volume of fluid (about 10 to 100 bbl) into the formation to create a fracture. Following pump-in, injected fluid is withdrawn from the fracture by flowing back with a constant rate. It is usually between one-sixth and one-quarter of the injection rate (Economides & Nolte 2000). Otherwise, accurate results cannot be obtained (Figure 3.29a). Finally, when the flow back ends, that means when the well is shut-in and surface flowback stops, a period of pressure rebound is observed. The initial interpretation assumed that closure occurred at the inflection point above the intersection point (Figure 3.29b). Then, Shlyapobersky et al. (1988b) suggested that closure occurred at begin of the linear response, which is below the intersection point (Figure 3.29b). Their theory is based on linear response corresponds to wellbore storage only (i.e., when the fracture is closed). This was precisely the case for low fluid loss and an ideal frictionless fluid (Figure 3.29b). In low-permeability formations, the pressure rebound tends toward the closure pressure (Thiercelin et al. 1994).

The pump-in/flowback (PI/FB) test has two advantages over the pump-in/shut-in test. Firstly, flow back accelerates fracture closure, which is especially beneficial for the low-permeability formation. Secondly, pressure rebound period develops an easier distinct signature for fracture closure rather than pump-in/shut-in test (Plahn et al. 1997).

During pressure rebound period, the fluid in the fracture flows into the well until equalization between the well pressure and the pressure within the fracture occurs. Nolte (1982) suggested that the maximum pressure value of the rebound was a lower bound for the closure pressure (i.e., the pressure equilibrated into the closed but conductive fracture).

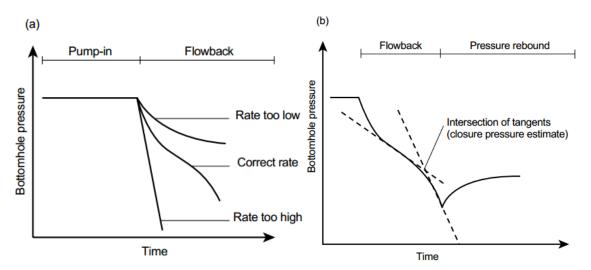


Figure 3.29 Flowback and pressure rebound: (a) influence of flowback rate on pressure response (Nolte 1982 & 1988a) and (b) recommended approach for closure pressure estimation (Plahn et al. 1997).

Not only the fracture closure pressure, but also other information (*Fekete Associates Inc. 2012*) can be yielded from analysis of pressure falloff data. For example,

Instantaneous shut-in pressure (ISIP)

$$ISIP = Final\ Flow\ Pressure - Final\ Flow\ Friction$$
 (3.34)

Final Flow Friction is the friction component of the bottomhole pressure calculation.

Fracture gradient

Fracture 
$$Gradient = ISIP / Formation Depth$$
 (3.35)

• Net Fracture Pressure  $(\Delta p_{net})$ 

Net fracture pressure is the pressure in the fracture minus the in-situ stress. It is required to keep the fracture open. It is an indication of the energy available to propagate the fracture.

$$\Delta p_{net} = ISIP - Closure Pressure \tag{3.36}$$

Fluid efficiency

Fluid efficiency is the ratio of the stored fluid volume within the fracture to the total

injected fluid volume. A high fluid efficiency means low leak-off and indicates the energy of injected fluid was efficiently utilized in creating and propagating the fracture. Unfortunately, low leak off is also an indication of low permeability formation. For minifrac after-closure analysis, high fluid efficiency is coupled with long closure durations and even longer identifiable flow regime trends.

$$Fluid\ efficiency = \frac{G_C}{2+G_C} \tag{3.37}$$

Where  $G_c$  is the G-function time at fracture closure

- Formation leak off characteristics and fluid loss coefficients
- Formation permeability (k)
- Reservoir pressure  $(p_i)$

In this dissertation, the well Leer Z4 for tight gas production was studied. Taking its frac-stage 1 as an example, the fracture specific data was estimated by performing a formation breakdown with a 1<sup>st</sup> datafrac, a minifrac and a 2<sup>nd</sup> datafrac (Koehler & Kerekes 2006, Figure 3.30). At the beginning, a datafrac contained a Formation Breakdown and a following Step Rate Down Test 1 (SRDT 1) and shut-in to examine the near wellbore friction (perforation friction and tortuosity friction) and the fracture closure pressures. After that, a minifrac with cross-linked Sirocco gels and proppant slugs (concentration: 1-3 ppg) was performed to calculate the fluid loss and fluid efficiency. It was also used to verify the expected fracture propagation, to investigate the fracture response on proppant slugs and to check the erosion effect by low concentrated proppant slugs. Then a 2<sup>nd</sup> datafrac with a Step Rate Down Test 2 (SRDT 2) was performed to especially examine the alterations in the near wellbore frictions after the minifrac.

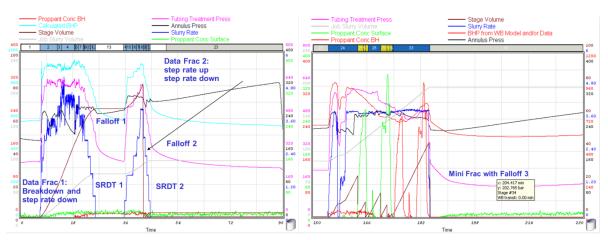


Figure 3.30 A 1<sup>st</sup> datafrac, a minifrac and a 2<sup>nd</sup> datafrac for fracture specific data estimation of frac-stage 1 (modified from Koehler 2005)

According to the recommended approach of Plahn et al. (1997) three injection/fall-off cycles are performed until repeatable results are obtained (Evans et al. 1989). According to 3<sup>rd</sup> falloff pressure the closure pressure is equal to 630 bar (Figure 3.31).

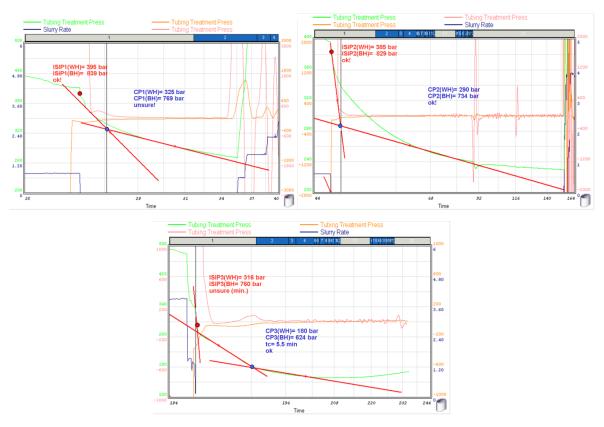


Figure 3.31 ISIP and closure pressure estimation of frac-stage 1 (Koehler 2005)

# 3.5 Fracture conductivity lab testing

As mentioned before, during the hydraulic fracturing process once a fracture is created proppants are injected with fluids downhole to fill in and prop the fracture. One of the indicator of a successful fracture is a large fracture conductivity value. Fracture conductivity is the permeability of the propped fracture region multiplied by the width of the generated fracture (Blair 2015). The propped generated fracture has a much higher permeability than the surrounding formation. It acts as a high permeability channel for fluids to flow through so that the well production can be improved.

Fracture conductivity lab testing, which developed by API standards 61 (1981) and 19D (2008) is a measure of how proppant will perform downhole when injected. A Cooke cell (Figure 3.32) has a top and bottom piston that applies stresses to simulate formation stress experienced by proppants. Between the pistons and proppant pack are sandstone platens which simulate formation rock. The pistons must apply stress at a rate of 100 psi/min  $\pm$  5 psi/min until the cell has reached a 2000 psi increment. Between the platens, proppant is spread out evenly then compressed.

The equation, in SI units used to calculate proppant pack permeability is outlined in API RP-19D (2008).

$$k_f = \frac{\mu QL}{100A(\Delta P)} \tag{3.38}$$

where  $k_f$  is the proppant pack permeability in darcy

 $\mu$  is the viscosity of the test liquid at room temperature in cp

Q is the flow rate in  $cm^3/s$ 

L is the length between pressure ports in cm

A is the cross-sectional area in cm<sup>2</sup>

 $\Delta P$  is the pressure drop (P<sub>upstream</sub> - P<sub>downstream</sub>) in kPa

To calculate the conductivity, pack width must be measured using a digital caliper at each stress.

The conductivity equation in SI units defined in API RP-19D (2008) is shown below.

$$k_f w_f = \frac{\mu QL}{100w(\Delta P)} \tag{3.39}$$

Where  $w_f$  is the pack thickness in cm

w is the width of the cell in cm

A long fracture half-length ( $x_f$ ) with sufficient fracture conductivity is essential. This could be further explained by the so-called dimensionless fracture conductivity ( $F_{CD}$ ). The dimensionless fracture conductivity, the fracture conductivity in respect to the conductivity capacity of the reservoir defined by Prats (1961) as

$$F_{CD} = \frac{k_f \cdot w_f}{k \cdot x_f} \tag{3.40}$$

Where *k* is reservoir permeability in darcy

 $x_f$  is the fracture half-length in m

To maintain conductivity under increasing load, proppant must be able to withstand the closure stress at the concentration level that it is present in the fracture. The most important characteristics for proppant selection are strength and bulk density, which is based on the stress and conductivity requirements. The measurement of proppant strength is performed by crush test. The results of these tests govern the selection of the proppant for a giving fracturing job. The standard procedure is based on concentration of 4lb/ft² and determination of percent crushed proppant under a specific load (Simo et al. 2013).

Current crush test procedures are defined and standardized in ISO 130503-2. Highlights of the procedures are as follows (Palisch et al. 2009):

- Proppant is pre-sieved to remove particles outside of stated mesh range.
- > Dry proppant placed in steel cell at ~4 lb/ft² (sand equivalent)
- ➤ Room temperature
- Proppant evenly distributed with level surface
- Load applied at uniform rate
- Constant stress maintained for two minutes
- Proppant is sieved. The weight percent which falls below the primary screen is reported.

- For 16/20 proppant all material < 20 mesh is reported as "fines"
- For 30/50 proppant all material < 50 mesh is reported as "fines"

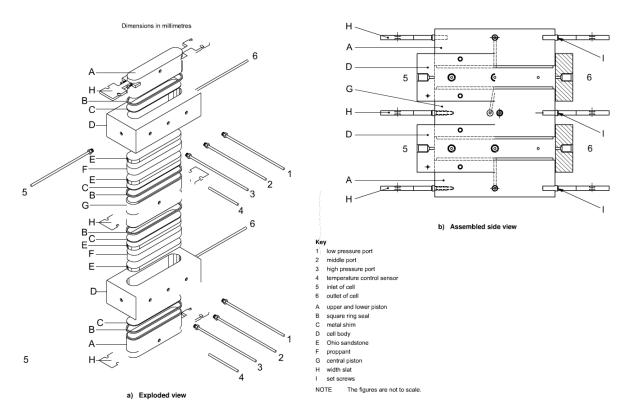


Figure 3.32 Conductivity cell stack, from API RP-19D (2008)

# 4 Modeling of hydraulic fracturing

The first hydraulic fracturing experiment was conducted in 1947 at the Hugoton gas field in Grant County of southwestern Kansas by Stanolind (Charlez 1997, Montgomery & Smith 2010). The first commercially successful application followed in 1950. In the Soviet Union, the first hydraulic proppant fracturing was carried out in 1952. As of 2012, 2.5 million "frac jobs" had been performed worldwide in oil and gas wells; over one million of those within the U.S. (King 2012, Staff 2013). To design and analyze the hydraulic fracturing, which is one of the most frequently used stimulation technique, it is necessary to build mathematical models that can describe it. Hydraulic fracture simulation process presents a complex problem, in which the physical processes involved such as mechanical rock matrix deformation induced by pressure change in fractures and pores; fluid flow within fracture and formation, including their interactions; fracture propagation; proppant transport and settling inside the fracture. These responses are coupled and depend on each other.

Different models were developed in the history. They can be divided into physical, empirical, analytical and numerical models (Economides & Nolte 2000). The physical models are real models (normally with reduced size) and reflect the physical processes. Since such models are related to experiments, it is usually expensive and time consuming. Empirical models are often less expensive and can be generated from observations. Their disadvantage lies on the prediction accuracy for unobserved conditions. The analytical solution is based on mathematical models in the form of equations which captures the main mechanisms of the physical process. Such models are more complicated than the empirical model, but the prediction may be better. However, due to the complexity, some of such equations are not easy to solve. Sometimes this can only be achieved with semi-analytical or numerical methods. Another feature of analytical models is that they often assume simple geometry and ideal distribution of material properties. They can only partially or even not be used to solve complicated real industry problem. However, they can be used to evaluate and verify other models. The numerical model is based on partial differential equations (PDE), but such

equations can be solved with the help of numerical methods. The big advantage is that complex geometry and material property distribution can be simulated, which makes it possible to solve complicated real industry problems.

# 4.1 Historical development of hydraulic fracture modeling

From 1950s the first theoretical models of hydraulic fracturing were introduced and then gradually developed, e.g. PKN and KGD 2D models, lumped and cell-based pseudo 3D models as well as planar 3D model. They were solved by analytical, semi-analytical or fully numerical methods respectively.

# 4.1.1 Modelling of penny-shaped fractures

Sneddon and Elliot (1946) developed an analytical plane strain model to describe the stress state around the fracture and the fluid pressure in the fracture. They have mathematically formulated that Eq. (4.1) can describe the fracture width profile of a penny-shaped (radial and axially symmetric) fracture (Figure 4.1) with a fracture radius of *R*. The radial model is applicable in homogeneous reservoir conditions where the injection region is practically a point source.

$$w(r) = \frac{8P_{net}R(1-v^2)}{\pi E} \sqrt{1 - \frac{r^2}{R^2}}$$
 (4.1)

Where R is fracture length in radial direction [m], r is radial coordinate [m], E is Young's modulus [Pa], v is Poisson ratio [-], which described an ellipsoid, and the volume of the crack V by,

$$v = \frac{16(1 - v^2)R^3}{3E} p_{net} \tag{4.2}$$

Net pressure  $P_{net}$  is defined as the difference between the fluid pressure in the fracture and the pressure against the propagation of the fracture (Fracture closure pressure  $\sigma_c$ ) and in Eq. (4.3) Optimization of Multistage Hydraulic Fracturing Treatment for Maximization of the Tight Gas Productivity

formulated.

$$p_{net} = p_f - \sigma_c \tag{4.3}$$

In ideal case, the fracture closure pressure  $\sigma_c$  can be approximately as minimum principal insitu stress  $\sigma_h$ . However, in fact, both are different, especially in the fracture front. There, the stresses are redistributed by fracture propagation because of the fluid overpressure and fluid lag effect.

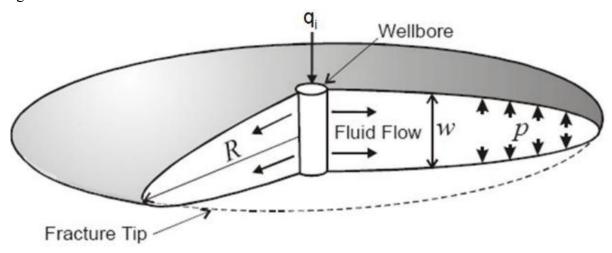


Figure 4.1 Schematic representation of a penny-shaped fracture (Hu & Garagash 2010)

The opening of a propped transverse fracture in horizontal well leads to the reorientation of insitu stress in its neighborhood, which in turn affects the propagation of subsequent main fractures and stress-relief fractures, the so-called stress shadowing (Roussel & Sharma 2011, Taghichian et al. 2014). Sneddon and Elliott (1946) proposed an analytical model to solve stress interference caused by hydraulic fracturing. The components of stress by single propped fracture are described as follows:

$$\frac{1}{2}\left(\Delta\sigma_{x} + \Delta\sigma_{y}\right) = p_{net}\left\{\frac{r}{\sqrt{r_{1}r_{2}}}\cos\left(\theta - \frac{1}{2}\theta_{1} - \frac{1}{2}\theta_{2}\right) - 1\right\} \tag{4.4}$$

$$\frac{1}{2}\left(\Delta\sigma_y - \Delta\sigma_x\right) = p_{net} \frac{r\sin(\theta)}{c} \left(\frac{c^2}{r_1 r_2}\right)^{3/2} \sin\frac{3}{2} (\theta_1 + \theta_2) \tag{4.5}$$

$$\Delta \tau_{xy} = p_{net} \frac{r \sin(\theta)}{c} \left(\frac{c^2}{r_1 r_2}\right)^{3/2} \cos \frac{3}{2} (\theta_1 + \theta_2)$$
 (4.6)

where c is the fracture half-length,  $p_{net}$  is the net pressure in the fracture and the other symbols are explained in Figure 4.2.

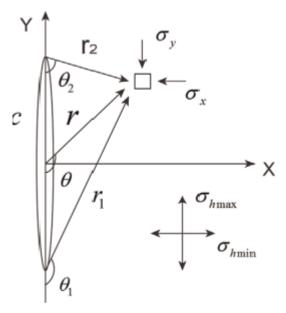


Figure 4.2 Schematic representation of a 2D fracture parameters in Eqs. (4.4) to (4.6) (Liu et al. 2015)

#### 4.1.2 2D model

Some papers published between 1950s and 1970s that developed the foundation of hydraulic fracturing modeling. Two basic models, namely KGD model according to its developers Khristianovich, Zheltov, Geertsma, de Klerk and PKN model developed by Perkins, Kern and Nordgren were developed during this period. KGD and PKN models are 2D plane strain models in which a 3D solid and fracture mechanics problem is converted into a 2D problem. They have taken not only the solid mechanics, but also volume balance into account. In this section, these two models are specifically discussed.

# 4.1.2.1 PKN model

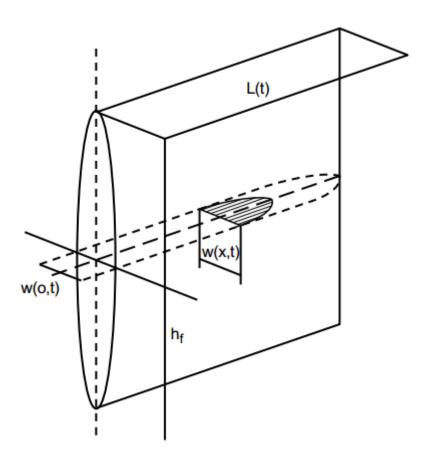


Figure 4.3 Schematic representation of a PKN fracture (Economides & Nolte 2000)

Figure 4.3 shows a PKN fracture. In the PKN model (Perkins and Kern 1961), it is assumed that each vertical cross-section is elliptical and has a limited height  $h_f$ . This is true if the fracture half-length is much larger than the fracture height ( $L >> h_f$ ). The fluid flow in the fracture is assumed to be 1D Newtonian flow, which can be described as follows.

$$\frac{dp}{dx} = -\frac{64qu}{\pi h_f w^3} \tag{4.7}$$

where p is the pressure, x is the distance along the fracture, and  $\mu$  is the fluid viscosity. For the fracture with fixed height, the fracture width and net pressure can be described as (Sneddon and Elliot 1946)

$$w = \frac{2p_{net}h_f(1-v^2)}{E} \tag{4.8}$$

and because the shape of the fracture is elliptical, so that the average width  $\overline{w} = (\pi/4)w$ .

Combing the above two equations, replacing  $q = q_i/2$  and neglecting the leak off and compressibility of the fluid, the following equations can be obtained

$$p_{net}^3 dp_{net} = -\frac{4}{\pi} \frac{\mu q_i E'^3}{h_f^4} dx \tag{4.9}$$

where  $E' = \frac{E}{1-v^2}$  is the plane strain modulus.

By integrating Eq. (4.9) along the fracture half-length L and  $p_{net} = 0$  at the fracture tip, the net pressure can be described as

$$p_{net} = \left[\frac{16\mu q_i E'^3}{\pi h_f^4} L\right]^{1/4} \tag{4.10}$$

Again, Eq. (4.10) can be inserted back into Eq. (4.8). Therefore, Eq. (4.11) described the maximum fracture width of each vertical cross-section.

$$w(x) = 3 \left[ \frac{\mu q_i (L - x)}{E'} \right]^{1/4} \tag{4.11}$$

Eq. (4.10) and Eq. (4.11) are only rough approximations because Perkins and Kern do not take the formulation of the storage and leak off in the fracture into account. Furthermore, Nordgren (1972) derived as the current PKN model by adding the storage and fluid leak off into the model of Perkins and Kern. With consideration of the storage and leak off, the equation of continuity is:

$$\frac{\partial q}{\partial x} + q_L + \frac{\partial A}{\partial t} = 0 \tag{4.12}$$

where q is the volume flow rate through a cross-section [m<sup>3</sup>/s], A is the cross-section area of the fracture (for PKN model  $A = \pi w h_f/4$ ) [m<sup>2</sup>],  $q_L$  is the volume rate of leak off per unit length [m<sup>2</sup>/s].

 $q_L$  can be calculated by Eq. (4.13) according to Carter (1957).

$$q_L = 2h_f u_L \tag{4.13}$$

where  $u_L$  is the leak off velocity at a point on the fracture wall.

$$u_L = \frac{C_L}{\sqrt{t - t_{exp}}} \tag{4.14}$$

where  $C_L$  is the leak off coefficient, t is the current time, and  $t_{exp}$  is the time at which point  $u_L$  was exposed. The cross-sectional area A is not  $A_f$ , the area of the fracture face.

Substituting (4.7), (4.13) into Eq. (4.12) obtains Eq. (4.15), which describes the fracture width a function of time and space.

$$\frac{E'}{128\mu h_f} \frac{\partial^2 w^4}{\partial x^2} = \frac{8C_L}{\pi \sqrt{t - t_{exp}(x)}} + \frac{\partial w}{\partial t}$$
(4.15)

This partial differential equation is only numerically solvable.

### **4.1.2.2 KGD model**

Figure 4.4 shows the KGD Fracture with a fixed height  $h_f$ . Khristianovich and Zhelo (1955) assumed that the fracture width at any distance from the well is height independent. This assumption is the essential difference in comparison with the PKN model. Because of the rectangular shape of the vertical cross-section, the fracture width in the vertical cross-section is independent of the vertical position. This is true, if the fracture height is much larger than fracture half-length ( $h_f >> L$ ). Their solution includes the fracture mechanics aspects of the fracture tip. The flow rate in the fracture is constant and the flow in the fracture is simplified by the fact that most region (in the fracture) has the same fluid pressure as in the borehole, except for a small region near the tip, in which no fluid penetrated.

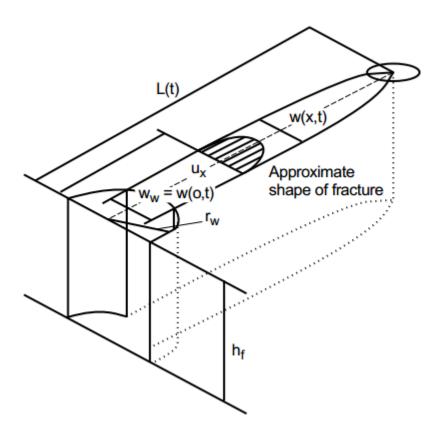


Figure 4.4 Schematic representation of a KGD fracture (Economides & Nolte 2000)

Geertsma and de Klerk (1969) gave a much simpler solution to the problem with the assumption of a very small tip region. Equivalent to Eq. (4.7), Eq. (4.16) applies to the description of the 1D flow in a rectangular fracture.

$$\frac{\partial p}{\partial x} = -\frac{12q\mu}{h_f w^3} \tag{4.16}$$

The fracture width profile of a horizontal cross-section with a small unpressured tip region is almost the same as the profile with constant net pressure over the entire fracture. Thus, the fracture width can be described according to Eq. (4.8) with  $h_f$  is replaced by 2L.

$$w_w = \frac{4}{E'} L p_{net} \tag{4.17}$$

Eq. (4.17) can be solved with the aid of Eq. (4.16). They found expressions of the form given by Perkins and Kern (1961):

$$p_{net} \approx \left[\frac{21\mu q_i}{64\pi h_f L^2} E'^3\right]^{1/4}$$
 (4.18)

with the wellbore width given by

$$w_w = \left[\frac{84}{\pi} \frac{\mu q_i L^2}{E' h_f}\right]^{1/4} \tag{4.19}$$

Geertsma and de Klerk also extended the model with consideration of fluid leak off according to Carter's (1957) method. The volume of a two-wing KGD Fracture is

$$v_f = \frac{\pi}{2} h_f L w_w \tag{4.20}$$

Performing a volume balance and solution procedure like that of Carter, they obtained

$$L = \frac{q_i w_w}{64C_L^2 h_f} \left( e^{s^2} erfc(S) + \frac{2}{\sqrt{\pi}} S - 1 \right)$$
 (4.21)

Where

$$S = \frac{8C_L\sqrt{\pi t}}{\pi w_w} \tag{4.22}$$

# 4.1.3 Planar 3D and pseudo-3D models

The above two 2D models have limitations in their applications, because both assume a fixed fracture height, which can vary from the well (where the pressure is highest) to the fracture tip. Planar 3D models and pseudo-3D (P3D) models can overcome this limitation.

#### 4.1.3.1 Planar 3D model

Planar 3D model assumes that the fracture is planar and oriented perpendicular to the far-field minimum in-situ stress (Economides & Nolte 2000). This model considers a close coupling between deformation and flow processes. Both the fracture width at any point and the overall

shape vary with time.

Hirth and Lothe (1968) and Bui (1977) showed how the fracture width at a point can be described by the net pressure. Not only the net pressure on the calculated point but also the net pressure at any other point has an influence on this point. That means, the width at any point (x, y) is determined by an integral of the net pressure over the entire fracture.

$$w(x,y) = \iint_{S} f(x - x', y - y') (p(x', y') - \sigma(x', y')) dx' dy'$$
(4.23)

where  $\sigma$  is the stress.

The failure criterion normally refers to the fracture mechanics. When the critical stress intensity factor or fracture toughness  $K_{Ic}$  is exceeded, the fracture propagates. The tensile strength criterion in Eq. (4.24) is also frequently used in practice because of its simplicity.

$$p - \sigma_3 > \beta_z \tag{4.24}$$

Where  $\beta_z$  is tensile strength [Pa]. However, the grid-resolution dependency of this criterion must be considered due to the stress concentration near the fracture tip.

The fluid flow in the fracture is assumed as a 2D flow, which contains two basic equations, namely equations for conservation of mass, and the equations for conservation of momentum. The continuity equation Eq. (4.25) is dispensed from 3D to 2D, but taking the leak off effect and the influence of fracture width into account. The gravitational effect is integrated in the flow equation.

$$\left(\frac{\partial(\rho w u_x)}{\partial x} + \frac{\partial(\rho w u_y)}{\partial y}\right) + \frac{\partial}{\partial t}(\rho w) + 2\rho u_L = 0 \tag{4.25}$$

In general, this model is only numerically solvable. The reasons are that all the above three components are coupled. The mobile boundary condition also plays an important role that is difficult to realize.

#### 4.1.3.2 Pseudo-3D model

P3D models were developed in the 1980s. They are built on the basic assumption that the reservoir elastic properties are homogeneous and averaged over all layers containing the fracture height. The pseudo-3D model is derived from the planar 3D model to calculate the fracture problem numerically. The main difference between these two models is the description of the fluid flow in the Fracture. Planar 3D model uses general fluid flow equation and the flow is simplified in the P3D model. Two main types of the P3D model, namely cell-based model and lumped model are discussed in detail in this section.

#### Cell-based P3D model

In cell-based models, fracture length is divided into many discrete cells (Figure 4.5). Any vertical cross-section, as in the case of the PKN model, is assumed as a planar strain. These assumptions make these models suitable if fracture half-length is much larger than fracture height. The fluid flow is taken as 1D along the fracture length, so the fluid pressure is Eq. (4.26)

$$p = p_{cp} + \rho gy \tag{4.26}$$

where  $p_{cp}$  is the pressure along a horizontal line through the center of the perforations and y is the vertical distance from the center of the perforations. This is based on that the vertical fracture extension is sufficiently slow. The pressure gradient due to the vertical flow are not considered. This assumption that the vertical tips of the fracture are approximately stationary always is called the equilibrium-height assumption.

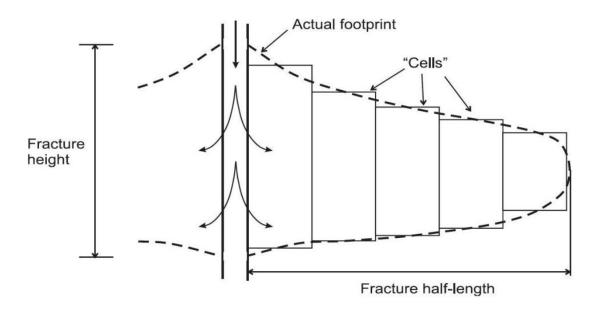


Figure 4.5 Schematic demonstration of the cell-based pseudo-3D fracture geometry (Adachi et al. 2007)

For the mechanic process, Fung et al. (1987) derived a more general solution for nonsymmetric multi-layer cases (Figure 4.6). The stress intensity factors  $K_{Iu}$  at the top and  $K_{Il}$  at the bottom tips can be described by Eq. (4.27) and Eq. (4.28) as a function of the fluid pressure at the perforation center  $P_{cp}$  and the closure stresses in the layer  $\sigma_i$  as

$$k_{Iu} = \sqrt{\frac{\pi h_f}{2}} \left[ p_{cp} - \sigma_n + \rho_f g \left( h_{cp} - \frac{3}{4} h_f \right) \right] + \sqrt{\frac{2}{\pi h_f}} \sum_{i=1}^{n-1} (\sigma_{i+1} - \sigma_i) \left[ \frac{h_f}{2} cos^{-1} \left( \frac{h_f - 2h_i}{h_f} \right) - \sqrt{h_i - (h_f - h_i)} \right]$$
(4.27)

$$k_{II} = \sqrt{\frac{\pi h_f}{2}} \left[ p_{cp} - \sigma_n + \rho_f g \left( h_{cp} - \frac{1}{4} h_f \right) \right]$$

$$+ \sqrt{\frac{2}{\pi h_f}} \sum_{i=1}^{n-1} (\sigma_{i+1} - \sigma_i) \left[ \frac{h_f}{2} \cos^{-1} \left( \frac{h_f - 2h_i}{h_f} \right) - \sqrt{h_i - (h_f - h_i)} \right]$$
(4.28)

where  $\rho_f$  is the fluid density,  $h_{cp}$  is the height at the center of the perforations, and  $h_i$  is the height from the bottom tip of the fracture to the top of the *i*th layer.

To solve these two equations,  $P_{cp}$  is first given. Thus,  $K_{Io}$  and  $K_{Iu}$  are calculated with the current Optimization of Multistage Hydraulic Fracturing Treatment for Maximization of the Tight Gas Productivity

fracture height  $h_f$ . If  $K_{Io}$  and  $K_{Iu}$  exceed the critical stress intensity factor,  $h_f$  changed with an incremental height growth (Eq. (4.29)).

$$h_f^{i+1} = \Delta h_{fo} + \Delta h_{fu} + h_f^i \tag{4.29}$$

where  $\Delta h_{fo}$  and  $\Delta h_{fu}$  is the fracture height increment to the top and bottom, respectively.

This set of nonlinear equations can be solved by iteration. With the known fluid pressure  $P_{cp}$  and the known incremental height growth, the fracture width can be described by Eq. (4.30).

$$w(y) = \frac{4}{E'} \left( p_{cp} + \rho_f g (h_{cp} - y) - \sigma_n \right) \sqrt{y(h_f - y)}$$

$$+ \frac{4}{\pi E'} \sum_{i=1}^{n-1} (\sigma_{i+1})$$

$$- \sigma_i \left[ (h_i - y) cosh^{-1} \left( \frac{y}{|y - h_i|} \frac{h_f - 2h_i}{h_f} + \frac{h_i}{|y - h_i|} \right) \right]$$

$$+ \sqrt{y(h_f - y)} cos^{-1} \left( \frac{h_f - 2h_i}{h_f} \right)$$
(4.30)

where *y* is the elevation measured from the bottom tip of the fracture.

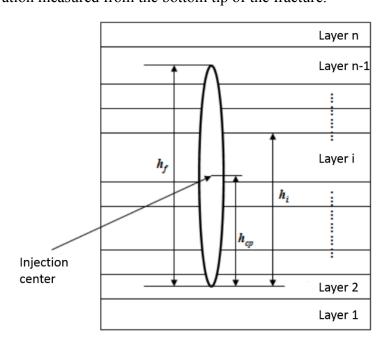


Figure 4.6 Definition of variables for the fracture containment problem (modified from Economides & Nolte 2000)

The fluid pressure  $P_{cp}$  are derived from the flow process. For each vertical cross-section the continuity equation Eq. (4.31) and the flow equation Eq. (4.32) are

$$\frac{\partial Au}{\partial x} + \frac{\partial A}{\partial t} = -2\sum_{i} (u_L h_L)_i \tag{4.31}$$

$$\bar{u}_x = -\frac{w^2}{12\mu} \frac{\partial p}{\partial x} \tag{4.32}$$

where A is the vertical cross-sectional area,  $\bar{u}_x$  is the average cross-sectional velocity,  $u_L$  and  $h_L$  are the leak off rate and height in each layer.

To solve this model generally there are some numerical methods, e.g. FDM with limitation of time discretization and time-sharing method without limitation of time discretization.

# Lumped P3D model

Lumped models are an alternative to cell-based models and were first introduced by Cleary (1980b). In the Lumped P3D model, the fracture propagation form is assumed as two-half-ellipses joined at their centers in the fracture length direction (Figure 4.7). The fracture length, top half-ellipse, and bottom half-ellipse are calculated at each time step. Generally, the horizontal and vertical fracture propagation is calculated by PKN and KGD model, respectively. For example, Eqs. (4.33) to (4.36) are analogous to the KGD model.

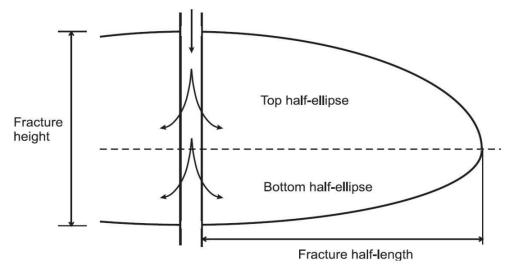


Figure 4.7 Schematic demonstration of the fracture geometry based on lumped p3D model (Adachi et al. 2007)

The continuum equation is

$$\rho(q\overline{w} - Lq_L) = \frac{d(r_3\rho\overline{w}L)}{dt}$$
 (Continum equation) (4.33)

where

$$\overline{w} \approx \frac{r_1 p_{net}}{F} L \tag{4.34}$$

$$q^m \overline{w}^m \approx \frac{r_5^m (\overline{w})^{2n+2}}{L^2}$$
 (Power law flow equation) (4.35)

where

$$r_5^m = \frac{r_2 r_4 E}{r_1 \mu} \tag{4.36}$$

This is analogous to the power law flow equation. The effort should be invested in the determination of the unknown coefficients  $\gamma_I$  to  $\gamma_5$  by detailed simulations, laboratory experiments or field studies. This part will not be discussed in detail.

# 4.2 Real 3D hydraulic fracture modeling with coupled THM effects

MFrac and FracPro are the most widely used simulators in the Petroleum Engineering industry. However, they still have some deficiency, e.g. plain strain assumption, empirical leak-off model, full fracture closure with proppant contact cannot be simulated appropriately. In MFrac the simulation is forced to stop when the proppant reaches its maximum value of the compacting factor, even when the most area of the fracture upper part is still open without proppant (full closure is not yet reached). That means, the area of the proppant placement is underestimated. In FracPro, the proppant fills the created fracture after complete full closure. But, the proppant will sink to the lower part of the fracture due to the settling effect. It indicates that the area of the proppant placement is overestimated. The problems of both models are that they do not consider the hydro-mechanical conditions under contact. In fact, the fluid pressure within fracture under contact could be smaller than the normal stress perpendicular to the fracture wall.

Therefore, it is difficult to simulate the compact proppant at the upper part of the fracture during the closure process.

Based on the above-introduced hydraulic fracturing models Zhou and Hou (2013) has developed a new approach for simulating hydraulic fracture propagation, which treats fracture propagation in a 3D geometric model under 3D stress state with fully hydro-mechanical coupling effect between fracture and matrix and integrated into the software FLAC3D (Itasca, 2009). The proppant transport with settling effect and fracture contact in consideration of proppant placement were further implemented in Zhou et al. (2014). In addition, Feng et al. (2016) has extended the model to take the heat transport within fracture and heat exchange between the fracture and the surrounding reservoir rocks into account. Thus, coupled THM effects during the hydraulic fracturing process in a tight gas reservoir are considered together. As the intrinsic components of FLAC3D are partly used in the investigations, the modified software with this set of plug-in components is named FLAC3D<sup>plus</sup>. The basic modeling concept for the new approach in FLAC3D<sup>plus</sup> is almost the same as for the PL3D model with a fixed rectangular mesh. They are different only in their mathematical details to describe the mechanical, hydraulic and thermal behavior, including their coupling during the calculations. The numerical formulation of the developed model to simulate hydraulic fracturing in tight gas reservoirs are listed in Zhou et al. 2014 and Feng et al. 2016.

### 4.2.1 Governing equations for mechanical deformation

As introduced in Zhou and Hou (2013), the created fracture is assumed as an aperture between two parallel plates perpendicular to the minimum horizontal stress. 3D mechanical calculation is based on the elasto-plasticity theory. Solving the equation of motion Eq. (4.37) in a dynamical process to get the displacement increment in a time interval is the key point. By using continuum Eq. (4.38) and constitutive equation Eq. (4.39), the strain and the stress increment could be further estimated.

$$\sigma_{ij,j} + \rho \left( b_i - \frac{dv_i}{dt} \right) = 0 \tag{4.37}$$

$$\Delta \varepsilon_{ij} = \frac{1}{2} \left( \Delta u_{i,j} + \Delta u_{j,i} \right) \tag{4.38}$$

$$\Delta \sigma' = D \Delta \varepsilon \tag{4.39}$$

where  $\sigma = \sigma' + \alpha I P_p$ ,  $\sigma$  is total stress [Pa],  $\rho$  is density [kg/m³];  $b_i$  is gravity acceleration [m/s²],  $v_i$  is velocity [m/s],  $\Delta \varepsilon$  is strain increment [-], u is displacement [m],  $\Delta \sigma'$  is effective stress increment [Pa],  $\alpha$  is biot-coefficient [-], I is the unit matrix and D is physical matrix, i, j  $\in$  (x, y, z).

As introduced in Zhou et al. (2014), an extra strain increment induced by pressure change in the fracture was added in the total strain increment to describe the discontinuous behavior of fracture. In Figure 4.8 a tensile fracture penetrates through the center of one-row elements. During the hydraulic fracturing the fluid pressure in the fracture changes due to the fluid flow or leak off. The pressure change will only lead a strain change in the direction perpendicular to the fracture. Under these considerations, the strain change perpendicular to the fracture can be expressed as Eq. (4.40).

$$\Delta \varepsilon_f = \frac{P_f(t+1) + \sigma_n(t)}{\alpha_1} \tag{4.40}$$

where  $\varepsilon_f$  is strain induced by change of fluid pressure in fracture [-],  $P_f$  is fluid pressure in fracture [Pa],  $\sigma_n$  is the normal stress perpendicular to the fracture [Pa],  $\alpha_1$  is material constants defined in terms of the shear modulus, G, and bulk modulus, K, as

$$\alpha_1 = K + \frac{4}{3}G\tag{4.41}$$

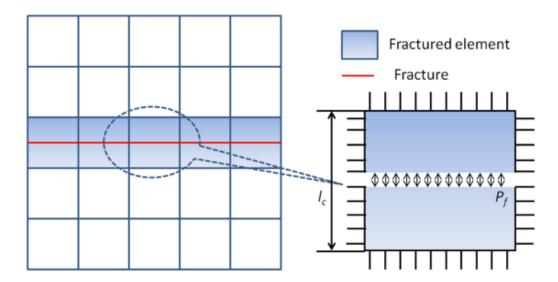


Figure 4.8 Demonstration of fracture elements in the geometrical model (left); load condition in one fracture element at the frozen time point (right) (Zhou et al. 2014)

Therefore, according to Hook's law the change of the stress in the three orthogonal directions at the current time step is

$$\sigma_n(new) = \sigma_n(old) - \alpha_1 \Delta \varepsilon_f \tag{4.42}$$

$$\sigma_{1,2}(new) = \sigma_{1,2}(old) - \alpha_2 \Delta \varepsilon_f \tag{4.43}$$

where  $\sigma_{l,2}$  is the stress in another two principal directions,  $\alpha_2$  is material constants defined in terms of the shear modulus, G, and bulk modulus, K, as

$$\alpha_2 = K - \frac{2}{3}G\tag{4.44}$$

If the element dimension which normal to the fracture is small, then the change of the fracture width can be approximated as Eq. (4.45)

$$\Delta w = \varepsilon_f l_c = \frac{p_f(t+1) + \sigma_n(t)}{\alpha_1} l_c \tag{4.45}$$

where w is the fracture width [m] and  $l_c$  is the element length which normal to the fracture [m]. As Eq. (4.45) states, If  $P_f > |\sigma_n|$ , the fracture width will be enlarged. If  $P_f < |\sigma_n|$ , the fracture width will be reduced. Physically the fracture width cannot be negative or zero because surface roughness prevents complete mechanical closure of a fracture. Therefore, it is necessary to Optimization of Multistage Hydraulic Fracturing Treatment for Maximization of the Tight Gas Productivity

impose a minimum constraint  $w_{res}$  (we permit  $w_{res} > 0$ ) on the width

$$w > w_{res} \tag{4.46}$$

In fact, when the proppant concentration reaches its maximum value (compacted proppant) or the fracture width reduced to the minimum constraint width  $w_{res}$ , which means the fracture wall has already contacted with proppant or its self. Then the fracture width will not reduce any more, even if the normal stress is larger than the fluid pressure. In this situation, a contact stress appears which must be considered, so that Eq. (4.45) can be rewritten as follows:

$$\Delta \varepsilon_f = \frac{P_f(t+1) + \sigma_{con}(t) + \sigma_n(t)}{\alpha_1} \tag{4.47}$$

where  $\sigma_{con}$  is the contact stress with

$$\begin{cases} \sigma_{con}(t+1) = 0 & \text{if } C \le C_{max} \text{ and } w \ge w_{res} \\ \sigma_{con}(t+1) = \sigma_{con}(t) + \alpha_1 \Delta \varepsilon_0 \text{ if } C > C_{max} \text{ and } w < w_{res} \end{cases}$$

$$(4.48)$$

and  $\Delta \varepsilon_o$  is over reduced strain [-].

After the recalculation of the stress in the fracture element by using Eqs. (4.42) and (4.43), the constraint condition around it will be removed. The influence of the stress redistribution can thus be considered.

### 4.2.2 Fracture propagation

The fracture propagation criterion describes a very special type of tip boundary condition. Usually, numerical models obey the conventional LEFM (linear elastic fracture mechanics) criterion (Eq. (4.49)), that the fracture propagates if (Adachi et al. 2007)

$$K_I = K_{Ic} \tag{4.49}$$

where  $K_I$  is the stress intensity factor (the strength of the inverse square-root stress singularity at the tip),  $K_{Ic}$  is the toughness (a material property of the rock). At the field site, the fracture propagation by hydraulic fracturing treatment is predominated by the combination of viscous dissipation and leak-off. Under these circumstances, the classical LEFM stress singularity is

restricted to a very small length scale near the tip (Garagash & Detournay, 2005).

The modeling in FLAC3D (Itasca, 2009) is consist of the fixed mesh. For simplicity, the linear cohesive zone model in FLAC3D<sup>plus</sup> (Zhou et al. 2014) can used to determine the fracture propagation. Therefore, the fracture propagation criterion can be reduced to a stress-based criterion. If the effective stress (considering the influence of the pore pressure) exceeds the critical traction stress (tensile strength), then the cohesive energy is fully dissipated and the fracture propagates further (Carrier et al. 2011). The critical traction stress is the physical property of the rock formation that is independent of the applied loading, which means it is convenient for the numerical implementation.

The precondition for applying the stress based fracture propagation criterion is the small size of the fracture tip element. Therefore, Zhou et al. (2014) introduced an improvement for the correction of the strain calculation by fracture propagation. In the calculation model of Zhou et al. (2014), all elements are divided into three groups: fractured, partially fractured (fracture tip) and non-fractured elements (Figure 4.9). The fracture propagation criterion is only applied on the partially fractured elements. As mentioned earlier, the mesh is fixed in the modeling, so the partially fractured elements should be subdivided into some sub elements (with a dimension of 0.1 m x 0.1 m). Now the stress based fracture propagation criterion can be applied on the sub elements. If the effective stress exceeds the critical traction stress, the non-fractured sub element will be converted to the fractured sub element, which from now on serves as the pathway for fluid flow. If all the sub elements are cracked, the partially fractured elements will be converted to the fractured elements. Simultaneously the fracture tip elements will be automatically judged and updated. For the consideration of the partially fractured elements, Zhou et al. (2014) introduced a correction of strain calculation (Eq. (4.50)) in the fracture tip element with consideration of the ratio between the opened and the total area of a tip element, which is analogous to the method used in Napier and Stephansen (1987).

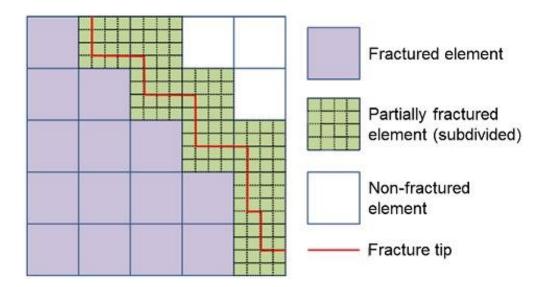


Figure 4.9 Classification and geometrical relationship of the fractured elements, partially fractured elements with the fracture tip and non-fractured elements (modified from Zhou et al. 2014)

$$\Delta \varepsilon_f = \frac{P_f(t+1) + \sigma_{con}(t) + \sigma_n(t)}{\alpha_1} \frac{A_{open}}{A_{tip}}$$
(4.50)

where  $A_{open}$  is the area of the opened fracture in a tip element [m<sup>2</sup>],  $A_{tip}$  is the area of a tip element [m<sup>2</sup>].

The numerical formulation and verification of the developed model mentioned above to simulate hydraulic fracturing in tight gas reservoirs was proved in the paper of Zhou et al. (2014).

## 4.2.3 Governing equations for solid-liquid two phase flow in the fracture

The flow process has three parts in the hydraulic fracturing: flow in fracture, flow in rock formation and flow exchange between them. The injected slurry is a mixture of proppant and fluid, which can be treated as a two-component, interpenetrating continuum. The rheology of the mixture is strongly dependent on the proppant volumetric concentration.

The researchers who investigated the relationship between the slurry viscosity and the proppant

concentration have done some experiments. Barree and Conway (1995) have derived a mathematical model through published correlations (Eq. (4.51)).

$$\mu_a = \mu_0 \left( 1 - \frac{C}{C_{max}} \right)^{-a} \tag{4.51}$$

where  $\mu_a$  is the apparent viscosity of the slurry [Pa·s],  $\mu_0$  is the effective Newtonian viscosity of the clean fluid [Pa·s], C is the proppant concentration [kg/m³],  $C_{max}$  is the maximum/saturation proppant concentration [kg/m³] and a is the correlation coefficient [-] (usually 1 < a < 3). The effect of Eq. (4.51) is to increase the viscosity of the slurry as the proppant concentration increases ( $\mu_a$  increases very rapidly as C approaches  $C_{max}$ ). In the industrial field operation, the most commonly used injection fluid is gel, e.g. guar solution, which has a high viscosity. That means, as concentration increases, it is expected that the slurry will start to behave more like a solid than a fluid. In the lower shear rate region, it behaves like the Newtonian fluid. But in the higher shear rate region, it is comparable to the shear-thinning fluid. Hence, the use of a lubrication-type equation (even with a very high viscosity) to model the slurry transport may become inappropriate. To describe the relationship between slurry viscosity and proppant concentration Eissa et al. (2007) developed a model (Eq. (4.52)), in which the lower, higher and transition shear rate regions were considered.

$$\mu_{a} = \mu_{0} \left( 1 - \frac{C}{C_{max}} \right)^{-a} \frac{\tan^{-1} \left( \frac{r}{r_{L}} \right)^{n-1}}{\tan^{-1} \left( \frac{r}{r_{H}} \right)^{n-1}}$$
(4.52)

where  $\gamma$  is apparent shear rate [1/s],  $\gamma_L$ ,  $\gamma_H$  are parameters [1/s] and n is power law coefficient [-].

In FLAC3D there is no option for simulating fracture flow but only native function for fluid flow in porous medium. Therefore, Zhou and Hou (2013) implemented a built-in flow simulator FTP3D (pseudo-3D simulator for fracture flow) in FLAC3D through the user interface. The slurry flow in the fracture is normally assumed as the flow between two parallel planes. Its averaged velocity can be derived from the Navier-Stokes equation (Eq. (4.53)), which is the so-called cubic flow or lubricant flow. If the slurry is assumed incompressible, the

mass conservation equation could be simplified to the volume conservation equation (Eq. (4.54)). The fracture aperture, the pressure gradient, the slurry density variation and the apparent viscosity control the movement of the slurry. Substituting Eq. (4.53) into Eq. (4.54), then Eq. (4.55) is obtained, which can be solved numerically.

$$v_s = -\frac{w^2}{12\mu_a} \frac{\partial (p_f + \rho_s gz)}{\partial x} \tag{4.53}$$

$$\frac{\partial w}{\partial t} + \nabla \cdot (v_s w) + w Q_s = 0 \tag{4.54}$$

$$w(Q_{inje} + Q_{leak}) + \frac{\partial w}{\partial t} = \nabla \cdot \left[ \frac{w^2}{12\mu_a} \nabla (p_f + \rho_s gz) \right]$$
(4.55)

where  $v_s$  is slurry velocity [m/s],  $\rho_s = C\rho_p + (1 - C)$  is slurry density [kg/m³],  $\rho_p$  is proppant density [kg/m³],  $\rho_l$  is liquid density [kg/m³], g is gravity acceleration [N/s²], z is elevation [m],  $q_s$  is source [1/s],  $Q_{lnje}$  is injection source [1/s],  $Q_{leak}$  is leak-off source [1/s].

To characterize the proppant transport, the mass conservation equation Eq. (4.56) is used and implemented in FLAC3D<sup>plus</sup>. The proppant velocity in Eq. (4.56) is estimated by using the model introduced in Gadde et al. (2004), Gadde and Sharma (2005), Liu (2006). The diffusion term caused by concentration gradient is neglected because of the relative much bigger advection velocity than the diffusion one.

$$\frac{\partial(Ct)}{\partial t} + \nabla \cdot (Cwv_p) + C_{inje.}Q_{inje.} = 0$$
(4.56)

where  $v_p$  is the proppant velocity vector,  $C_{inje}$  is the proppant concentration in the injected slurry [-].

#### 4.2.4 Flow interaction between the fracture and the formation

One of the key issues in designing a fracture treatment is accurate knowledge of how rapidly fluid will leak out of the fracture into the reservoir, namely the leak-off process. It is induced by the pressure difference between the fracture and the formation pores and has significant influence on fracture propagation, proppant transport and stress distribution in the formation

due to the change of the pore pressure. Zhou and Hou (2013) and Zhou et al. (2014) introduced a method to describe the leak-off process that implemented in FLAC3D. In this method, the exchange area is the fracture wall and a stationary Darcy flow caused by the pressure gradient between the fracture and the formation pores is assumed in each time step. The exchange volume at this time step can be approximated by Eq. (4.57), which will be further treated as the source term in Eq. (4.55). The fluid flow in the porous medium is numerically modeled based on the Darcy flow and the mass conservation (Zhou and Hou, 2013) and the pore pressure varied during the fluid injection.

$$Q_{leak(t+1)} = \frac{k_m s}{\mu_a} f(P_{f(t)} - P_{p(t)})$$
(4.57)

where  $Q_{leak}$  is the exchange volume [m<sup>3</sup>/s], f is the infiltration coefficient [1/m], S is the exchange area [m<sup>2</sup>],  $K_m$  is the matrix permeability [m<sup>2</sup>],  $P_f$  and  $P_p$  is the fluid pressure in the fracture and formation pores [Pa].

#### 4.2.5 Governing equations for the heat transport

Not only the coupled hydro-mechanical processes but also thermal process take place during the hydraulic fracturing. The temperature distribution derived by means of the heat transport equations. The heat transport includes heat conduction, heat convection and heat radiation. In this section, heat conduction and heat transfer are introduced for the implementation in the thermal module.

Heat conduction is defined as the heat flux in a continuum, or between two directly connected substances (solid or fluid) which caused by the temperature gradient. The heat flow equation (Eq. (4.58), Fourier 1878), the continuity equation (Eq. (4.59), Lamb 1916) and the thermal constitutive equation of materials (Eq. (4.60), Halliday et al. 2013) are integrated to describe this process mathematically.

$$q_i = -\lambda \frac{\partial T}{\partial i} \tag{4.58}$$

$$-\left(\frac{\partial q_x}{\partial x} + \frac{\partial q_y}{\partial y} + \frac{\partial q_z}{\partial z}\right) + q_v = \frac{\partial H}{\partial t}$$
(4.59)

$$\frac{\partial H}{\partial t} = \rho c_v \frac{\partial T}{\partial t} \tag{4.60}$$

where  $q_i$  is the heat flow [W/m²] in the i direction (i = x, y, z),  $\lambda$  is the thermal conductivity [W/(m·°C)], T is the temperature [°C],  $q_v$  is the heat source of volume [W/m³], H is the stored heat per unit volume [J/m³],  $\rho$  is the density [kg/m³] and  $c_v$  is the specific heat capacity [J/(kg·°C)].

Integrated the above Equations obtained the heat conduction equation (Eq. (4.61)).

$$\lambda \frac{\partial^2 T}{\partial x^2} + \lambda \frac{\partial^2 T}{\partial y^2} + \lambda \frac{\partial^2 T}{\partial z^2} + q_v = \rho c_v \frac{\partial T}{\partial t}$$
(4.61)

Heat convection describes the heat exchange process between the flowing fluid (in the fracture) and the solid rock formation. Two systems of different phases exchange their thermal energy (Figure 4.10) and the driving force is the temperature gradient. In addition, the intensity of the heat exchange can also be influenced by other factors, e.g. fluid flow rate, surface roughness of the fracture walls.

In the new heat transport module (Feng et al. 2016), all the influence factors are considered through an overall convective heat-transfer coefficient *h*. In FLAC3D, a convective boundary condition has the form (Eq. (4.62), Itasca 2009)

$$q_n = h(T - T_e) (4.62)$$

where  $q_n$  is the component of the flux normal to the boundary in the direction of the exterior normal, h is the convective heat-transfer coefficient [W/m<sup>2</sup>°C], T is the temperature of the solid boundary surface, and  $T_e$  is the temperature of the surrounding fluid [°C].

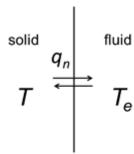


Figure 4.10 Convective heat exchange between flowing fluid and solid rock formation

Zhou & Hou (2013) assumed the fracture propagation to be a planar problem. Thus, the heat transport in the fracture system (Feng et al. 2016) are simplified to be two-dimensional. Unlike FLAC3D, the new thermal module for FLAC3D<sup>plus</sup> has been implemented in the simulator using the Finite Volume Method with the consideration of the heat conduction and convection in fractures, as well as the heat transfer between the flowing fluid and the rock formations. That means, the thermal influence on the mechanical behavior of the rock formations has been taken into consideration through the intrinsic thermal module in FLAC3D.

#### 4.2.6 Coupled THM effects between each of the processes

The governing equations for the coupled THM processes during hydraulic fracturing are introduced and listed in the previous sections. Each sub-process has its own variables (e.g. stress, strain, displacement in mechanical deformation; fracture fluid pressure, fracture fluid velocity in fracture flow; proppant concentration in proppant transport; pore pressure, pore flow velocity in porous flow; and temperature of rock formation/fracture fluid in heat transport). These processes are coupled strongly with each other (Figure 4.11). The coupling effect has a great impact on the modeling results and thus must be taken into consideration.

#### Fracture flow ← Mechanical deformation

In hydraulic fracturing, the existing fracture is a discontinuous field and is formed by two fracture walls (i.e. boundary surface of the rock formation). During the fluid injection, the

fracture fluid pressure will increase and act on the fracture walls that leads to the stress change of the boundary surface. Thus, the mechanical deformation of the rock formation will happen. Then the fracture width will change and leads further to the change of the fracture conductivity and then affects the pressure distribution.

#### Fracture flow $\leftrightarrow$ Porous flow

During the hydraulic fracturing operation, the injected fluid will infiltrate from fracture into rock formations. This process is triggered by the pressure gradient between fracture and pores and called leak-off. In the leak-off process, mass conservation must obey, and leak-off rate is strongly dependent on the pressure gradient, which couples the fracture and the porous flow.

#### **Porous flow** ← **Mechanical deformation**

Due to the fluid leak-off, the pore pressure increased, and the effective stress decreased. This leads to the deformation of the rock formations. On the other hand, the pores expand, which leads to the change of the porosity as well as the storage capacity of the pores. The rock formation permeability will also be influenced.

#### Fracture flow ↔ Proppant transport

During the hydraulic fracturing operation, the proppant (solid particle) is added to the injected fluid to prevent the fracture from full closure after shut-in. It is a mixture of proppant and fluid called slurry and is a two-phase two-component flow problem. The drag force derived from the velocity difference between the solid and fluid is the coupled interaction forces between them.

#### **Proppant transport** ← Mechanical deformation

After shut-in, fracture will gradually close due to the fluid leak-off into the formation. At certain time point, the fracture wall will get in contact with the proppant and then the compaction process of the proppant starts. Once the maximum proppant compaction (i.e. the maximum proppant concentration) is achieved, further fracture closure and fracture width reduction could not happen anymore.

### Fracture flow $\leftrightarrow$ Heat transport

The fluid flow within the fracture will transport the heat at the same time. This is the heat convection process.

#### **Heat transfer** ↔ **Mechanical deformation**

Due to the heat conduction and heat advection derived from the fluid leak-off, the decrease of the formation temperature leads to an extra tensile stress in the rock formation. Therefore, the minimum horizontal stress around the fracture decreases. Thus, the fracture is easier to open and leads to the change of the fracture geometry (mechanical deformation).

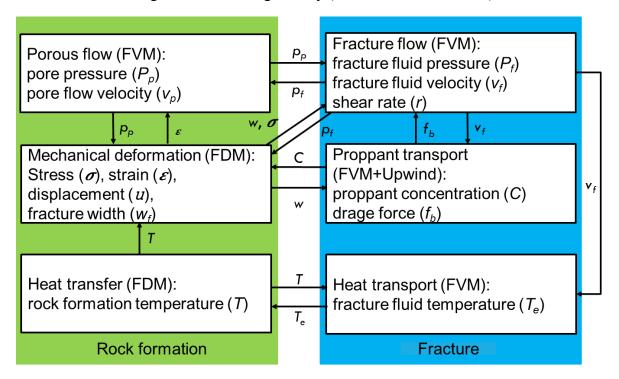


Figure 4.11 Schematic demonstration of the coupling effects between the sub-processes in hydraulic fracturing

# 5 Development of the Frac- and FracProdu-Simulator for the optimization of multistage hydraulic fracturing

In this dissertation an innovative numerical tool chain was developed for the optimization of the whole process from multiple hydraulic fracturing till production in the tight gas reservoir. The full 3D hydraulic fracturing model of FLAC3D<sup>plus</sup> was linked with the robust design optimization (RDO) simulator optiSLang. To simulate the gas production process in the stimulated gas reservoir, the parallel multi-phase multi-component reservoir simulator TMVOCMP was also linked. The details of the model development and verification were introduced in the following sections.

# 5.1 RDO simulator optiSLang

optiSLang is a CAE-based software for sensitivity analysis, multi-objective and multi-disciplinary optimization, robustness evaluation, reliability analysis and robust design optimization (RDO) (Dynardo 2014).

The goal of the optiSLang is the improvement of the existing designs and creation of optimal new designs.

With the help of sensitivity analysis, the designer identifies the variables which contribute most to a possible improvement of the optimization goal. Based on this identification, the number of design variables can be dramatically reduced and an efficient optimization can be performed. There are three sensitivity analysis methods (Variance based sensitivity analysis, Polynomial based sensitivity analysis, Meta-modelling e.g. Kriging, neural networks), which are very suitable as an optimization-preprocessing tool. However, all of them have some disadvantages and limitations (Table 5.1). To overcome these problems, Dynardo developed the Metamodel of Optimal Prognosis (Most & Will 2008). In this approach, the optimal input variable subspace together with the optimal meta-model are determined with the help of an objective- and model-independent quality measure, namely the Coefficient of Prognosis (CoP).

Table 5.1 Comparison of the different sensitivity analysis methods

Methods	Advantage	Disadvantage		
Variance based sensitivity	Directly quantify the	Huge numerical effort		
analysis	proportion of the output			
	variance			
Polynomial based sensitivity	Model response	Strong over-estimation of the		
analysis	approximated by a	approximation quality;		
	polynomial basis function of	limitation to polynomial		
	linear or quadratic order with	regression		
	or without coupling terms			
Meta-modeling, e.g. Kriging,	Model response represented	Not clear which one most		
neural networks	by surrogate functions in	suitable for which problem;		
	terms of the model inputs	limitation to a small number		
		of input variables		
Metamodel of Optimal	Determine optimal input	Parameters show larger		
Prognosis (Dynardo)	variable subspace together	deviation		
	with the optimal Metamodel			
	with help of CoP			

optiSLang automatically identifies the relevant input and output parameters and quantifies the forecast quality with the help of the Coefficient of Prognosis (CoP) and the Metamodel of Optimal Prognosis (MOP). A predictable prognosis quality is the key to an efficient optimization. Thus, a "no run too much" philosophy can be implemented to minimize solver calls. Consequently, even optimization tasks involving many variables, scattering parameter as well as non-linear system behavior can be solved. optiSLang's Best-Practice-Management automatically selects the appropriate algorithms, such as gradient methods, genetic algorithms, evolutionary strategies or Adaptive Response Surface Methods. Furthermore, all methods of optimization and stochastic analysis can be combined concerning the task.

In (Most & Will 2008) a model independent measure to assess the model quality was proposed. This measure is the Coefficient of Prognosis (CoP), which is defined as follows Eq. (5.1) and Eq. (5.2).

$$CoP = 1 - \frac{SS_E^{Prediction}}{SS_T} \tag{5.1}$$

$$SS_T = \sum_{i=1}^{N} (y_i - \mu_Y)^2 \tag{5.2}$$

where N is the number of samples,  $y_i$  are the sample values, and  $\mu_Y$  is the mean value.  $SS_E^{Prediction}$  is the sum of squared prediction errors. These errors are estimated based on cross validation,  $SS_T$  is equivalent to the total variation of the output Y.

In principle optiSLang is a tool used for graphical programming. Two important components (Dynardo, 2014) provide a base for this (Figure 5.1):

- Nodes: Nodes can be separated in Input, Process/Properties and Output.
- Connections: Connections are used to manage the data flow between two nodes and to trigger the successor node.

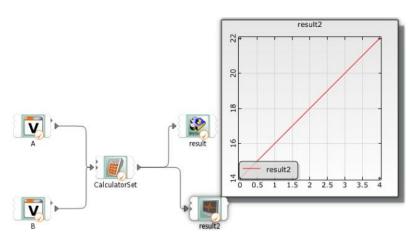


Figure 5.1 Basic data flow of optiSLang (Dynardo, 2014)

The flowchart of optiSLang sensitivity analysis (Figure 5.2a) and single-objective optimization (Figure 5.2b) is shown below (Dynardo, 2014). With the help of sensitivity analysis, the designer identifies the variables that contribute most to a possible improvement of the optimization goal. Based on this identification, the number of design variables may be

dramatically reduced and an efficient optimization with better start designs can be performed.

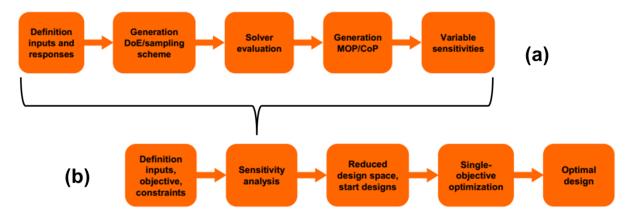


Figure 5.2 Flowchart of optiSLang sensitivity analysis (a) and single-objective optimization (b) (modified from Dynardo 2014)

# 5.2 The coupled Frac-Simulator optiSLang-FLAC3D<sup>plus</sup>

Figure 5.3 shows the coupling concept of the simulator optiSLang-FLAC3D<sup>plus</sup>. Every time optiSLang modifies the input data and then call FLAC3D<sup>plus</sup> to run it. After the simulation, optiSLang read and judge the output data, which export from the FLAC3D<sup>plus</sup>, till the optimization criteria reached.

The flowchart of the simulator optiSLang-FLAC3D<sup>plus</sup> for hydraulic fracturing simulation is described in Figure 5.4. First, input parameters and design variables will be defined in input.dat. Then, output- and reference signals should be defined as output/reference.tab. After that, signal functions (variables), optimization criteria (error\_norm/objective) and the solver call (solver.bat) will be defined. After all the predefinition a sensitivity analysis, global- and local optimization will run in sequence in optiSLang-FLAC3D<sup>plus</sup>. According to the above results the uniqueness of the solution will be checked at last.

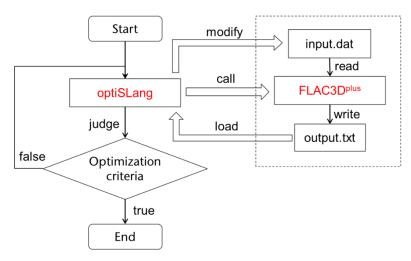


Figure 5.3 Coupling concept of the simulator optiSLang-FLAC3D<sup>plus</sup>

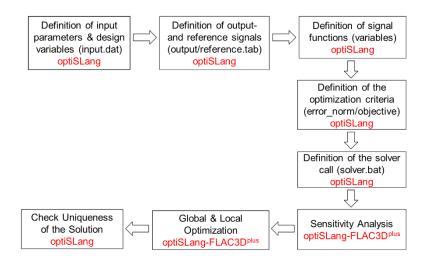


Figure 5.4 Flowchart of the simulator optiSLang-FLAC3D<sup>plus</sup> for hydraulic fracturing simulation

#### 5.3 Verification of the Frac-Simulator

In this section, we use fictive reservoir models to demonstrate inverse parameters calculation with optiSLang-FLAC3D<sup>plus</sup> by hydraulic fracturing.

#### 5.3.1 Problem definition

For the numerical investigation, a generic ¼ model is used (Figure 5.5a). The model lies at a

depth between 3,000 and 3,200 m and consists of three major rock formations, namely the caprock (50 m), the reservoir (100 m), and the basement (50 m). They are assumed to be siltstone, sandstone, and siltstone, respectively. The whole model has a dimension of 200, 300, 200 m and is discretized into 21,175 rectangle elements. The near-fracture elements are finely discretized for better modeling of the fracture propagation, and the mesh elements of the fracture have a width of 2 m.

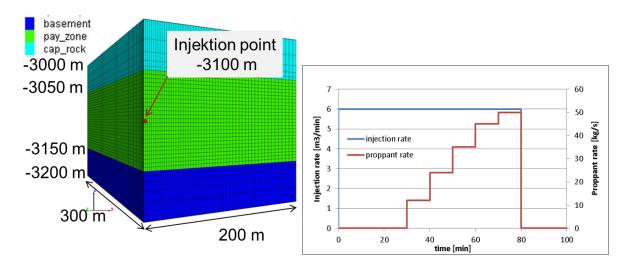


Figure 5.5 (a) Generic 3D ¼ model for the numerical simulations; (b) Hydraulic fracturing treatment schedule

The duration of the whole simulated fracturing treatment was 100 min. The slurry injection with a constant rate of 6 m³/min took place in the whole 80 min (Figure 5.5b). The density of the fracturing fluid was assumed as 1040 kg/m³ and viscosity as 0.1 Pa·s. The injected proppant was typical fracturing sand (density 3500 kg/m³, diameter 0.67 mm), and its concentration which in consideration of the slurry injection rate was increased with time until it attained a maximum value of 50 kg/s after about 70 min. After 80 min, the injection well was shut-in. The mechanical and hydraulic properties for the three rock formations are listed in Table 5.2.

Table 5.2 Mechanical and hydraulic properties of the rock formations in the calculation model

Rock formation	$\rho  [\text{kg/m}^3]$	E [GPa]	v [-]	$\sigma_t$ [MPa]	φ [-]	k [m <sup>2</sup> ]
Caprock (siltstone)	2650	25	0.3	1.0	0.025	1 x 10 <sup>-17</sup>
Reservoir	2600	30	0.25	1.0	0.1	1 x 10 <sup>-15</sup>

Optimization of Multistage Hydraulic Fracturing Treatment for Maximization of the Tight Gas Productivity

(sandstone)						
Baserock (siltstone)	2650	25	0.3	1.0	0.025	1 x 10 <sup>-17</sup>

To achieve optimal adaptation to the reference function the parameter should be predefined. Here three parameters and their bounds were predefined (start value = 0.075):

$$f = 0.075$$
, fwe  $\in [0.01, 1]$ 

$$\mu_0 = 0.075$$
, miu $0 \in [0.004, 0.87]$ 

$$b = 0.075, b \in [0.01, 1]$$

$$k_f = f \frac{w_f^2}{12} \tag{5.3}$$

$$m = \frac{k}{\mu_0 b} \tag{5.4}$$

where f is the fracture surface roughness parameter [-],  $\mu_0$  is the fluid viscosity [Pa·s], b is the leak-off regulation parameter [-],  $k_f$  is the fracture permeability [m<sup>2</sup>],  $w_f$  is the fracture width [m], k is the reservoir permeability [m<sup>2</sup>], m is the reservoir permeability with consideration of leak-off.

The objective function Eq. (5.5) is the sum of squared errors between the reference and the calculated bottomhole pressure function values.

$$\sum_{i=1}^{n} (y^* - y_i)^2 \to min \tag{5.5}$$

Where  $y^*$  is the reference bottomhole pressure function values (simulate with f = 0.1,  $\mu_0 = 0.1$ , b = 0.1) and  $y_i$  is the calculated bottomhole pressure function values [Pa].

In this parameter optimization simulation, a sensitivity analysis, global- and local optimization will run in sequence in optiSLang-FLAC3D<sup>plus</sup>. According to the above results the uniqueness of the solution will be checked at last. Some of the results are showed in the following figures.

#### 5.3.2 Sensitivity analysis

Sensitivity analysis is the study of how the uncertainty in the output of a model can be

apportioned, qualitatively or quantitatively, to different sources of variation in the input of a model (Saltelli et al. 2008). By means of a global sensitivity analysis and the automatic generation of the Metamodel of Optimal Prognosis (MOP), optimization potential and the corresponding important variables are identified. Figure 5.6a shows the fracture geometry in the simulation of the hydraulic fracture operation at the end of the injection. The fracture height is constrained to circa 100 m due to the large minimum horizontal stress in the cap rock and basement. The fracture half-length is 116 m. Figure 5.6b shows comparison of the evolution of the reference BHP and the simulated one in the sensitivity analysis. Totally 8 design simulations were carried out. We can check the simulation and the reference signal in the statistics post-processing. The reference is covered sufficiently by the simulations. That means, the parameter bounds seem to be adequate for the calibration.

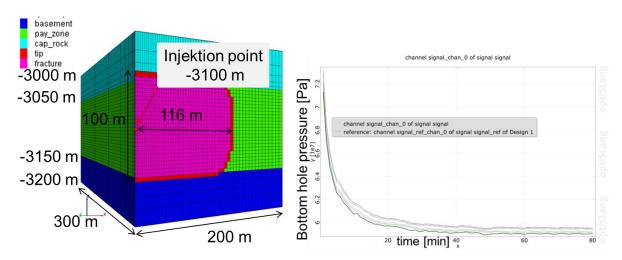


Figure 5.6 (a) Fracture geometry by hydraulic fracturing at the end of the injection; (b) Comparison of the evolution of the reference BHP and the simulated one in the sensitivity analysis

Figure 5.7 shows the 3D plot of single response with respect to the most important variables f and  $\mu_0$ . Error norm can be explained with 99%. Single global optimum is indicated. Parameter b is detected as not important.

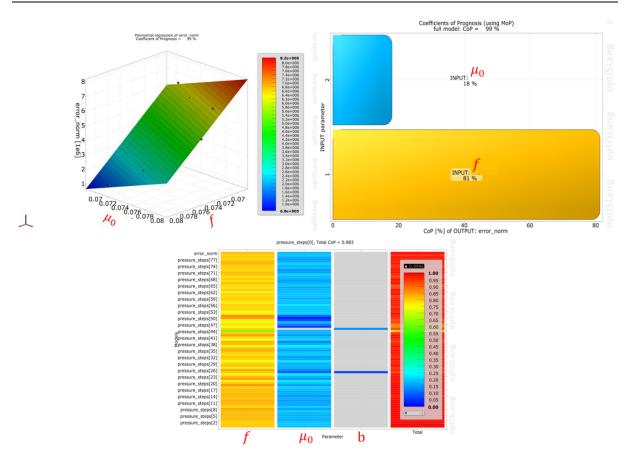


Figure 5.7 3D plot of single response with respect to the most important variables

#### 5.3.3 Global optimization

From the sensitivity analysis we know that, the parameter *b* is not sensitive to any of the pressure values. So, it cannot be identified and is not considered in the optimization. In global optimization, other parameters bounds are kept, only parameter *b* set as constant in the parameter table. Best 4 designs of sensitivity are taken as start design. Here population based optimization method global Evolutionary Algorithm (EA) is used. Totally 12 design simulations were carried out.

The comparison of the evolution of the reference BHP and the simulated one in the global optimization is shown in Figure 5.8a. The Evolutionary Algorithm converges to a small signal difference. The red line means the best design of the global optimization, which is already very close to the reference BHP. Figure 5.8b shows the objective value of the singly simulated optimization design. Obviously, the smallest objective value is 1.48 MPa, which is design 1.

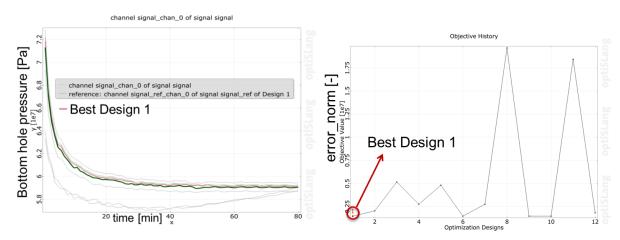


Figure 5.8 (a) Comparison of the evolution of the reference BHP and the simulated one in the global optimization; (b) Objective value of the singly simulated optimization design

## 5.3.4 Local optimization

In local optimization, the parameter *b* is also set as constant in the parameter table. Now the analysis status is pre-optimized. To improve the approximation quality around the optimum, adaptive methods are very efficient. Here a polynomial based local Adaptive Response Surface Method (ARSM) is recommended, which is provided by optiSLang. Then we chose the simplex optimizer. In local optimization, the best design of the EA optimization is imported as start design. The default settings for the Simplex method are kept. Totally 58 design simulations were carried out.

The comparison of the evolution of the reference BHP and the simulated one in the local optimization is shown in Figure 5.9a. The signal of the best design (red line, Design 55) agrees very well with the reference. Figure 5.9b shows the objective value of the singly simulated optimization design. Obviously, the smallest objective value is 0.02 MPa, which is design 55.

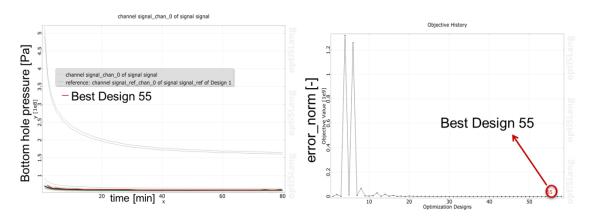


Figure 5.9 (a) Comparison of the evolution of the reference BHP and the simulated one in the global optimization; (b) Objective value of the singly simulated optimization design

The unknown parameters f = 0.11541 and  $\mu_0 = 0.13319$  Pa·s are identified by the optimizer (Figure 5.10). The parameter b is as constant value 0.075.

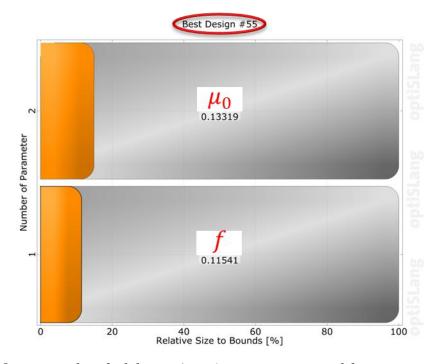


Figure 5.10 Optimizer identified design (input) parameters  $\mu_0$  and f

From the results of the global and the local optimization, the Simplex optimizer eventually coupled with global Evolutionary Algorithm shows good convergence.

# 5.3.5 Check uniqueness of the solution

Figure 5.11 left shows the parallel coordinates plot of the 58 design simulations in local optimization. We reduced the range of the error norm to the best values (Best Design 55, Figure 5.11 right). The remaining signals are very close (Figure 5.9a). The f and  $\mu_0$  show small deviations. So, they can be identified very well with the measurement data.

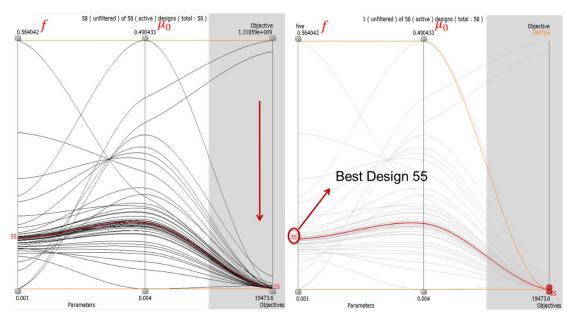


Figure 5.11 Parallel coordinates plot of the 58 design simulations in local optimization

As mentioned above, the parameter for calculation the reference BHP in FLAC3D<sup>plus</sup> is f = 0.1,  $\mu_0 = 0.1$ , b = 0.1. According to the optimization results the best design 55 of optiSLang-FLAC3D<sup>plus</sup> shows the three parameters with f = 0.11541,  $\mu_0 = 0.13319$ , b = 0.075. Since Eq. (5.4) shows that the parameter  $\mu_0$  multiplied to b as the denominator. Thus,  $\mu_0*b = 0.00999$  in optiSLang-FLAC3D<sup>plus</sup>, which is the same as these two parameters multiplied in FLAC3D<sup>plus</sup>  $\mu_0*b = 0.01$ . Therefore, the verification of the developed Frac-Simulator optiSLang-FLAC3D<sup>plus</sup> for history matching of stimulation phase is successful.

#### 5.4 Reservoir simulator TMVOCMP

TMVOCMP (Zhang et al. 2007) is a parallel version of the TMVOC code (Pruess & Battistelli

2002), a numerical simulator for three-phase non-isothermal flow of water, gas, and a multicomponent mixture of volatile organic chemicals (VOCs) in multidimensional heterogeneous porous/fractured media. TMVOCMP retains the physical process model of TMVOC, designed for applications to contamination problems that involve hydrocarbon fuels or organic solvents in saturated and unsaturated zones. TMVOCMP can not only model contaminant behavior under "natural" environmental conditions but also for engineered systems, such as soil vapor extraction, groundwater pumping, or steam assisted source remediation. Therefore, TMVOCMP can handle much complicated and larger problems than TMVOC with a higher computationally efficiency due to its sophisticated parallel computing techniques.

## 5.5 The coupled FracProdu-Simulator optiSLang-FLAC3D<sup>plus</sup>-TMVOCMP

Figure 5.12 shows the coupling concept of the simulator optiSLang-FLAC3D<sup>plus</sup>-TMVOCMP. OptiSLang is used for optimization of parameters. At each time optiSLang modifies the input data and then calls FLAC3D<sup>plus</sup> and TMVOCMP to run it. After the simulation, optiSLang read and judge the output data exported from FLAC3D<sup>plus</sup>. For optimization, several rounds are necessary until the optimization criteria are reached. FLAC3D<sup>plus</sup> is not only used for coupled simulation with TMVOCMP but also for visualization of the simulation results.

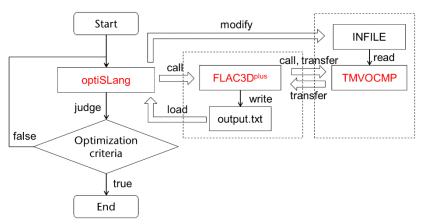


Figure 5.12 Coupling concept of the simulator optiSLang-FLAC3D<sup>plus</sup>-TMVOCMP

The flowchart of the simulator optiSLang-FLAC3D<sup>plus</sup>-TMVOCMP for gas production simulation is described in Figure 5.13. At first the simulated fracture permeability  $k_f$  and fracture width  $w_f$  will be exported in INI\_PERM.txt, which has the similar format as that of INCON data. They will be used to calculate the fracture zone permeability according to Eqs. (5.6), (5.7), (5.8) (Figure 5.14). Then, the reservoir model will be generated in MESH.txt and INCON.txt, which will be copied into the INFILE for TMVOCMP. After that, a reference run (perm\_multiplier = 0.1) will be done in FLAC3D<sup>plus</sup> and TMVOCMP to get a bottomhole pressure, which is treated as reference signal. Then, INFILE, Solver and Output files will be in optiSLang defined. After all the predefinition, a sensitivity analysis, global- and local optimization will run in sequence in optiSLang-FLAC3D<sup>plus</sup>-TMVOCMP. According to the above results the uniqueness of the solution will be checked at last.

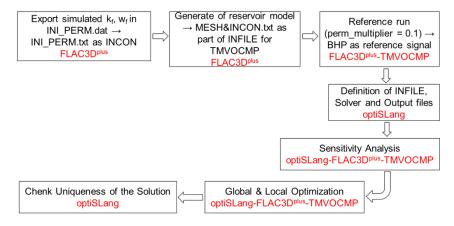


Figure 5.13 Flowchart of the simulator optiSLang-FLAC3D<sup>plus</sup>-TMVOCMP for gas production simulation

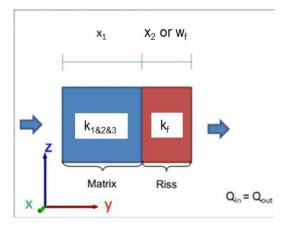


Figure 5.14 Fracture zone Permeability calculation based on superposition

$$k_{y} = \frac{x_{1} + x_{2}}{\frac{x_{1}}{k_{y}^{m}} + \frac{x_{2}}{k_{y}^{f}}} = \frac{x_{1} + w_{f}}{\frac{x_{1}}{k_{2}} + \frac{x_{f}}{k_{y}^{f}}}$$
(5.6)

$$k_{x} = \frac{x_{1} \cdot k_{x}^{f} + x_{2} \cdot k_{x}^{f}}{x_{1} + x_{2}} = \frac{x_{1} \cdot k_{1} + w_{f} \cdot k_{x}^{f}}{x_{1} + w_{f}}$$
(5.7)

$$k_z = \frac{x_1 \cdot k_z^m + x_2 \cdot k_z^f}{x_1 + x_2} = \frac{x_1 \cdot k_3 + w_f \cdot k_z^f}{x_1 + w_f}$$
 (5.8)

where:

 $k_y$ ,  $k_x$ ,  $k_z$ : fracture zone permeability [m<sup>2</sup>]

 $k_x^f$ ,  $k_y^f$ ,  $k_z^f$ : with proppant supported fracture permeability [m<sup>2</sup>]

 $\mathbf{k}_{x}^{m}, k_{y}^{m}, \mathbf{k}_{z}^{m}, k_{1}, k_{2}, k_{3}$ : matrix/reservoir permeability [m<sup>2</sup>]

 $x_1$ : matrix width [m]

 $x_2$ ,  $w_f$ : fracture width [m]

Thus, the coupled FracProdu simulator optiSLang-FLAC3D<sup>plus</sup>-TMVOCMP was developed for history matching of the production phase. An equivalent continuum model is adopted for the coupled simulation. During the production the pore pressure is reduced. The increase in effective normal stress to the supported fractures (closure stress) and the resulting reduction in fracture conductivity are also considered (Figure 5.15). TMVOCMP will calculate the gas production rate and pore pressure change in the reservoir (Figure 5.16). After that the pore pressure is transferred to FLAC3D<sup>plus</sup> for the mechanical simulation, through which the deformation and effective stress of the rock formations are obtained. The change of permeability is calculated in FLAC3D<sup>plus</sup> and then transferred back to TMVOCMP. The updated fracture conductivity as well as the equivalent permeability is then used in the further hydraulic simulation.

# REFERENCE PERMEABILITY DARCIES @ 250°F

Closure Stress [psi]	2lb./ft² 12/18	2lb./ft² 16/30	2lb./ft² 20/40	2lb./ft² 30/60
2000	2742	1207	539	254
4000	2395	939	440	224
6000	1609	721	370	197
8000	894	515	302	167
10000	409	393	246	134
12000	284	298	204	99
14000	194	232	166	73

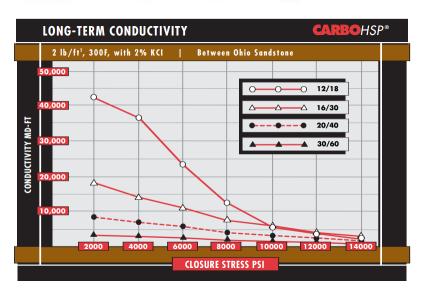


Figure 5.15 The relationship between closure stress and permeability/fracture conductivity based on the different proppant size (CARBO Ceramics, 2006)

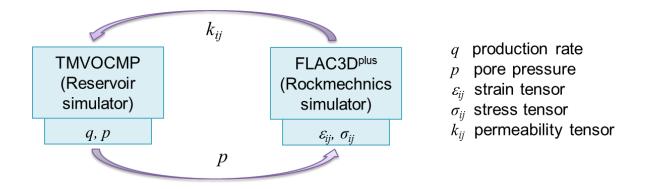


Figure 5.16 Coupled THM effects during production simulation (Gou et al. 2014)

# 5.6 Verification of the developed FracProdu-Simulator

In this section we use the reservoir model of fracturing stage 6 of Leer Z6 (Li et al. 2015) to demonstrate inverse parameters calculation with optiSLang-FLAC3D<sup>plus</sup>-TMVOCMP for gas production simulation. For simplicity, in this verification the increased effective stress induced reduced fracture conductivity is not considered. FLAC3D<sup>plus</sup> is only used for calling TMVOCMP and evaluation/visualization of the simulation results.

For the numerical investigation, a generic 1/2 model is used (Figure 5.17 a). The model lies at a depth between 4,290 and 4,505 m and consists of two major rock formations, namely sand and shale. The whole model has a dimension of 300 m  $\times$  272 m  $\times$  215 m and is discretized into 57,200 rectangle elements. The mesh elements of the fracture zone have a width of 10 m.

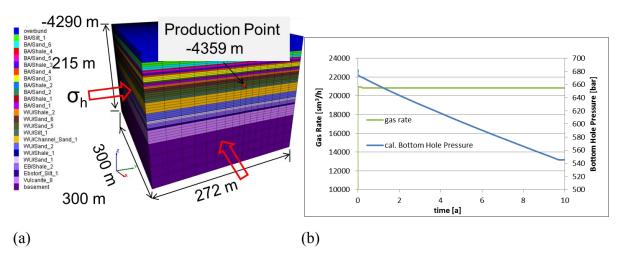


Figure 5.17 (a) Generic 3D 1/2 model for the numerical simulations; (b) Gas production treatment schedule and calculated Bottomhole Pressure

The supposed duration of the whole simulated gas production was 10 years. The gas production took place in the standard state (1 atm, 15 °C) with a supposed constant rate of  $500,000 \text{ sm}^3/\text{d}$  (1/2 model) in the whole 10 years (Figure 5.17 b). The produced gas consists of 94% CH<sub>4</sub>, 6% N<sub>2</sub>. In this simulation, only gas phase would be considered.

The mechanical and hydraulic properties for the rock formations are already listed in Li et al. 2015. With proppant supported fracture permeability and fracture width, which simulated from hydraulic fracturing in FLAC3D<sup>plus</sup>, are exported to INI\_PERM.txt. This text will be read into

TMVOCMP to calculate the fracture zone permeability during gas production simulation.

To achieve optimal adaptation to the reference function the parameter should be defined. Here one parameter (Eq. (5.9)) and its bounds are predefined (start value):

$$a = 0.1, \epsilon [0.01, 1]$$

$$k = a * k_0 \tag{5.9}$$

where:

*a*: permeability multiplier [-]

 $k_0$ : reservoir permeability [m<sup>2</sup>]

k: modified reservoir permeability [m<sup>2</sup>]

The objective function (Eq.(5.10)) is the sum of squared errors between the reference and calculated bottomhole pressure function values.

$$\sum_{i=1}^{n} (y^* - y_i)^2 \to min \tag{5.10}$$

where:

y\*: reference bottomhole pressure function values [Pa]

 $y_i$ : calculated bottomhole pressure function values [Pa]

In this parameter optimization simulation, a sensitivity analysis, global- and local optimization will run in sequence in optiSLang-FLAC3D<sup>plus</sup>-TMVOCMP. According to the above results the uniqueness of the solution will be checked at last. Some of the results are showed in the following figures.

#### 5.6.1 Sensitivity analysis

By means of a global sensitivity analysis and the automatic generation of the Metamodel of Optimal Prognosis (MOP), optimization potential and the corresponding important variables are identified. Figure 5.18 shows comparison of the evolution of the reference BHP and the simulated one in the sensitivity analysis. Totally 60 design simulations were carried out. We can check the simulation and the reference signal in the statistics post-processing. The reference

is covered sufficiently by the simulations. That means, the parameter bounds seem to be adequate for the calibration.

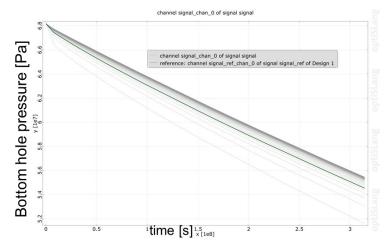


Figure 5.18 (a) Comparison of the evolution of the reference BHP and the simulated one in the sensitivity analysis

Figure 5.19 shows the 3D plot of single response with respect to the most important variable a. Error norm can be explained with 95%. There is only one variable, so parameter a is contributing most to the possible improvement of optimization goal. Single global optimum is indicated.

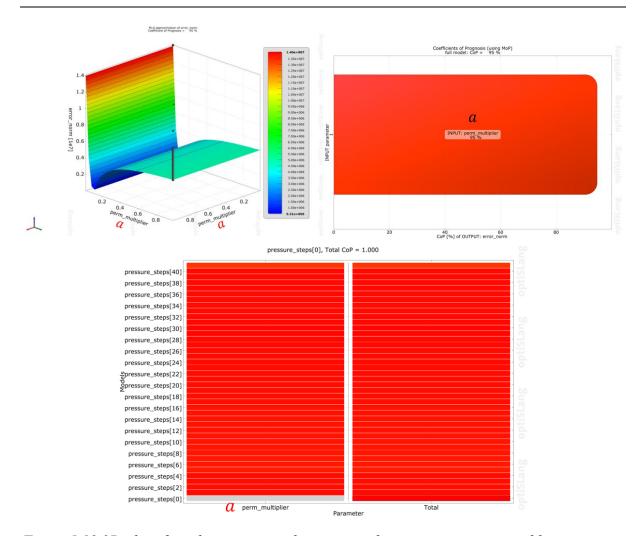


Figure 5.19 3D plot of single response with respect to the most important variables

#### 5.6.2 Global optimization

In global optimization, bounds of parameter *a* are kept. Best 10 designs of sensitivity analysis are taken as start design. Here population based optimization method global Evolutionary Algorithm (EA) is used. Totally 88 design simulations were carried out.

The comparison of the evolution of the reference BHP and the simulated one in the global optimization is shown in Figure 5.20 a. The Evolutionary Algorithm converges to a small signal difference. The red line means the best design of the global optimization, which is already very close to the reference BHP. Figure 5.20 b shows the objective value of the singly simulated optimization design. Obviously, the smallest objective value is 0.3 bar, which is design 10.

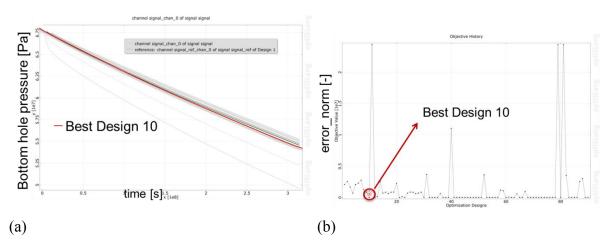


Figure 5.20 (a) Comparison of the evolution of the reference BHP and the simulated one in the global optimization; (b) Objective value of the single simulated optimization design

## 5.6.3 Local optimization

In local optimization, now the analysis status is pre-optimized. To improve the approximation quality around the optimum, adaptive methods are very efficient. Here a polynomial based local Adaptive Response Surface Method (ARSM) is recommended, which is provided by optiSLang. Then we chose the simplex optimizer. In local optimization, best design of the EA optimization is imported as start design. The default settings for the Simplex method are kept. Totally 34 design simulations were carried out.

The comparison of the evolution of the reference BHP and the simulated one in the local optimization is shown in Figure 5.21a. The signal of the best design (red line, Design 31) agrees very well with the reference. Figure 5.21b shows the objective value of the singly simulated optimization design. Obviously, the smallest objective value is 0.07 bar, which is design 31 and smaller than the smallest objective value of global optimization.

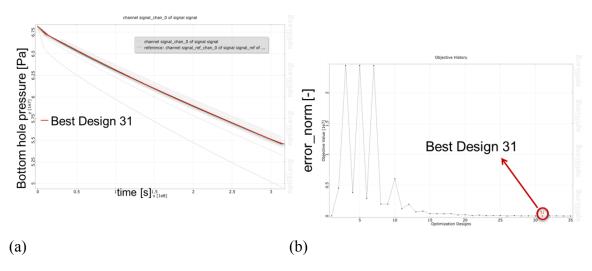


Figure 5.21 (a) Comparison of the evolution of the reference BHP and the simulated one in the global optimization; (b) Objective value of the singly simulated optimization design

The unknown parameters a = 0.10015 are identified by the optimizer (Figure 5.22). From the results of the global and the local optimization, the Simplex optimizer eventually coupled with global Evolutionary Algorithm shows good convergence.

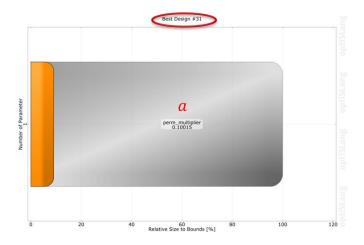


Figure 5.22 Optimizer identified design (input) parameters a

## 5.6.4 Check uniqueness of the solution

Figure 5.23a shows the parallel coordinates plot of the 34 design simulations in local optimization. We reduced the range of the error norm to the best values (Best Design 31, Figure 5.23 b). The remaining signals are very close (Figure 5.23 a). The parameter a shows small

deviation. So, it can be identified very well with the measurement data.

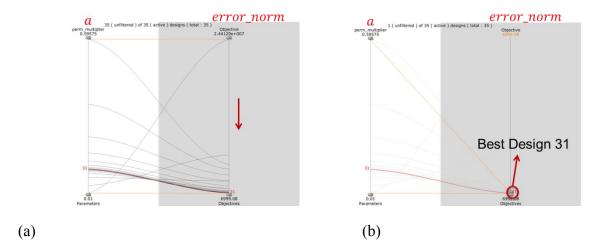


Figure 5.23 Parallel coordinates plot of the 34 design simulations in local optimization

As mentioned above, the parameter for calculation the reference BHP in FLAC3D<sup>plus</sup> is a = 0.1. According to the optimization results the best design 31 of optiSLang-FLAC3D<sup>plus</sup>-TMVOCMP shows the same results with a = 0.10015. Therefore, the verification of the developed FracProdu-Simulator optiSLang-FLAC3D<sup>plus</sup>-TMVOCMP for history matching of production phase is successful.

# 6 Optimization of the hydraulic fracturing operation in the tight gas reservoir Leer

The developed Frac-Simulator optiSLang-FLAC3D<sup>plus</sup> is applied in the simulation of 4 fracturing stages of a horizontal well Z4 in a real tight gas reservoir Leer in the Northern German Basin, which is already introduced in detail in chapter 2.

## 6.1 Numerical simulation of the hydraulic fracturing

In this reservoir, the gas is stored in two types of sandstones: Bahnsen and Wustrow sandstone (Figure 6.1). Based on logging analysis, considering GR-logs, wave propagation velocities in sandstones and shales, as well as porosities, a rock-mechanical relevant sub-division of the Bahnsen- and Wustrow-Member was performed from vertically to slight-slanted drilled reference wells. With the aid of a stratigraphic correlation the Top Wustrow was matched with the fracture locations in the horizontal well and a most likely local rock-mechanical vertical sub-layer-sequence was setup to define rock-mechanical properties.

A 3D geometrical model, which is shown in Figure 6.1, was built with a dimension of 375 m (x) × 1259 m (y) × 292 m (z) and at the depth below -4,308 m. It represents half of the reservoir due to the yz-plane-symmetry. A wellbore had been drilled to the previously calculated target in the Rotliegend rock. The perforations of 4 fracturing stages along the fracturing sequence locate at the depth of -4,421 m, -4,423 m, -4,422 m and -4,406 m in the layer WU-Sst-Sec6, WU-Sst-Sec5, Dirty-WU-Sst & WU-Sst-Sec3and4 and Wustrow-Sand5 & Wustrow-Sand4. All the mechanical and hydraulic parameters for each layer are listed in Table 6.1. The temperature gradient of the reservoir is 2.7 °C/100 m. The temperature of the model top and bottom is 145 °C and 153 °C, respectively. The simulation of hydraulic fracturing was carried out from 1<sup>st</sup> to the 4<sup>th</sup> stage separately. The initial stress and pore pressure distribution of 4 fracturing stages are shown in Figure 6.2.

Table 6.1 Mechanical and hydraulic properties of the rock formations in the calculation model

-					
Rock group	Young's	Poisson	Permeability	Porosity	Density
	modulus	ratio			
	[Pa]	[-]	[m²]	[-]	[kg/m³]
Waste-Zone-Shale	2.93E+10	0.260	1.000E-21	0.050	2550
Ba-Sst-Sec6	3.02E+10	0.193	1.067E-16	0.064	2563
BA-Shale4	2.93E+10	0.159	9.162E-17	0.057	2589
Ba-Sst-Sec5	3.09E+10	0.182	7.577E-17	0.052	2577
BA-Shale3	2.73E+10	0.262	7.597E-	0.059	2579
			17		
Ba-Sst-Sec4	3.26E+10	0.225	5.220E-18	0.022	2631
Ba-Sst-Sec3	3.09E+10	0.197	7.673E-17	0.067	2577
BA-Shale2	2.94E+10	0.248	8.742E-17	0.081	2600
Ba-Sst-Sec2	2.95E+10	0.192	1.516E-16	0.097	2536
BA-Shale1	2.93E+10	0.237	1.053E-16	0.089	2618
Ba-Sst-Sec1	2.54E+10	0.254	3.148E-16	0.113	2536
WU-Shale2	2.96E+10	0.267	4.841E-17	0.069	2633
WU-Sst-Sec6	2.93E+10	0.212	7.233E-15	0.094	2538
WU-Sst-Sec5	2.88E+10	0.198	9.720E-15	0.111	2514
Dirty-WU-Sst	3.05E+10	0.192	5.586E-16	0.076	2567
WU-Sst-Sec3and4	2.89E+10	0.193	1.145E-14	0.113	2501
WU-Sst-Sec2	2.94E+10	0.223	3.265E-15	0.092	2529
WU-Shale1	2.89E+10	0.275	6.607E-17	0.085	2618
WU-Sst-Sec1	2.85E+10	0.253	7.572E-15	0.104	2505
EB-Shale2	3.10E+10	0.221	7.775E-17	0.051	2605

Optimization of Multistage Hydraulic Fracturing Treatment for Maximization of the Tight Gas Productivity

EB-Silt1	3.11E+10	0.224	6.785E-17	0.051	2568
EB-Shale1	3.09E+10	0.220	7.280E-17	0.055	2607
Rotliegend-	3.12E+10	0.220	1.000E-21	0.042	2586
Vulcanite					
Niendf-Damb-Mem	3.60E+10	0.228	1.000E-21	0.001	2750
Dambeck-Shale1	3.00E+10	0.216	9.160E-17	0.032	2574
Bahnsen-Sand5	3.09E+10	0.214	7.580E-17	0.073	2477
Bahnsen-Shale3	3.00E+10	0.212	7.600E-17	0.025	2493
Bahnsen-Sand4	2.98E+10	0.211	5.220E-18	0.089	2474
Bahnsen-Silt1/Sand3	2.81E+10	0.211	7.180E-17	0.110	2431
Bahnsen-Shale2	2.42E+10	0.249	8.740E-17	0.015	2570
Bahnsen-Sand2	2.84E+10	0.211	1.520E-16	0.096	2386
Bahnsen-Shale1	2.86E+10	0.210	1.050E-16	0.072	2506
Bahnsen-Sand1	2.88E+10	0.211	3.150E-16	0.093	2415
Wustrow-	2.80E+10	0.212	5.280E-17	0.093	2465
Shale3/Sand6/Shale2					
Wustrow-Sand5	2.96E+10	0.210	9.720E-15	0.089	2457
Wustrow-Sand4	2.96E+10	0.211	8.030E-15	0.091	2461
Wustrow-Sand3	2.97E+10	0.210	8.030E-15	0.091	2476
Wustrow-Sand2	2.95E+10	0.210	3.270E-15	0.095	2493
Wustrow-Shale1	2.99E+10	0.210	6.610E-17	0.096	2579
Wustrow-Sand1	2.86E+10	0.210	7.570E-15	0.107	2494
Ebstorf-Shale2/Silt2	3.21E+10	0.215	7.280E-17	0.025	2683
Ebstorf-Shale1	3.12E+10	0.213	7.280E-17	0.022	2707
				•	

Ebstorf-Silt1	3.38E+10	0.222	6.790E-17	0.048	2614
Vulcanite	3.66E+10	0.234	1.000E-21	0.034	2704

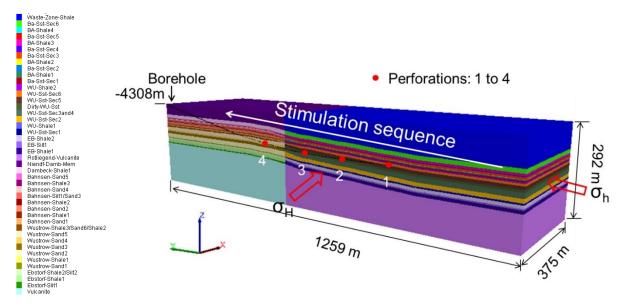


Figure 6.1 1/2 3D model geometry and geological stratigraphy

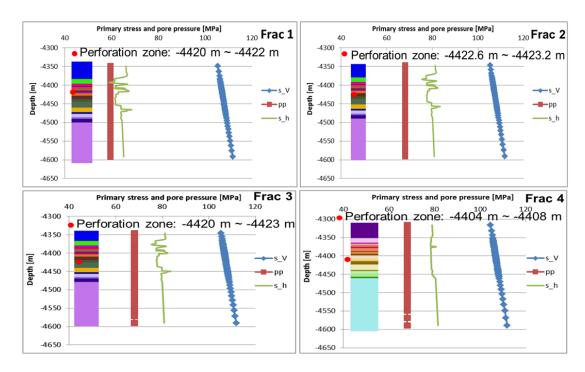


Figure 6.2 Initial stress and pore pressure of 4 fracturing stages

During the fracture treatments, a total of 1500 m<sup>3</sup> fracturing fluid with 399 tons of proppants

(type: CARBOHSP 20/40 mesh) have been injected into the reservoir formation through 4 stages (Frac-stage 1: 300 m<sup>3</sup> with 76 tons; Frac-stage 2: 350 m<sup>3</sup> with 83 tons; Frac-stage 3: 400 m<sup>3</sup> with 111 tons; Frac-stage 4: 450 m<sup>3</sup> with 129 tons). The surface treating pressure were measured during the fracture treatment. They were converted to the bottomhole pressure (BHP) and used for the history matching.

#### 6.1.1 Simulation results of frac-stage 1

During the main fracturing, the injection rate increased to 4 m³/min. Figure 6.3 shows the comparison of the calculated BHP from the measured treating pressure and the simulated one during the main fracturing. Except the unstable section at the end of the injection, which is caused by pre-mature screen out, the simulated pressure matches well with the calculated one, which proves the reliability of the modeled fracture propagation and closure.

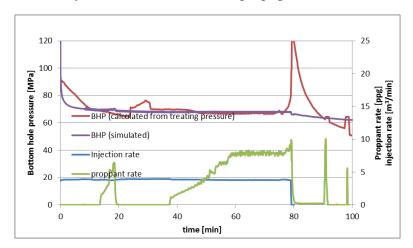


Figure 6.3 Comparison of the calculated BHP from the measured treating pressure and the simulated during the main fracturing 1

Figure 6.4 shows the fracture pattern with width distribution and proppant mass distribution per unit area at shut-in and closure. At the end of the injection (t = 80 min), the fracture got a half-length of 126 meters and a height of 86 meters (Figure 6.5a). In the meantime, the proppant was distributed with a decreased concentration (mass per unit area) along the radius from the injection, which represents the increased injection rate of the proppant. The proppant front is Optimization of Multistage Hydraulic Fracturing Treatment for Maximization of the Tight Gas Productivity

below the injection level because of the settling effect. At t = 1000 minutes (920 min after shutin) there is no proppant anymore at the middle part of the fracture, where the perforation is located. This may be the main reason for a poor hydraulic connection and thus for a lower contribution to performance. The reason for the geometry of fracture 1 is the significant change in horizontal stress along the depth caused by partial pressure reduction due to dynamic connection to the adjacent wellbore. Figure 6.5b shows the temporary development of the widths and the concentration distribution at perforation. Indeed, at t = 200 minutes the proppant concentration at perforation has already reduced to 0%, which is the main reason for the insufficient hydraulic connection, which means no contribution to production.

One indicator of a successful frac-stage is a large fracture conductivity value. Fracture conductivity is the width of the generated fracture  $(w_f)$  multiplied by the permeability of the propped region  $(k_f)$ . The propped fracture has a much higher permeability than the surrounding formation and acts as a high permeability channel for fluids to flow through, which improves production for the well. Comparison of the effect of fracture conductivity on production can be made easily if conductivity is cast in dimensionless terms  $(F_{CD})$ . The dimensionless fracture conductivity, the fracture conductivity in respect to the conductivity capacity of the reservoir defined as  $F_{CD} = k_f w_f / k x_f$  (Prats, 1961). For frac-stage 1 the dimensionless fracture conductivity  $(F_{CD})$  is 12.3.

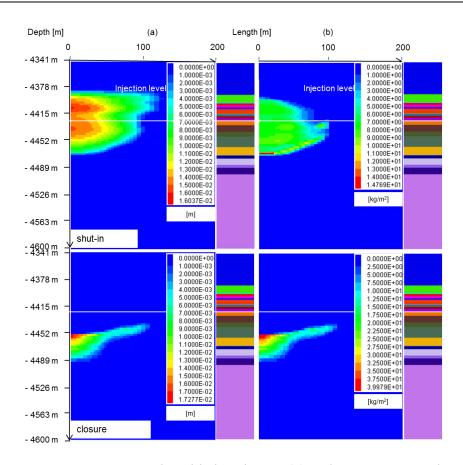


Figure 6.4 Fracture pattern with width distribution (a) and proppant mass distribution pro area (b) at shut-in (t = 80 min) and closure (t = 1000 min) during the main fracturing 1

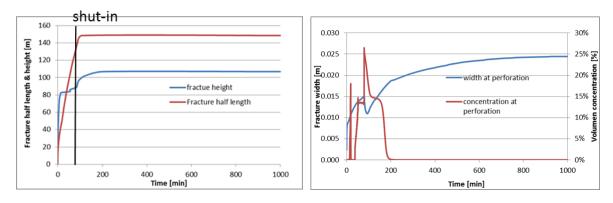


Figure 6.5 (a) Temporal developments of the fracture half-length and height during the main fracturing 1; (b) Temporal developments of the fracture and the proppant concentration at perforation during the main fracturing 1

Figure 6.6 shows the comparison between simulator FLAC3D<sup>plus</sup> and FracPro by the fracture half-length, height and average fracture width at shut-in and closure. The simulation results of Optimization of Multistage Hydraulic Fracturing Treatment for Maximization of the Tight Gas Productivity

FracPro come from Koehler (2005). Since FracPro is a commercial simulator, it cannot simulate the fracture closure process properly. Thus, the simulation results between them are comparable, especially at shut-in.

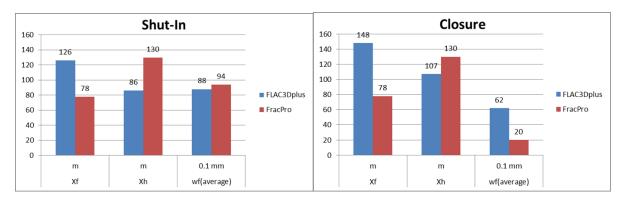


Figure 6.6 Comparison between FLAC3D<sup>plus</sup> and FracPro by the fracture geometry at shut-in and closure during the main fracturing 1

Figure 6.7 shows the comparison of the fracture volume and the injection volume. After t = 1000 minutes the fracture volume stays constant, which means that the fully closure is reached. Figure 6.8 shows the comparison between FLAC3D<sup>plus</sup> and FracPro by the injection volume, fracture volume and leak-off at shut-in and closure. The differences between them are small, especially at shut-in.

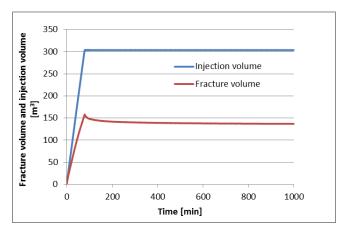


Figure 6.7 Comparison of the fracture volume and the injection volume in the main fracturing during the main fracturing 1

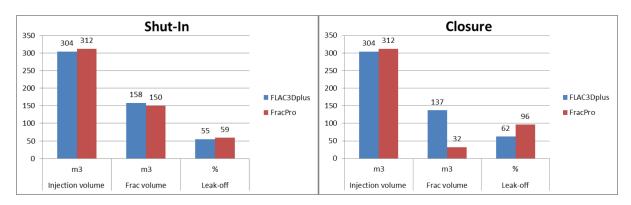


Figure 6.8 Comparison between FLAC3D<sup>plus</sup> and FracPro by the injection volume, fracture volume and leak-off at shut-in and closure during the main fracturing 1

The viscosity distribution and the formation temperature are shown in Figure 6.9. The largest fluid viscosity value is 0.87 Pa·s at shut-in. And the temperature around the perforation is 50 °C, which is coinciding with the injection temperature. Because of the gel breaking during the hydraulic fracturing, the fluid viscosity reduced gradually after shut-in. And because of the energy transport the formation temperature gradually comes back to the initial reservoir temperature.

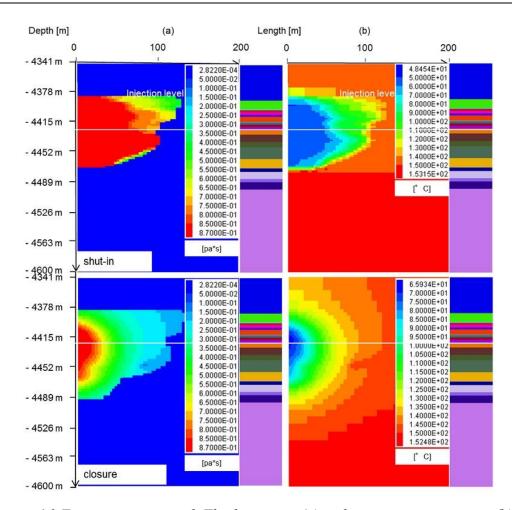


Figure 6.9 Fracture pattern with Fluid viscosity (a) and reservoir temperature (b) at shut-in (t = 80 min) and closure (t = 1000 min) during the main fracturing 1

## 6.1.2 Simulation results of frac-stage 2

Figure 6.10 shows the comparison of the calculated BHP from the measured treating pressure and the simulated one during the main fracturing. The simulated pressure matches well with the calculated one, which proves the reliability of the modeled fracture propagation and closure.

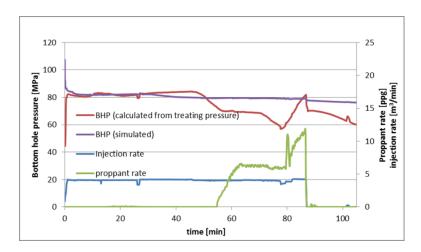


Figure 6.10 Comparison of the calculated BHP from the measured treating pressure and the simulated during the main fracturing 2

Figure 6.11 shows the fracture pattern with width distribution and proppant mass distribution per unit area at shut-in and closure. At the end of the injection (t = 87 min), the fracture got a half-length of 84 meters and a height of 63 meters (Figure 6.13 a). It is noteworthy in Figure 6.11 b, that there is a maximum value appearing along the fracture length at the depth of -4439 m by the proppant mass per unit area at shut-in. The proppant mass per unit area (Eq. (6.1)) is defined as,

$$\frac{Mp}{A} = w_f * C_p * \rho_p \tag{6.1}$$

where  $M_p$  is proppant mass [kg], A is fracture area [m<sup>2</sup>],  $w_f$  is fracture width [m],  $C_p$  is proppant volume concentration [%],  $\rho_p$  is proppant density [kg/m<sup>3</sup>].

For fracture 2 the dimensionless fracture conductivity ( $F_{CD}$ ) is 12.2. Figure 6.12 shows fracture width, proppant volume concentration and proppant mass per unit area along the fracture length at shut-in. The fracture width reduced along the facture length. The proppant volume concentration hat reached the maximum value of 65% from x = 74 m. According to the (Eq. (6.1)), the proppant mass per unit area is equal to the product of the facture width and proppant volume concentration. So, at x = 74 m the proppant mass per unit area has reached the maximum value of 15.6 kg/m<sup>2</sup>. That is the reason for the maximum value appearance along the fracture length by the proppant mass per unit area at shut-in.

At t = 650 minutes (563 min after shut-in), the width shows the same contour distribution as the proppant, which indicates that the fracture got already in contact with the proppant and no more closure would happen there.

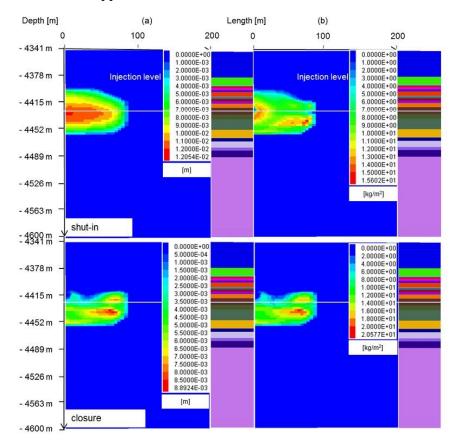


Figure 6.11 Fracture pattern with width distribution (a) and proppant mass distribution pro area (b) at shut-in (t = 87 min) and closure (t = 650 min) during the main fracturing 2

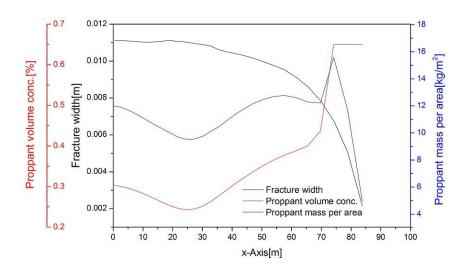


Figure 6.12 Fracture width, proppant volume concentration and proppant mass per unit area along the fracture length at shut-in (z = -4439 m) during the main fracturing 2

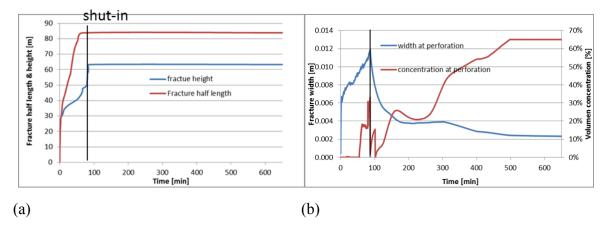


Figure 6.13 (a) Temporal developments of the fracture half-length and height during the main fracturing; (b) Temporal developments of the fracture and the proppant concentration at perforation during the main fracturing 2

Figure 6.14 shows the comparison between FLAC3D<sup>plus</sup> and FracPro by the fracture half-length, height and average fracture width at shut-in and closure. The differences between them are small and acceptable i.e. can be neglected.

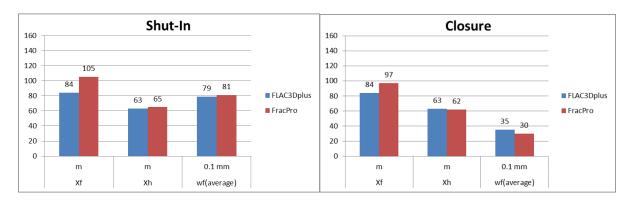


Figure 6.14 Comparison between FLAC3D<sup>plus</sup> and FracPro by the fracture geometry at shutin and closure during the main fracturing 2

Figure 6.15 shows the comparison of the fracture volume and the injection volume. After t = 650 minutes the fracture volume stays constant, which means that the fully closure is reached. Figure 6.16 shows the comparison between FLAC3D<sup>plus</sup> and FracPro by the injection volume, fracture volume and leak-off at shut-in and closure. The differences between them are small.

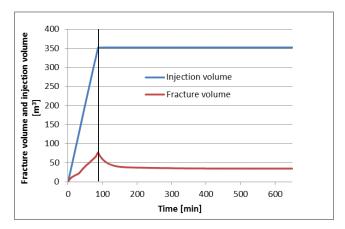


Figure 6.15 Comparison of the fracture volume and the injection volume during the main fracturing 2

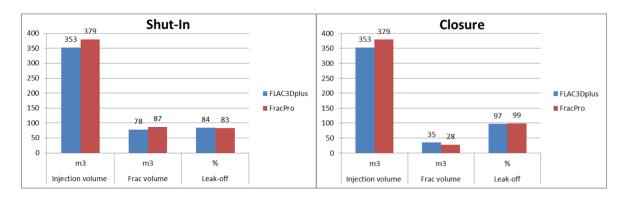


Figure 6.16 Comparison between FLAC3D<sup>plus</sup> and FracPro by the injection volume, fracture volume and leak-off at shut-in and closure during the main fracturing 2

The viscosity distribution and the formation temperature are shown in Figure 6.17. The largest fluid viscosity value is 0.87 Pa·s at shut-in. And the temperature around the perforation is 50 °C, which is coinciding with the injection temperature. Because of the gel breaking during the hydraulic fracturing, the largest fluid viscosity reduced to 0.65 Pa·s at closure. And because of the energy transport the formation temperature gradually comes back to the initial reservoir temperature.

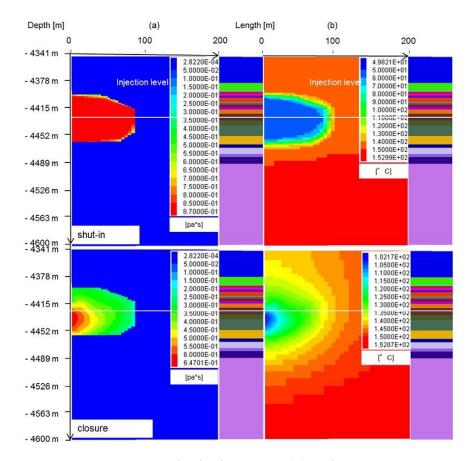


Figure 6.17 Fracture pattern with Fluid viscosity (a) and reservoir temperature (b) at shut-in (t = 87 min) and closure (t = 650 min) during the main fracturing 2

### **6.1.3** Simulation results of frac-stage 3

Figure 6.18 shows the comparison of the calculated BHP from the measured treating pressure and the simulated one during the main fracturing. The simulated pressure matches well with the calculated one, which proves the reliability of the modeled fracture propagation and against closure.

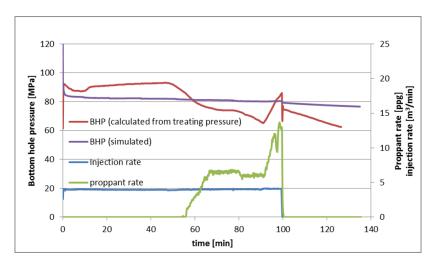


Figure 6.18 Comparison of the calculated BHP from the measured treating pressure and the simulated during the main fracturing 3

Figure 6.19 shows the fracture pattern with width distribution and proppant mass distribution per unit area at shut-in and closure. At the end of the injection (t = 100 min), the fracture got a half-length of 94 meters and a height of 76 meters (Figure 6.21 a). At t = 1000 minutes (900 min after shut-in), the width shows the same contour distribution as the proppant, which indicates that the fracture got already in contact with the proppant and no more closure would happen there. Figure 6.21 b shows the temporary development of the widths and the concentration distribution at perforation. From t = 223 min the proppant concentration at perforation has already reached 65%. For frac-stage 3 the dimensionless fracture conductivity ( $F_{CD}$ ) is 19.2.

Figure 6.20 shows fracture width, proppant volume concentration and proppant mass per unit area along the fracture length at shut-in and at the depth of -4432 m. The fracture width reduced along the facture length. The proppant volume concentration hat reached the maximum value of 65% from x = 79 m. According to the Eq. (6.1), the proppant mass per unit area is equal to the product of the facture width and proppant volume concentration. So, at x = 74 m the proppant mass per unit area has reached the maximum value of 16.4 kg/m<sup>2</sup>. That is the reason for the maximum value appearance along the fracture length by the proppant mass per unit area at shut-in (Figure 6.19 b).

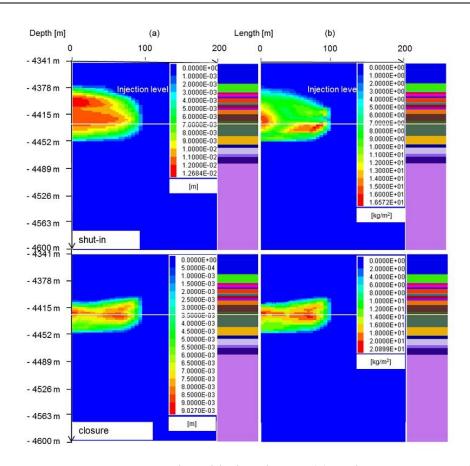


Figure 6.19 Fracture pattern with width distribution (a) and proppant mass distribution pro area (b) at shut-in (t = 100 min) and closure (t = 1000 min) during the main fracturing 3

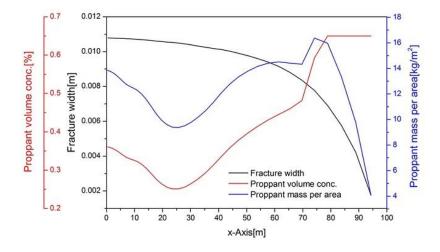


Figure 6.20 Fracture width, proppant volume concentration and proppant mass per unit area along the fracture length at shut-in (Z = -4432m) during the main fracturing 3

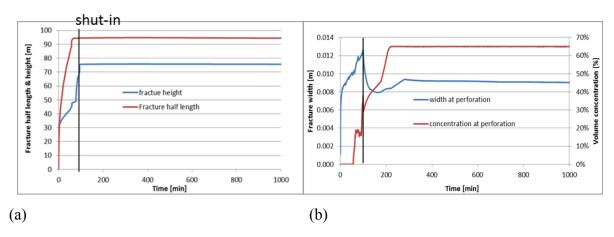


Figure 6.21 (a) Temporal developments of the fracture half-length and height during the main fracturing; (b) Temporal developments of the fracture and the proppant concentration at perforation during the main fracturing 3

Figure 6.22 shows the comparison between FLAC3D<sup>plus</sup> and FracPro by the fracture half-length, height and average fracture width at shut-in and closure. The differences between them are small and can be neglected.

Figure 6.23 shows the comparison of the fracture volume and the injection volume. After t = 1000 minutes the fracture volume stays constant, which means that the fully closure is reached. Figure 6.24 shows the comparison between FLAC3D<sup>plus</sup> and FracPro by the injection volume, fracture volume and leak-off at shut-in and closure. The difference between them is very small.

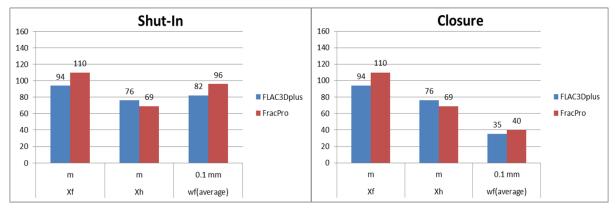


Figure 6.22 Comparison between FLAC3Dplus and FracPro by the fracture geometry at shutin and closure during the main fracturing 3

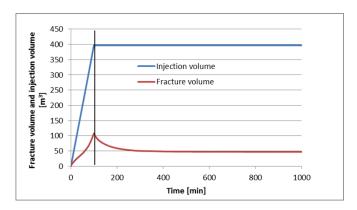


Figure 6.23 Comparison of the fracture volume and the injection volume in the main fracturing during the main fracturing 3

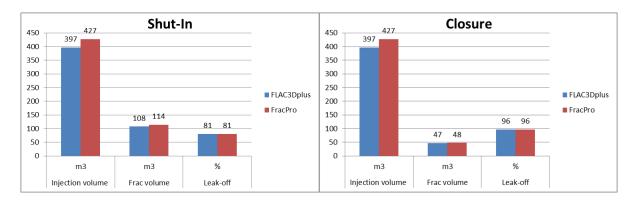


Figure 6.24 Comparison between FLAC3D<sup>plus</sup> and FracPro by the injection volume, fracture volume and leak-off at shut-in and closure during the main fracturing 3

The viscosity distribution and the formation temperature are shown in Figure 6.25. The largest fluid viscosity value is 0.87 Pa·s at shut-in. And the temperature around the perforation is 50 °C, which is coinciding with the injection temperature. Because of the gel breaking during the hydraulic fracturing, the largest fluid viscosity reduced to 0.64 Pa·s at closure. And because of the energy transport the formation temperature gradually comes back to the initial reservoir temperature.

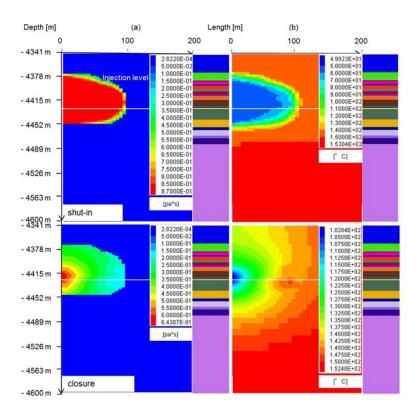


Figure 6.25 Fracture pattern with Fluid viscosity (a) and reservoir temperature (b) at shut-in (t = 100 min) and closure (t = 1000 min) during the main fracturing 3

### 6.1.4 Simulation results of frac-stage 4

Figure 6.26 shows the comparison of the calculated BHP from the measured treating pressure and the simulated one during the main fracturing. Except the unstable section at the end of the injection, which is caused by pre-mature screen out, the simulated pressure matches well with the calculated one, which proves the reliability of the modeled fracture propagation and closure.

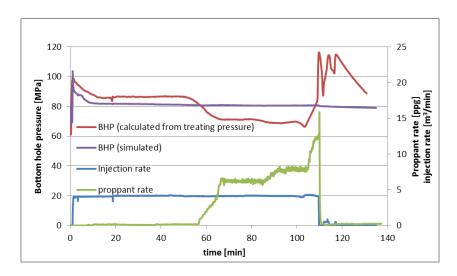


Figure 6.26 Comparison of the calculated BHP from the measured treating pressure and the simulated during the main fracturing 4

Figure 6.27 shows the fracture pattern with width distribution and proppant mass distribution per unit area at shut-in and closure. At the end of the injection (t = 110 min), the fracture got a half-length of 100 meters and a height of 86 meters (Figure 6.28 a). The reason of the maximum value appearance along the fracture length by proppant mass per unit area at shut-in is the same with fracture 2 and 3 (Figure 6.27 b). At t = 740 minutes (630 min after shut-in), the width shows the same contour distribution as the proppant, which indicates that the fracture got already in contact with the proppant and no more closure would happen there. Figure 6.28 b shows the temporary development of the widths and the concentration distribution at perforation. From t = 200 min the proppant concentration at perforation has already reached 65%. For frac-stage 4 the dimensionless fracture conductivity ( $F_{CD}$ ) is 22.6.

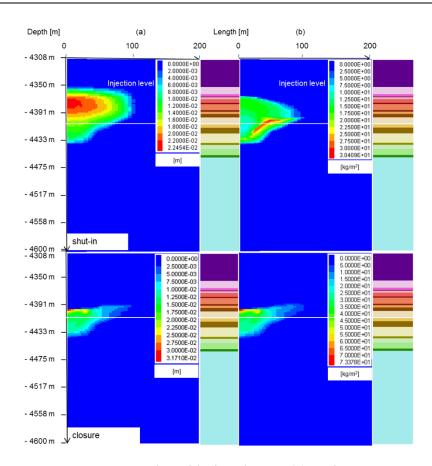


Figure 6.27 Fracture pattern with width distribution (a) and proppant mass distribution pro area (b) at shut-in (t = 110 min) and closure (t = 740 min) during the main fracturing 4

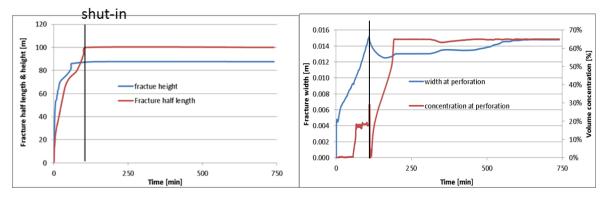


Figure 6.28 (a) Temporal developments of the fracture half-length and height during the main fracturing; (b) Temporal developments of the fracture and the proppant concentration at perforation during the main fracturing 4

Figure 6.29 shows the comparison between FLAC3D<sup>plus</sup> and FracPro by the fracture half-length, height and average fracture width at shut-in and closure. The differences between them are Optimization of Multistage Hydraulic Fracturing Treatment for Maximization of the Tight Gas Productivity

small and can be neglected.

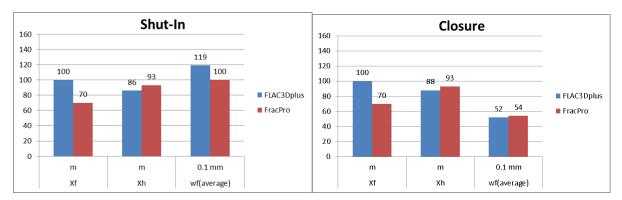


Figure 6.29 Comparison between FLAC3Dplus and FracPro by the fracture geometry at shutin and closure during the main fracturing 4

Figure 6.30 shows the comparison of the fracture volume and the injection volume. After t = 740 minutes the fracture volume stays constant, which means that the fully closure is reached. Figure 6.31 shows the comparison between FLAC3D<sup>plus</sup> and FracPro by the injection volume, fracture volume and leak-off at shut-in and closure. The difference between them is very small.

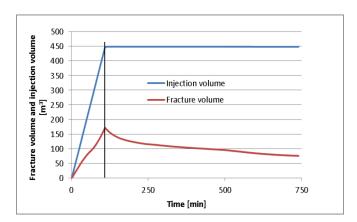


Figure 6.30 Comparison of the fracture volume and the injection volume during the main fracturing 4

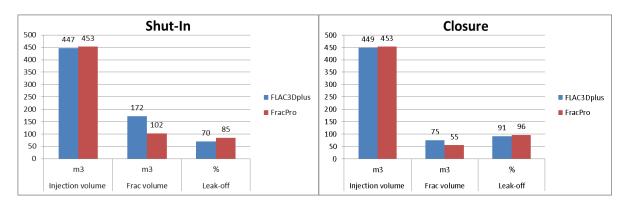


Figure 6.31 Comparison between FLAC3D<sup>plus</sup> and FracPro by the injection volume, fracture volume and leak-off at shut-in and closure during the main fracturing 4

The viscosity distribution and the formation temperature are shown in Figure 6.32. The largest fluid viscosity value is 0.87 Pa·s at shut-in. And the temperature around the perforation is 50 °C, which is coinciding with the injection temperature. And because of the energy transport the formation temperature gradually comes back to the initial reservoir temperature.

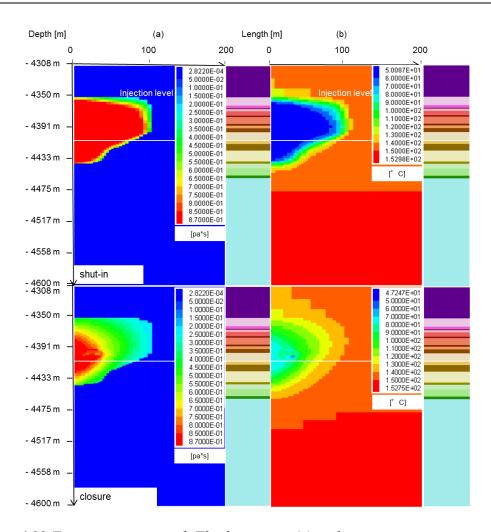


Figure 6.32 Fracture pattern with Fluid viscosity (a) and reservoir temperature (b) at shut-in (t = 110 min) and closure (t = 740 min)

### 6.1.5 Summary

The simulation results are shown in Figure 6.33 and Figure 6.34. Figure 6.33 shows the comparison of the simulated BHP and the BHP derived from the measured treating pressure for all the four fractures. Generally, the simulated fracturing results match with the treating pressure measurement. It is noteworthy that a rapid rise in measured pressure shortly before the shut-in of the stage 1 and 4 occurred. This phenomenon occurs when the proppant in the fracture fluid forms a bridge across the perforations. This leads to a sudden and significant restriction of fluid flow and is called pre-mature screen-out. However, such changes of surface treating pressure will not affect the fracture propagation.

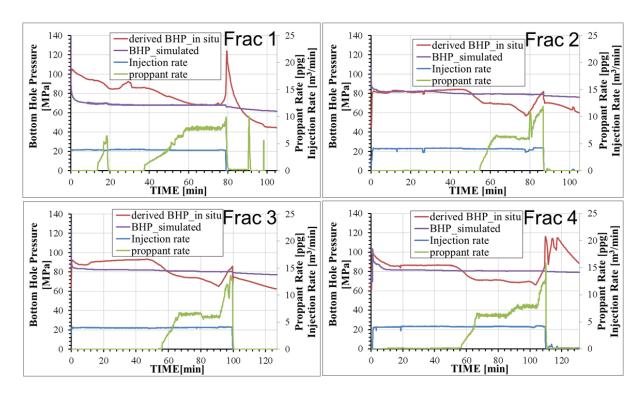


Figure 6.33 Comparison of the simulated BHP and the BHP derived from the measured treating pressure

The dimensionless fracture conductivity  $F_{CD}$  (Eq. (3.40)) is derived from the simulated fracture geometry and shown in Figure 6.34. The  $F_{CD}$  becomes larger and larger from the  $2^{st}$  to the  $4^{th}$  fracturing stage, which reveals the performance becomes better and better. It is noteworthy that, although the  $F_{CD}$  of the fracture 1 is a little bit larger than that of the fracture 2, there is already no proppant at the perforation of fracture 1. This should be the main reason for the insufficient hydraulic connection of the fracture 1 and thus a low contribution to the total gas production.

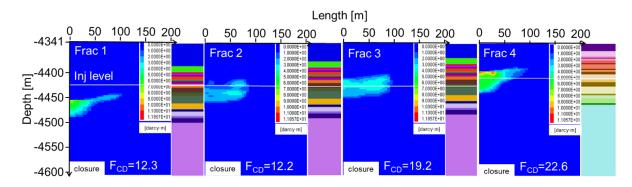


Figure 6.34 The dimensionless fracture conductivity of the main fractures 1 to 4 at closure

The reason for the fracture geometry of frac-stage 1 is the significant changing in the vertical stress-log, which was caused by partial reservoir pressure reductions due to dynamic connections to the side-tracked well Leer Z3a (Koehler & Kerekes 2006). This heterogeneity in the vertical reservoir pressure profile had a severe impact on the vertical stress profile and thus to the fracture geometry in lateral and vertical propagation sense.

## 6.2 Numerical simulation of the gas production

To maximize the productivity of the tight gas wellbore, the performance of the reservoir with artificial fractures should be studied. This requires the gas production simulation, and the matching of the in-situ measured production rate is necessary. Especially for the stimulated reservoir, the pore pressure reduction will increase the effective normal stress on the propped fractures and lead to the reduction of fracture conductivity. So, the coupled thermo-hydromechanical effects must be considered.

To carry out the coupled thermo-hydraulic-mechanical simulation with optiSLang-FLAC3D<sup>plus</sup>-TMVOCMP (Figure 6.35), a same 3D reservoir model includes in the stimulation phase created four fractures with their own fracture widths and proppant distributions (described in section 6.1) is generated. As shown in Figure 2.5, a huge fault lies southwest of the fracture 4, which doesn't allow any inflow or outflow during the gas production. Therefore, the left (southwest) boundary of the model is closed, meanwhile the other three lateral boundaries are open. The first production period lasted from Jul. 2006 to Dec. 2009 for 3.5 years. The well is producing gas at a rate of about 19,000 m³(Vn)/h during the first half year. The bottomhole pressure (BHP) derived from measured well head pressure (Figure 6.36) was used as input for the stress sensitive reservoir simulation.

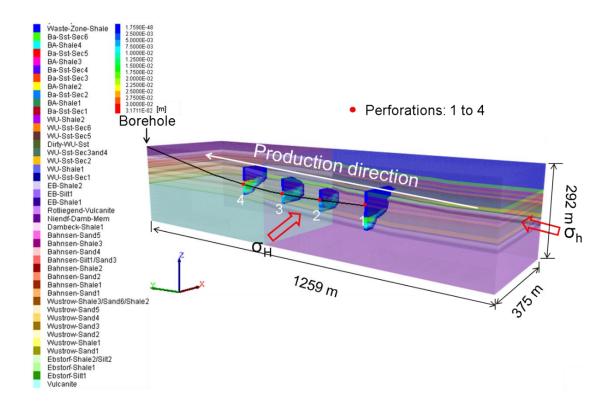


Figure 6.35 ½ 3D model geometry and geological stratigraphy including four created fractures

The simulated temporal evolution of gas production rate, bottomhole and reservoir pressure are shown in Figure 6.36. The total produced gas volume is 276 Mio. sm<sup>3</sup>. Frac-stage 1 to frac-stage 4 produce  $5.18 \times 10^5$  sm<sup>3</sup>,  $1.02 \times 10^8$  sm<sup>3</sup>,  $8.82 \times 10^7$  sm<sup>3</sup> and  $8.48 \times 10^7$  sm<sup>3</sup>, respectively (Figure 6.37). The simulated gas production rate has the similar tendency to that of the in-situ measured data. Only there is a sudden increase in the in-situ gas rate in a short period from May 2007, since a sand cleanout was done at that time. However, the sand cleanout induced productivity index increase cannot be considered through numerical simulation, so there is a little bit mismatches.

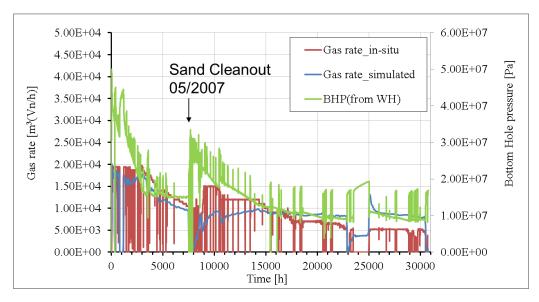


Figure 6.36 Comparison of the simulated gas rate and in-situ measured gas rate

The contribution of each fracture to the total gas production rate are listed in Figure 6.37. It can be seen that the gas rate of fracture 1 is very low. This confirms the earlier prediction that there is no proppant at the perforation and the perforation has a poor hydraulic connection to the supported fracture (Figure 6.34). The pore pressure distribution in the reservoir near the fractures are shown in Figure 6.38. Compared to other 3 fractures, the pore pressure around fracture 1 is reduced least. That means, the least amount of gas is produced by fracture 1.

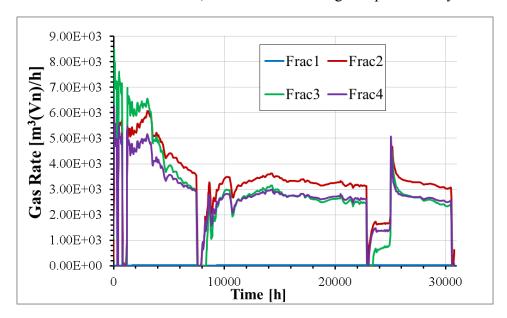


Figure 6.37 Comparison of the contribution of each fracture to the total production rate

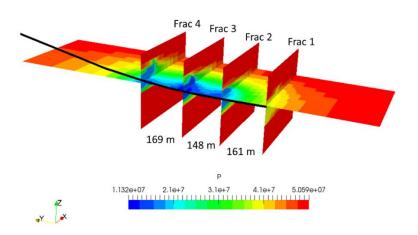


Figure 6.38 Pore pressure distribution in the reservoir near the fractures at t = 3.5 a

## 6.3 Proposal of a new calculation formula of F<sub>CD</sub>

The Leer Z4 order of the dimensionless fracture conductivity  $F_{CD}$  according to Prats ((3.40)) is 2 < 1 < 3 < 4. However, the order of the simulated gas rate at the beginning of the production is 1 < 2 < 4 < 3 (Figure 6.39). The two orders are inconsistent. The reason for this is that the calculation of  $F_{CD}$  according to Prats does not consider the proppant distribution and concentration, in particular the distance from the supported fracture to the perforation. As we all know, the closer the propped area to the perforation and the more concentrated the proppant, the better hydraulic connection can be achieved. Therefore, the position and concentration of the proppant play important roles for the later production. For this reason, a new modified weighted calculation formula of  $F_{CD}$  (Eq. (6.2)) was proposed, which takes the proppant position and concentration into account.

$$F_{CD} = \frac{\sum_{i=1}^{n} \frac{w_i k_{f_i}}{d_i} A_i \frac{C_p}{C_{max}}}{\sum_{i=1}^{n} \frac{1}{d_i} A_i \frac{C_p}{C_{max}}} \times \frac{1}{k x_f}$$
(6.2)

where,

 $C_{max}$ : maximum proppant concentration (=0.65) [-]

w: fracture width [m]

 $k_f$ : fracture permeability [m<sup>2</sup>]

d: distance between fracture element and perforation [m]

A: fracture element area [m<sup>2</sup>]

 $C_p$ : proppant concentration [-]

k: reservoir permeability [m<sup>2</sup>]

 $x_f$ : fracture half-length [m]

*n*: total fracture element [-]

With the hydraulic fracturing simulation and modified weighted  $F_{CD}$  man can better predict the gas rate. Now the order of gas rate at the beginning of the production is the same as the prediction by modified weighted  $F_{CD}$  (Table 6.2).

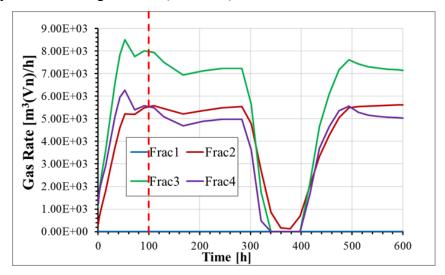


Figure 6.39 Comparison of the contribution of each fracture to the total production rate at the beginning

Table 6.2 Comparison of  $F_{CD}$  and initially gas rate

F <sub>CD</sub> , prats	2<1<3<4
F <sub>CD</sub> , weighted	1<2<4<3
gas rate, begin	1<2<4<3

Besides  $F_{CD}$ , the pressure difference between the wellbore and reservoir is also a decisive factor for the gas rate. In addition, the fracture will affect with each other during the production. At the same time, the large fault (Figure 2.5) reduces the producible gas volume in the vicinity. Hence, the final relationship (Table 6.3) of produced gas volumes is different than that at the beginning (as well as the  $F_{CD}$ ).

*Table 6.3 Contribution of each farcture for the total produced gas volume* 

	F <sub>CD, prats</sub>	F <sub>CD, prats</sub> F <sub>CD, weighted</sub>	
			[Mio. sm <sup>3</sup> ]
Frac-stage 1	12.3	2.6	0.5
Frac-stage 2	12.2	11.1	102
Frac-stage 3	19.2	17.6	88
Frac-stage 4	22.6	15.7	85
Order	2<1<3<4	1 < 2 < 4 < 3	1 < 4 < 3 < 2

# 6.4 Sensitivity analysis

In this section a sensitivity analysis of the 3<sup>rd</sup> fracturing stage Leer Z4 (described in chapter 5.4) were carried out with different design parameters to obtain their sensitivities, including proppant type, viscosity of the injection fluid and injection time/rate.

#### **6.4.1** Proppant type

During the fracture treatment in the field, the applied proppant was CARBOHSP 20/40 (Basic case: 3,560 kg/m3, 667 microns). For the variation studies, two different types of proppants have been applied. They are CARBOECONOPROP 40/70 (Var. 1: 2,700 kg/m³, 334 microns) and CARBO-Lite 16/20 (Var. 2: 2,700 kg/m³, 1075 microns).

The simulation results are shown in Figure 6.40 and Figure 6.41. In this paper, all the fracture half-length and height mean the largest value during the stimulation, although the upper part of the fracture will closure again after shut-in due to the proppant settling effect. There is no significantly fracture height difference between basic and variations because of the constriction of the fracture barrier (Figure 6.40). The main differences between them lie in average fracture width and fracture volume due to the enlarged propped area of variations. The proppant distribution of variations is better than that of the basic case due to their lower densities (Figure 6.41). The fracture half-length of variation 1 (CARBOECONOPROP 40/70) is slightly larger than that of variation 2 (CARBO-Lite 16/20). Even so, variation 2 (CARBO-Lite 16/20) still shows the best performances (with the largest modified weighted F<sub>CD</sub>) due to the lowest density and largest proppant diameter, which can lead to an abated settling effect and a larger supported fracture width to ensure high fracture conductivity at high strength.

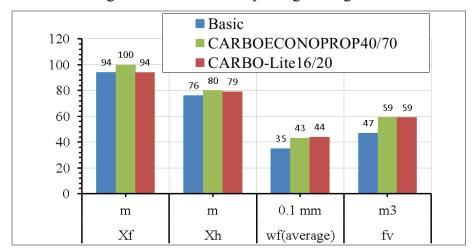


Figure 6.40 Comparison of the fracture geometry and volume at closure with three different types of proppants

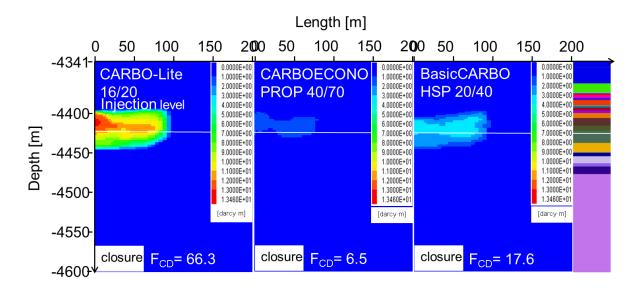


Figure 6.41 Comparison of the fracture conductivity contour and derived dimensionless fracture conductivity (modified) at closure with three different types of proppants

### 6.4.2 Viscosity of the injection fluid

During the simulation, the viscosity of the injection fluid is dependent on both temperature and time. It will change from 870 cp (80°C, t = 0.1 h) to 4.2 cp (160°C, t = 10 h). These data are used for the basic case. For the variation study the applied two varied viscosities (+50% and -50%) of the injection fluid are shown in Figure 6.42.

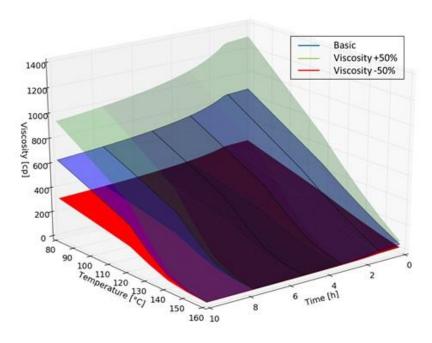


Figure 6.42 Varied viscosity of the injection fluid +50% (Var. 3); -50% (Var. 4)

The fracture geometry is compared in Figure 6.43. The fracture half-length of the variation 3 is lower than that of the basic case due to the higher viscosity with insufficient fluidity. That is also the reason for the higher height of variation 3. The changes of the injection fluid viscosity have almost no influences on the average fracture width and fracture volume during closure. The simulated dimensionless fracture conductivities are shown in Figure 6.44. The results reveal that variation 3 (+50% viscosity) shows relatively larger modified weighted F<sub>CD</sub> and thus better performance.

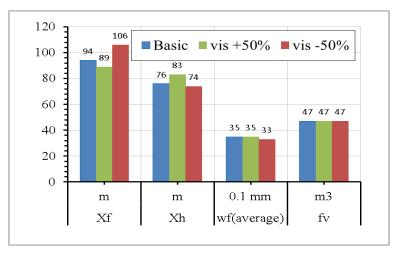


Figure 6.43 Comparison of the fracture geometry and volume at closure with varied viscosity

of the injection fluid

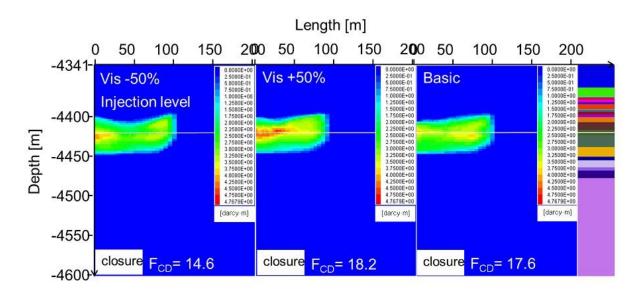


Figure 6.44 Comparison of the fracture conductivity contour and derived dimensionless fracture conductivity at closure with varied viscosity of the injection fluid

## 6.4.3 Injection time/rate

In these variation studies the total injection volume remains constant, while the injection time and injection rate were varied by  $\pm 20$  min (Figure 6.45).

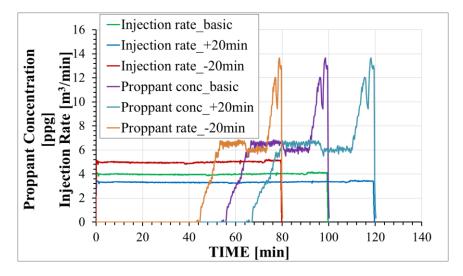


Figure 6.45 Varied injection time +20 min (Var. 5); -20min (Var. 6)

The simulation results of variation 6 (Figure 6.46) show higher fracture height compared with the basic results due to higher injection rate. But the average fracture width is smaller than that in the basic cases at closure. The fracture half-length and volume are the same as that in the basic results. The modified weighted  $F_{CD}$  shows the best hydraulic connection during the variation 5 (+20 min) (Figure 6.47).

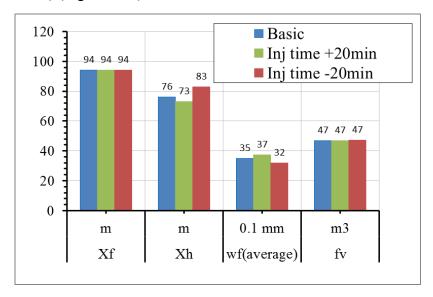


Figure 6.46 Comparison of the fracture geometry and volume at closure with varied injection time/rate

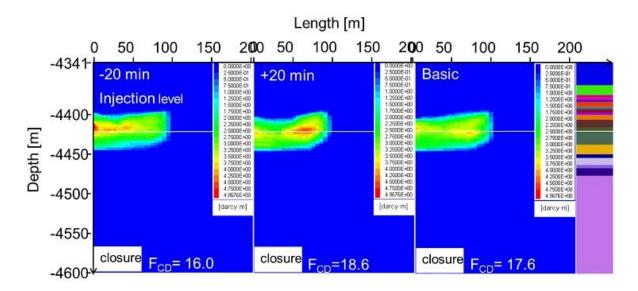


Figure 6.47 Comparison of the fracture conductivity contour and derived dimensionless fracture conductivity at closure with varied injection time/rate

### 6.4.4 Summary

The numerical simulation with different design parameters results show that the influences of proppant type on fracture geometry and fracture conductivity are much larger than that of the viscosity of the injection fluid, while the influences of the injection time are the smallest. CARBO-Lite 16/20 shows the best performance due to its lower density and larger diameter, which can lead to an abated settling effect and a larger supported fracture width to ensure high frac conductivity at high strength. Increasing viscosity (e.g. +50%) of the injected fluid and injection time (e.g. +20 min) show a little larger F<sub>CD</sub> and thus a little better performance.

### 6.5 Optimization of the treatment schedule and fracture number/spacing

Optimization criteria, such as estimation of the necessary number of hydraulic fractures, the perforation strategy, the estimation of the stress-log and general aspects of the fracture stimulation design, are important to the success of the tight gas project (Koehler & Kerekes 2006). From theoretical considerations, the number of fracture treatments depend on the reservoir permeability, the length of the well section within the potential layer (distance between the two border fractures), net thickness, fracture half-length, fracture conductivity, the expected compartments (estimated by means of LWD interpretations: sub-seismic faults and/or facies changes), vertical to horizontal permeability anisotropy ((kv/kh)-ratio) and the drainage radius (or assumed reservoir borders) (Koehler & Kerekes 2006). In this chapter, fracture number/spacing and treatment schedule of well Leer Z4 will be varied simulated and analyzed. The well Leer Z4 is drilled in the direction of the minimum horizontal stress, therefore the transverse fractures can be obtained. The spacing between perforations, the number and orientation of transverse fractures have major impacts on the well production performance. In this chapter optimization studies were carried out by varying the number of fractures and their spacing, as well as injection volume.

On one hand the number of fracture stimulations were varied between 3 and 5 (Figure 6.48).

For the case with 5 facture treatments, the fracture spacing is uniformly 120 m. The position of the first and the last fracture was kept unchanged. Here the new third and fourth fracture adopted the same treatment schedule as that of the third fracture in the basic case. The case with 4 fracture treatments is based on the case with 5 fractures, but the rightmost fracture was removed due to the connectivity problem by the perforation (section 6.1). The case with 3 fractures is based on the basic case, but the rightmost fracture was also removed due to the connectivity problem by the perforation (section 6.1).

On the other hand, the injection volume was also varied (Table 6.4). There are generally two groups of simulation, one with the original total injection volume of 1500 m<sup>3</sup> and with increased total injection volume of 1900 m<sup>3</sup>. For these variations, the injection time was unchanged, but the injection rate was varied.

The simulation results of the hydraulic fracturing are listed as fracture geometry in Table 6.5. With the increased injection volume/rate, the fracture geometry (e.g. fracture half-length and height) also increased.

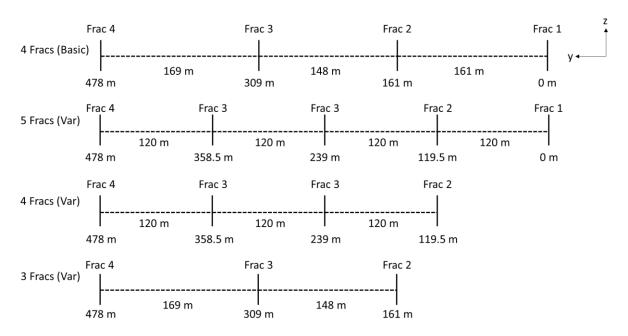


Figure 6.48 Variation of numbers of fracture treatments (3 - 5) and fracture spacing (120 - 169 m) with the corresponding fracture location (e.g. y = 478 m) and adopted treatment schedule (e.g. "Frac-stage 4")

Table 6.4 Variations with varied fracture location (y) and injection volume

	Injection volume [m <sup>3</sup> ] vs. Fracture location [m]									
	Total	478	358.5	309	239	161	119.5	0		
Basic	1,500	450	-	400	-	350	-	300		
(4 Fracs)										
Var. 1	1,500	375	337.5	-	300	-	262.5	225		
(5 Fracs)										
Var. 2	1,500	575	-	500	-	425	-	-		
(3 Fracs)										
Var. 3	1,900	708	-	633	-	558	-	-		
(3 Fracs)										
Var. 4	1,900	525	475	-	475	-	425	-		
(4 Fracs)										
Var. 5	1,900	450	400	-	400	-	350	300		
(5 Fracs)										

Table 6.5 Fracture geometry of the basic and varied fracture stimulation

Basic (4 Fracs)	Half- length [m]	Wavg [mm]	Height [m]	Inj vol. [m³]	Frac vol. [m <sup>3</sup> ]	Proppant mass [t]	Leak-off [%]
Frac 1	148	6.2	107	300	137	76	62%
Frac 2	84	3.5	63	350	35	83	96%
Frac 3	94	3.5	76	400	47	111	96%
Frac 4	100	5.2	88	450	75	129	91%
total				1500		399	

Var. 1 (5 Fracs)	Half- length [m]	W <sub>avg</sub> [mm]	Height [m]	Inj vol. [m³]	Frac vol. [m <sup>3</sup> ]	Proppant mass [t]	Leak-off [%]
Frac 1	148	9.2	107	222	139	56	44%
Frac 2	70	3.8	53	262.5	26	62	97%

Frac 3	84	3.8	63	300	36	83	96%
Frac 4	94	3.5	84	337.5	49	89	93%
Frac 5	89	5.6	85	375	72	109	89%
total				1500		399	

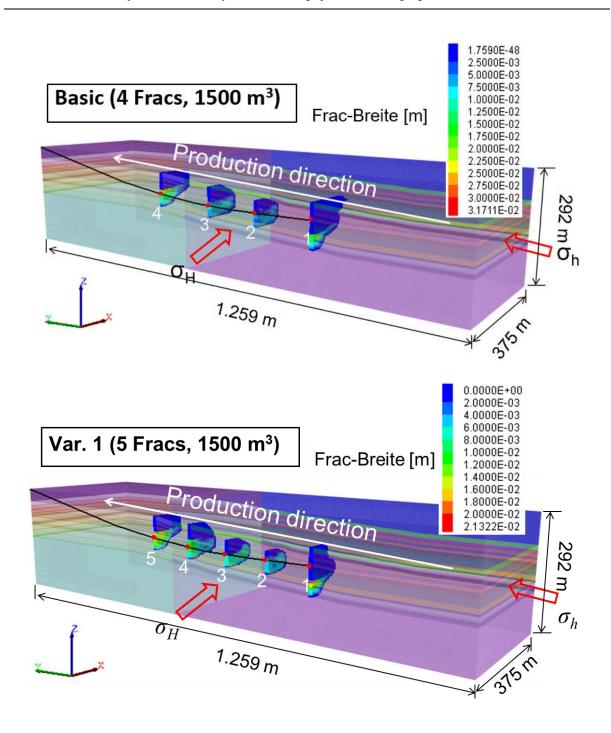
Var. 2 (3 Fracs)	Half- length [m]	W <sub>avg</sub> [mm]	Height [m]	Inj vol. [m³]	Frac vol. [m <sup>3</sup> ]	Proppant mass [t]	Leak-off [%]
Frac 1	89	3.7	73	425	45	98	96%
Frac 2	100	3.7	83	500	61	135	95%
Frac 3	119	5.1	105	575	99	166	91%
total				1500		399	

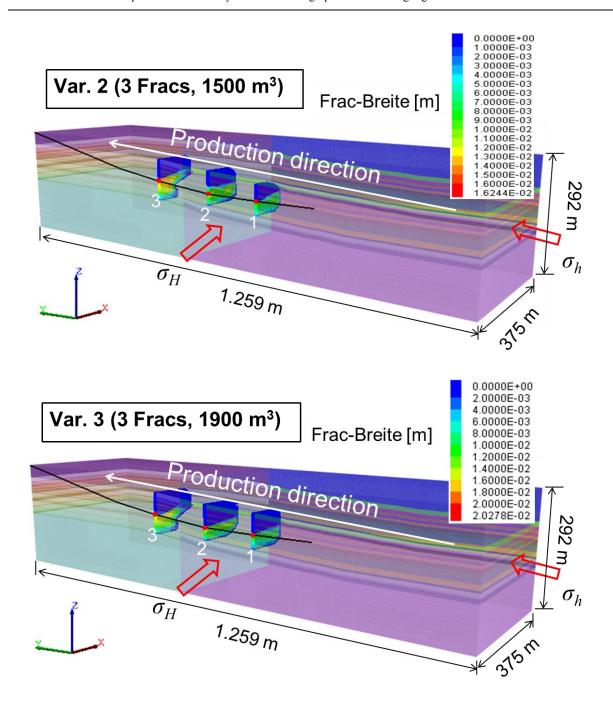
Var. 3 (3 Fracs)	Half- length [m]	W <sub>avg</sub> [mm]	Height [m]	Inj vol. [m³]	Frac vol. [m³]	Proppant mass [t]	Leak-off [%]
Frac 1	100	3.8	83	558	63	127	95%
Frac 2	119	4.3	86	633	89	171	94%
Frac 3	133	6.2	105	708	141	202	88%
total				1900		500	

Var. 4 (4 Fracs)	Half- length [m]	W <sub>avg</sub> [mm]	Height [m]	Inj vol. [m³]	Frac vol. [m <sup>3</sup> ]	Proppant mass [t]	Leak-off [%]
Frac 1	89	3.7	73	425	44	95	96%
Frac 2	100	5.6	84	475	92	128	88%
Frac 3	100	5.6	84	475	92	128	88%
Frac 4	106	5.5	103	525	93	149	90%
total				1900		500	

Var. 5 (5 Fracs)	Half- length [m]	W <sub>avg</sub> [mm]	Height [m]	Inj vol. [m³]	Frac vol. [m <sup>3</sup> ]	Proppant mass [t]	Leak-off [%]
Frac 1	148	6.2	107	304	137	76	62%
Frac 2	84	3.5	63	353	35	80	96%
Frac 3	94	3.5	76	397	47	108	96%
Frac 4	94	3.5	76	397	47	108	96%
Frac 5	100	5.2	88	449	75	128	91%
total				1900		500	

Based on the stimulation results a ½ 3D reservoir model (Figure 6.49) was generated, including created fractures with its own fracture width and proppant distribution. From the results of variations 1 (5 fractures, 1500 m³ injected) and 5 (5 fractures 1900 m³ injected) it can be seen, the first fracture was likely to propagate to the lower part of the reservoir because of the lower minimal horizontal stress in the lower part of the reservoir (section 6.1), even when the injection was increased. That means there is no proppant anymore at the middle part of the fracture, where the perforation is located. This could be the reason for the lower productivity, because the perforation got a poor connectivity to the propped fracture. From the results of variation 2 (3 fractures, 1500 m³ injected) and variation 3 (3 fractures 1900 m³ injected) it can be seen, that the fracture half-length and height has increased due to the increased injection volume. However, there is no proppant any more at the perforation of fracture 3. Compared variation 4 with basic results, the fracture half-length and height has also increased by variation 4 due to the increased injection volume.





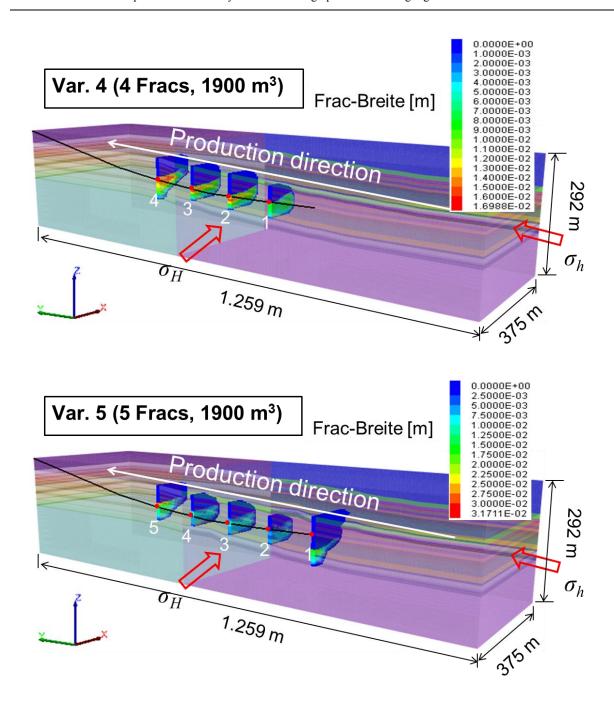


Figure 6.49 ½ 3D model geometry and geological stratigraphy including created fractures of varied fracture spacing and injection volume

The gas production results are listed in Table 6.6. Because of the eliminated fracture 1 and increased fracture volume the variation 4 (4 fractures with 120 m fracture spacing and 1900 m<sup>3</sup> injection volume) shows the highest produced gas volume. That means, an increase of 26.7% injection volume results in 12.7% more gas volume. The results of variation 3 (3 equally spaced

fractures as that in the basic case and 1900 m<sup>3</sup> injection volume) is also noteworthy. The produced gas volume is even reduced (-12.8%) compared to the basic situation. The reason for this is the insufficient support at perforation by fracture 3 (Figure 6.49). That means, the injection rate is not, the higher the better. If it is too high, the fracture width becomes too big, then proppant settles down easier to the bottom. Thus, the hydraulic connection between fracture and wellbore is insufficient. This is a counter example.

Although the total injection volume in the variation 1 (5 fractures, 1500 m³) and variation 2 (3 fractures, 1500 m³) was the same as that of the basic simulation, the produced volume has increased slightly. This is because the total fracture volume was increased by variation 1 with increased fracture number, which leads to a broader influence area, so that more gas can be produced. By variation 2, although the fracture number reduced, the individual fracture volume has increased. And what's more important is that the original low-productive fracture 1 has been removed. The injection fluid for this fracture has been injected to the other 3 fractures. Thus, the fractures in variation 2 have larger area und more gas has been produced, compared with variation 1. By variation 4 fracture 1 has also been removed and the other 3 fractures have larger area.

The estimation of fracture positions is based on logging results and influenced by sub-seismic faults and compartments. Optimum number of fracture stimulations are based on local conditions, numerical simulation and literature. (Koehler & Kerekes 2006)

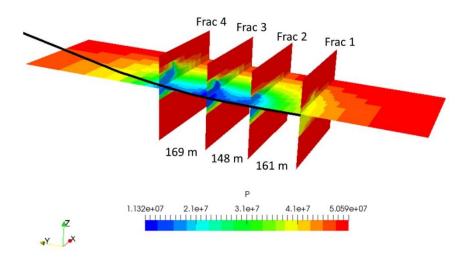
Due to the expected fracture half length, different injection volumes are planned. According to the numerical simulation results (Table 6.6), the optimal number of the fracture stimulations in the well Leer Z4 is 3-4 fracture treatments. With a total injection volume of 1500 m³ the best fracture number is 3>5>4. In the meantime, the best fracture number is 4>5>3 for a total injection volume of 1900 m³. The sequence is reversed. The injection rate is not, the higher the better. It could lead to proppant settle down quicker to the bottom of the fracture. That means, there is no uniform and unique criterion to determine the number and spacing of the fracture, it should be analyzed in detail based on the local condition, numerical simulation and literature.

Table 6.6 Comparison of the produced gas volume

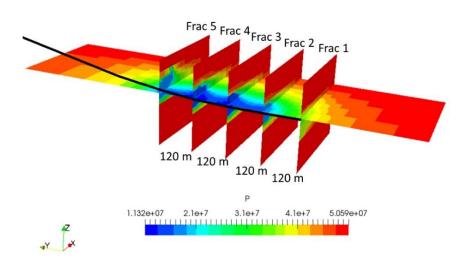
06. 2006 ~ 12. 2009	Produced gas	Increased gas	Increased inj.
	volume	volume vs basic	volume vs basic
	[Mio. sm <sup>3</sup> ]	[%]	[%]
Basic (4 Fracs, 1500 m <sup>3</sup> )	276	-	-
Var. 1 (5 Fracs, 1500 m <sup>3</sup> )	288	+4.3	0
Var. 2 (3 Fracs, 1500 m <sup>3</sup> )	289	+4.5	0
Var. 3 (3 Fracs, 1900 m <sup>3</sup> )	241	-12.8	+26.7
Var. 4 (4 Fracs, 1900 m <sup>3</sup> )	311	+12.7	+26.7
Var. 5 (5 Fracs, 1900 m <sup>3</sup> )	303	+9.8	+26.7

The pore pressure distribution at t = 3.5 years is shown in Figure 6.50. It varied from 11 MPa to 50 MPa. The lower pore pressure means more gas are produced. The pore pressure distribution can also be used to evaluate the performance of the production. The problem of the basic simulation, variation 1 and 5 mentioned above can also been explained with Figure 6.50a, Figure 6.50b, Figure 6.50f. During the production, the pore pressure of fracture 1, which located at 0 m in y-direction reduced less than the other fractures due to deficient propped fracture.

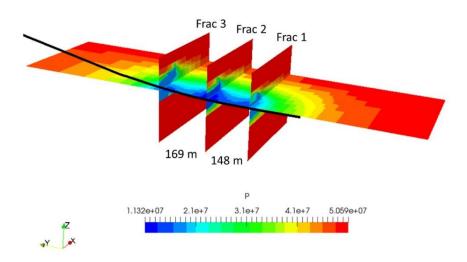
The same problem of variation 3 can also been seen in Figure 6.50d, during the production the pore pressure of fracture 3 reduced less than other 2 fractures due to deficient propped fracture.



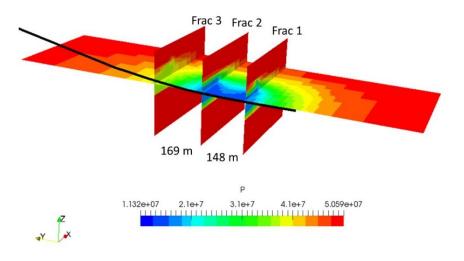
a. Basic: 4 fracs with 1500 m³ injection volume



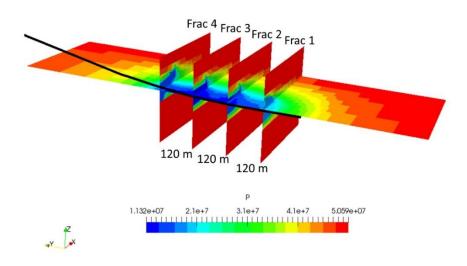
b. Variation 1: 5 fractures with 120 m fracture spacing and 1500 m³ injection volume



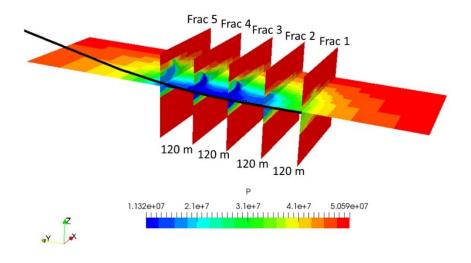
c. Variation 2: 3 fractures with the same fracture spacing as that in the basic case and 1500 m3 injection volume



d. Variation 3: 3 fractures with the same fracture spacing as that in the basic case and  $1900 \text{ m}^3$  injection volume



e. Variation 4: 4 fractures with 120 m fracture spacing and 1900 m³ injection volume



f. Variation 5: 5 fractures with 120 m fracture spacing and 1900 m³ injection volume

Figure 6.50 Pore pressure distribution at t=3.5 years by varied fracture number and

injection volume

## 7 Conclusions and outlook

The most produced natural gas is in conventional reservoir with well-permeable rocks. The natural gas flows without further technical effort to the borehole. In the tight gas reservoir, natural gas located in the pore space of low-permeability sandstone layers, where it must first be mobilized by technical measures before it can be pumped. Thus, multi-fracs and horizontal borehole technology are used.

By high-pressure injection of the fracture fluid targeted millimeter-thin flow paths are generated in the reservoir. So that the artificially created flow paths remain permanently open, the proppant is necessary. They are distributed in the flow paths so that the natural gas can flow better to the bore via an enlarged contact surface.

Economic optimization can be based on the following aspects: suitable fracture propagation models, reservoir formation suitable and environmentally friendly fracture fluid systems, selection of proppant and maximum permissible pump capacity. Optimization methods are e.g. In-situ measurements and numerical simulations, namely history matching and optimization. In the oil and gas industry, there are many numerical tools that are commonly used for modeling, fracturing and production. So far, there is no tool that can optimize the whole process with the same 3D model, considering the thermo-hydromechanical coupling. Man always have to convert and adjust the result from one phase for the next phase. Actually, optimizing each frac during the stimulation phase does not represent the performance of the entire horizontal well. The fractures interact with each other during the production process. Therefore, the optimization design should also be considered from the production perspective, especially for multi-fracs. In this work a novel combination of different simulation tools for the modeling of the complex fracturing process from initiation to production was developed.

The concept is based on the numerical model for hydraulic fracturing and the associated reservoir simulation model for gas production. This concept was realized through the coupling of FLAC3D<sup>plus</sup>, TMVOCMP and optiSLang. With these tools, a 3D simulation model can be generated according to the measured geological and geophysical data and verified with the

measured treatment and production data. Based on the verified models, numerical simulations with varied design parameters can be performed to optimize tight gas production.

Firstly, the Frac-Simulator optiSLang-FLAC3D<sup>plus</sup> was developed to match the fracturing operation history automatically and optimize the hydraulic fracturing with consideration of thermal effect and gel-breaking. The temperature change will affect the fracture propagation process directly through the thermal stress as well as expansion or shrinkage. The temperature can also influence the fluid properties (gel breaking) as well. In the extended coupled simulator FLAC3D<sup>plus</sup> the equation for heat transport in the fracture is solved using Finite-Volume-Method (FVM) and that in the formation is solved using Finite-Difference-Method (FDM). The software optiSLang can be used for the parameter optimization during hydraulic fracturing. To match the in-situ measured surface pressure, an inverse calculation is required. During the coupling between optiSLang and FLAC3D<sup>plus</sup> all parameters (e.g. wall roughness coefficient, viscosity of basis fluid etc.), including their start values and bandwidths, will be defined at first. With the help of sensitivity analysis, the designer identifies the variables which contribute mostly to a possible improvement of the optimization goal. Based on this identification, the number of design variables may be dramatically reduced, and an efficient optimization can be performed. For the verification the extended simulator optiSLang-FLAC3D<sup>plus</sup> was applied in the hydraulic fracturing simulation in a fictive tight gas reservoir. During the verification the time-dependent pressure curve was simulated with predefined parameters at first. Then it is matched using the coupled simulator by only defining the start values and bandwidth of these parameters. Through the inverse calculation the parameters were determined, which are very close to the predefined values.

After the verification, a numerical application of a hydraulic fracture operation at four fracstages in a real tight gas reservoir Leer is illustrated, which was done in 2005. Comparing the simulation results from FLAC3D<sup>plus</sup> and FracPro for four frac-stages, it could be concluded that the difference between them is small and can be neglected. At frac-stage 1 there is no proppant in the middle part of the fracture at fracture closure, where the perforation is located. This could be the reason for the later lower productivity, because the perforation got a poor connectivity to the propped fracture. The dimensionless fracture conductivity  $F_{CD, prats}$  of Leer Z4 is 2 < 1 < 3 < 4.

Secondly, to maximize the productivity of the above mentioned tight gas wellbore, Frac-Produ Simulator optiSLang-FLAC3D<sup>plus</sup>-TMVOCMP was developed for the simulation of the gas production. It considers the coupled thermo-hydro-mechanical effects. The change of stress tensor and the fracture conductivity during gas production are also considered. After the verification, a full 3D reservoir model is generated, including in the hydraulic fracturing operation created four fractures with their fracture geometries and proppant contribution. The bottomhole pressure derived from the measured treating pressure was used as input for the stress sensitive reservoir simulation. According to the results, the simulated decline of production rate agrees with the in-situ measured data. The gas rate of each fracture at the beginning of the production is 1 < 2 < 4 < 3, which is not consistent with those of F<sub>CD, prats</sub>. The reason is that the proppant distribution and concentration, especially the distance from the propped area to the perforation, are not considered by F<sub>CD, prats</sub>. For this reason, a new modified weighted calculation formula of F<sub>CD</sub> was proposed, which takes the proppant position and concentration into account. Now the gas rate of each fracture at the beginning of the production is the same as the prediction by modified weighted  $F_{CD}$  (1 < 2 < 4 < 3). But not only  $F_{CD}$  but also geological structure and the interaction between fractures are determinant for the gas production volume of each fracture. Hence, the relationship between gas production rates from each fracture in the later production is different from that at the beginning (as well as the F<sub>CD</sub>). The results of sensitivity analysis with different design parameters show that the influences of proppant type on fracture geometry and fracture conductivity is much larger than that of viscosity of the injection fluid, while the influences of the injection time are the smallest. CARBO-Lite 16/20 shows the best performance due to its lower density and larger diameter, which can lead to an abated settling effect and a larger supported fracture width to ensure high frac conductivity at high strength. Enhanced viscosity (e.g. +50%) of the injection fluid and longer injection time (+20 min) or lower rate show a little larger F<sub>CD</sub> and thus a little better performance.

Numerical simulation with varied fracture number/spacing and treatment schedule results show that the injection rate is not, the higher the better. If it is too high, the fracture width will become wider and the proppant will settle down easier to the bottom, which leads to insufficient hydraulic connection between fracture and wellbore. The fracture spacing should also not be too small, otherwise the influence area/drainage radius is not enough. Due to the expected fracture half length, different injection volumes are planned. The optimum design for fractures stimulations of well Leer Z4 is 4 fractures with 120 m fracture spacing and 1900 m<sup>3</sup> injection volume or 3 fractures with 148 to 169 m fracture spacing and 1500 m<sup>3</sup> injection volume. That means, there is no uniform and unique criterion to determine the number and spacing of the fracture, it should be analyzed in detail based on the local condition, numerical simulation and literature.

For future research an alternative fracturing fluid will be developed without any chemical ingredients and water, e.g. gas frac. In addition, the natural fractured systems will also be considered in the later numerical simulation, e.g. shale gas reservoir.

## References

Adachia J, Siebritsb E, Peircec A, Desrochesd J (2007) Computer simulation of hydraulic fractures, Int. J. Rock Mech. Min. Sci., 44(5):739-757. doi:10.1016/j.ijrmms.2006.11.006

Agarwal RG, Al-Hussainy R, Ramey HJ Jr (1970) An Investigation of Wellbore Storage and Skin Effect in Unsteady Liquid Flow: I. Analytical Treatment, paper SPE 2466, SPE Journal 10(3): 279–290. doi: 10.2118/2466-PA

Agnew BG (1966) Evaluation of Fracture Treatments with Temperature Surveys, J. Pet. Tech. Society of Petroleum Engineers, 18(07): 892-898. doi: 10.2118/1287-PA

Allen LS, Tittle CW, Mills WR and Caldwell RL (1967) Dual Spaced Neutron Logging for Porosity, Geophysics 32(1):60-68. doi: 10.1190/1.1439857

Amyx B, et al. (1960) Petroleum Reservoir Engineering Physical Properties, McGraw Hill. ISBN-13: 978-0070016002

Bell JS (1990) The stress regime of the Scotian Shelf offshore eastern Canada to 6 kilometers depth and implications for rock mechanics and hydrocarbon migration, - In: Maury, V. and D. Fourmaintraux, eds., Rock at Great Depth, Rotterdam, Balkema, 1243-1265, ISBN 9061919754

Barree R, Conway M (1995) Experimental and numerical modeling of convective proppant transport, Journal of Petroleum Technology, 47(3):216-222. doi: 10.2118/28564-PA

Bartz V (2010) Depth Structure Map Top Wustrow Member. GDF SUEZ, Geology Department

Bell JS, Gough DI (1979) Northeast-southwest compressive stress in Alberta: Evidence from oil wells, Earth Planet. Sci. Lett., 45(2):475-482. doi: 10.1016/0012-821X(79)90146-8

Biot MA (1956b) Theory of Propagation of Elastic Waves in a Fluid-Saturated Porous Solid. I. Low Frequency Range, J. Acoust. Soc. Am. 28(2):168–178

Biot MA (1956c) Theory of Propagation of Elastic Waves in a Fluid-Saturated Porous Solid, II. High Frequency, J. Acoust. Soc. Am. 28(2):179–191

Blair Kent (2015) MODIFYING FRACTURE CONDUCTIVITY TESTING PROCEDURES, Graduate Theses & Non-Theses, Paper 60

Bourdet D, Whittle TM, Douglas AA, and Pirard YM (1983) A New Set of Type Curves Simplifies Well Test Analysis, World Oil, 196(6): 95–106

Bradford IDR, Fuller J, Thompson PJ, Walsgrove TR (1998) Benefits of assessing the solids production risk in a North Sea reservoir using elastoplastic modelling, SPE/ISRM Rock Mechanics in Petroleum Engineering, 8-10 July, Trondheim, Norway. doi:10.2118/47360-MS

Brink HJ (2005) The evolution of the North German Basin and the metamorphism of the lower crust, International Journal of Earth Sciences, 94(5): 1103–1116. doi: 10.1007/s00531-005-0037-7

Brooks RH, Corey AT (1966) Properties of Porous Media Affecting Fluid Flow, J. Irrig. Drain. Div., 6:61-88.

Bruce R Meyer et al. (2010) Optimization of Multiple Transverse Hydraulic Fractures in Horizontal Wellbores, SPE 131732, SPE Unconventional Gas Conference held in Pittsburgh, Pennsylvania, USA

Bui HD (1977) An Integral Equations Method for Solving the Problem of a Plane Crack of Arbitrary Shape, J. Mech. Phys. Solids. 25(1):29-39. doi:10.1016/0022-5096(77)90018-7

Burdine NT (1953) Relative Permeability Calculations from Pore Size Distribution Data, Journal of Petroleum Technology, 198(03):71-78. doi: 10.2118/225-G

CARBO Ceramics (2006) Proppant CARBOHSP data sheet, internal report of CARBO Ceramics Inc.

Carrier B, Granet S (2011) Numerical modeling of hydraulic fracture problem in permeable medium using cohesive zone model, Engineering Fracture Mechanics, Elsevier, 79:312–328. doi:<10.1016/j.engfracmech.2011.11.012>. <hal-00670787>

Carter RD (1957) Derivation of the General Equation for Estimating the Extent of the Fractured Area, Appendix I of "Optimum Fluid Characteristics for Fracture Extension, Drilling and Production Practice, G.C. Howard and C.R. Fast, New York, New York, USA, American Petroleum Institute, 261–269

Castillo JL (1987) Modified Fracture Pressure Decline Analysis Including Pressure-Dependent Leakoff, paper SPE 16417, presented at the SPE/DOE Low Permeability Reservoirs Symposium, Denver, Colorado, USA. doi: 10.2118/16417-MS

Charlez Philippe A (1997) Rock Mechanics: Petroleum Applications, Paris: Editions Technip, 2: 239. ISBN:9782710805861. Retrieved 05 May 2017

Cipolla CL, Wright CA (2000) Diagnostic Techniques to Understand Hydraulic Fracturing: What? Why? and How? SPE/CERI Gas Technology Symposium, 3-5 April, Calgary, Alberta, Canada. doi:10.2118/59735-MS

Cleary MP (1980b) Comprehensive Design Formulae for Hydraulic Fracturing, paper SPE 9259, presented at the SPE Annual Technical Conference and Exhibition, Dallas, Texas, USA, 21–24. doi: 10.2118/9259-MS

COMSOL (2012) COMSOL Multiphysics User's Guide (Version 4.3)

Corey AT (1954) The Interrelation between Gas and Oil Relative Permeabilities, Prod. Mon., 19:38-41.

Crone Trevor (2015) Horizontal Drilling: How Do They Get It To Go Sideways? RIGZONENEWS. https://rigzonenews.wordpress.com/2015/02/25/horizontal-drilling-how-do-they-get-it-to-go-sideways/. Retrieved 03 June 2017

Crump J, Conway M (1988) Effects of Perforation-Entry Friction on Bottomhole Treating Analysis, Paper SPE 15474, Journal of Petroleum Technology, 40(8):1041–

1048.doi:10.2118/15474-PA

Dake L (1982) Fundamentals of Reservoir Engineering, Developments in Petroleum Science, volume 8, Amsterdam, Netherlands, Elsevier Scientific Publishing Company. ISBN:0-444-41830-X

Darcy H (1856) Les Fontaines Publiques de la Ville de Dijon, Paris, France, Victor Dalmont, page 647

Davis ER, Zhu D, Hill AD (1997) Interpretation of Fracture Height from Temperature Logs - The Effect of Wellbore/Fracture Separation, Society of Petroleum Engineers, 12(02): 119-124, doi: 10.2118/29588-PA

Detournay E & Carbonell R (1994) Fracture Mechanics Analysis of the Breakdown Process in Minifrac or Leak-Off Tests, paper SPE 28076, presented at the SPE/ISRM Rock Mechanics in Petroleum Engineering Conference, Delft, Netherlands. ISBN:905410502X

Dynardo (2014): optiSLang Manual, Version 4.2.0. Dynamic Software and Engineering GmbH, Weimar, Germany

Economides MJ, Nolte KG (2000) Reservoir Stimulation, 3rd Edition. Wiley VCH. ISBN:978-0471491927

Ehlig-Economides CA (1995) Implications of the Test Area of Investigation in Nonradial Geometries, SPE Memorial Series, Richardson, Texas, USA, Society of Petroleum Engineers 1:103–112

EIA (U.S. Energy Information Administration) (2016) International Energy Outlook 2016. DOE/EIA-0484

Eissa M, King S, Abdulrahman A (2007) Experimental and numerical investigation of proppant placement in hydraulic fractures, In: Proceedings of SPE Latin American and Caribbean Petroleum Engineering Conference. Buenos Aires, Argentina, 15–18 April. doi: 10.2118/107927-MS

Engelder T (1993) Stress Regimes in the Lithosphere, Princeton, New Jersey, USA, Princeton University Press, ISBN:9781400863150

Evans KF, Engelder T, Plumb RA (1989) Appalachian Stress Study: 1. A Detailed Description of In-Situ Stress Variations in Devonian Shales of the Appalachian Plateau, Journal of Geophysical Research, 94(B6): 7129–7154. doi:10.1029/JB094iB06p07129

Fekete Associates Inc. (2012) Minifrac Tests. http://www.fekete.com/SAN/TheoryAndEquations/WellTestTheoryEquations/Minifrac.htm, Retrieved 12 June 2017

Feng WT, Were P, Li MT, Hou Michael Z, Zhou L (2016) Numerical study on hydraulic fracturing in tight gas formation in consideration of thermal effects and THM coupled processes, Journal of Petroleum Science and Engineering, 146:241-254. doi:10.1016/j.petrol.2016.04.033

Flemisch B, Darcis M, Erbertseder K, Faigle B, Lauser A, Mosthaf K, et al. (2011) DuMux: DUNE for Multi-{Phase, Component, Scale, Physics, ...} Flow and Transport in Porous Media. Advances in Water Resources 34(9):1102-1112. doi:10.1016/j.advwatres.2011.03.007

Fourier J (1878) Analytical Theory of Heat, Cambridge University Press, London

Gadde P, Liu Y, Norman J, Bonnecaze R, Sharma M (2004) Modeling proppant settling in water-fracs, In: Proceedings of the SPE Annual Technical Conference and Exhibition. Houston, USA, 26–29 September. doi: 10.2118/89875-MS

Gadde P, Sharma M (2005) The impact of proppant retardation on propped fracture lengths, In: Proceedings of the SPE Annual Technical Conference and Exhibition. Dallas, USA, 9–12 October

Garagash D, Detournay E (2005) Plane-strain propagation of a hydraulic fracture: small toughness solution, J Appl Mech, 72(6):916–928. doi: 10.1115/1.2047596

Geertsma J, De Klerk F (1969) A rapid method of predicting width and extent of hydraulically induced fractures, Journal of Petroleum Technology, 21 (12):1571-1581. doi:10.2118/2458-PA

Gemmer L, Nielsen SB, Bayer U (2003) Late Cretaceous—Cenozoic evolution of the North German Basin—results from 3-D geodynamic modeling, Tectonophysics, 373(1-4):39-54. doi: 10.1016/S0040-1951(03)00282-8

George G (1993) A new lithostratigraphy and depositional model for the Upper Rotliegend of the UK Sector of the Southern North Sea, Geological Society Special publications, 73: 291–319. doi:10.1144/gsl.sp.1993.073.01.18

Gou Y, Hou Z, Liu H, Zhou L, Were P (2014) Numerical simulation of carbon dioxide injection for enhanced gas recovery (CO<sub>2</sub>-EGR) in Altmark natural gas field. Acta Geotechnica, 9(1):49–58. doi: 10.1007/s11440-013-0221-z

Ground Water Protection Council; ALL Consulting (2009) Modern Shale Gas Development in the United States: A Primer (Report), DOE Office of Fossil Energy and National Energy Technology Laboratory. pp. 56–66. DE-FG26-04NT15455. Retrieved 14 May 2017

Guo F, Morgenstern NR, Scott JD (1993) Interpretation of Hydraulic Fracturing Breakdown Pressure, International Journal of Rock Mechanics and Mining Sciences & Geomechanics, 30(6):617–626. doi: 10.1016/0148-9062(93)91221-4

Häfner F, Pusch mont. G, Klafki M et al. (2006) Simulation of the production behaviour of hydraulically fractured wells in Tight Gas Reservoir,. DGMK-Research Report 593-9/2 Phase II. ISBN: 3-936418-37-3

Haimson BC (1993) The Hydraulic Fracturing Method of Stress Measurement: Theory and Practice, Comprehensive Rock Engineering, J. Hudson (ed.), Oxford, UK, Pergamon Press, 3:(297–328). doi:10.1016/B978-0-08-042066-0.50021-5

Haimson BC, Huang X (1989) Hydraulic Fracturing Breakdown Pressure and In-Situ Stress at Great Depth, Rock at Great Depth, V. Fourmaintraux and D. Maury (eds.), Rotterdam,

Netherlands, Balkema, 939-946. ISBN: 9061919754

Halliday D, Resnick R, Walker J (2013) Fundamentals of Physics, 9th ed. Wiley, London. ISBN-10:111823071X, ISBN-13:978-1118230718

Itasca (2009) FLAC3D Manual, Version 4.0. ITASCA Consulting Group, Inc

Hubbert MK, Willis DG (1957) Mechanics of Hydraulic Fracturing, SPE-686-G, presented at the SPE Annual Meeting, Los Angeles, California, USA (October 14–17, 1956); also in Journal of Petroleum Technology (September 1957), 9(6): 153–168 and Trans., AIME (1957) 210:153-168

Ito T, Hayashi K (1991) Physical Background to the Breakdown Pressure in Hydraulic Fracturing Tectonic Stress Measurements, International Journal of Rock Mechanics and Mining Sciences & Geomechanics Abstracts 28(4): 285–293. doi:10.1016/0148-9062(91)90595-D

Hartnett-White K (2011) The Fracas About Fracking - Low Risk, High Reward, but the EPA is Against it. National Review Online. Retrieved 15 May 2017

Heidbach O, Rajabi M, Reiter K, Ziegler M, WSM Team (2016) World Stress Map Database Release 2016, GFZ Data Services. doi:10.5880/WSM.2016.001

Hirth JP and Lothe J (1968) Theory of Dislocations, New York, New York, USA, McGraw-Hill. ISBN:0-89464-617-6

Hou Z, Li M, Yang G, Feng W (2018) Numeric Investigations on Frac Propagation in Tight Gas Reservoirs with the FDM Program FLAC3D – Phase 4: Optimization of a complete fracoperation in a horizontal well concerning maximum productivity. *DGMK*, *Hamburg*, 2018.

Hou Z & Zhou L (2015) Numeric Investigations on Frac Propagation in Tight Gas Reservoirs with the FDM Program FLAC3D – Phase 3: Proppant Transport in Fluid and Closure Process. *DGMK*, *Hamburg*, February 2015 (ISBN 978-3-941721-57-9).

Horner DR (1951) Pressure Buildup in Wells, Proc., Third World Petroleum Congress, The Hague, Netherlands Sec. II, 503–523; also in Pressure Analysis Methods, SPE Reprint Series, Richardson, Texas, USA, Society of Petroleum Engineers (1967) 9, 25–43

Hubscher C, Hansen MB, Trinanes SP, Lykke-Andersen H, Gajewski D (2010) Structure and evolution of the Northeastern German Basin and its transition onto the Baltic Shield, Marine and Petroleum Geology, 27(4):923-938. doi: 10.1016/j.marpetgeo.2009.10.017

Khristianovic SA, Zheltov YP (1955) Formation of vertical fractures by means of highly viscous liquid, In Proceedings of the fourth world petroleum congress, pages 579 – 586, Rome, Italy. doi: WPC-6132

King George E (2012) Hydraulic fracturing 101. Society of Petroleum Engineers, SPE 152596 – via Kansas Geological Survey

Koehler M (2004) Project Leer Z4: G&G\_Peer-Presentation. Internal presentation of ENGIE E&P Deutschland GmbH

Koehler M (2005a) Project Leer Z4: Fracture Stimulation Fracture 1. Internal presentation of ENGIE E&P Deutschland GmbH

Koehler M (2005b) Leer Z3a/Z4: Rock-Mechanical Data Base. Internal presentation of ENGIE E&P Deutschland GmbH

Koehler M, Kerekes F (2006a) Rotliegend Tight Gas Field Leer: A Development with a Multiple Hydraulically Fractured Horizontal Well: Project Leer Z4. DGMK-Frühjahrstagung 2006, ISBN 3-936418-48-9

Koehler M, Kerekes F (2006b) Entwicklung einer "tight gas"-Lagerstätte mit einer mehrfach hydraulisch stimulierten Horizontalbohrung: Projekt Leer Z4. Interne präsentation von ENGIE E&P Deutschland GmbH

Koehler M (2008) Rotliegend "Tight Gas" Field Leer (Ostfriesland): Field Development with Focus on: Petrophysics, Rock Mechanics, Stimulation Technology, Production Experiences, Outlook on Future Wells and Lessons Learned (Section: Reservoir Engineering). Internal presentation of ENGIE E&P Deutschland GmbH

Kolditz O, Bauer S, Bilke L, Böttcher N, Delfs JO, Fischer T, et al. (2012) OpenGeoSys: an open-source initiative for numerical simulation of thermo-hydro-mechanical/chemical (THM/C) processes in porous media. Environ. Earth Sci., 67(2): 589–599. <a href="http://dx.doi.org/10.1007/s12665-012-1546-x">http://dx.doi.org/10.1007/s12665-012-1546-x</a>

Kolditz O, Xie H, Hou Z, Were P, Zhou H (Eds.) (2015) The Thematic Issue: Subsurface energy

Systems in China: production, storage and conversion. *Environ Earth Sci* 73(11):6727—6732

Kolditz O, Görke UJ, Shao H, Wang W, Bauer S (Eds.) (2016) Thermo-Hydro-Mechanical-Chemical Processes in Fractured Porous Media: Modelling and Benchmarking. Springer International Publishing. ISBN:978-3-319-29224-3

Lacy LL (1997) Dynamic rock mechanics testing for optimized fracture designs. SPE Annual Technical Conference and Exhibition, 5-8 October, San Antonio, Texas, USA. doi:10.2118/38716-MS

Lamb H (1916) Hydrodynamics, fourth edition, Cambridge University Press, London

Lamb H (1932) Hydrodynamics, sixth edition, New York, New York, USA, Dover Publications, 581–587

Lane HS (1993) Numerical Simulation of Mud Filtrate Invasion and Dissipation, Transactions of the SPWLA 34th Annual Logging Symposium, paper D. doi: SPWLA-1993-D

Leshchyshyn TH (2004) Using Empirically Developed Rock Tables to Predict and History Match Fracture Stimulations, SPE 86089, SPE International Thermal operations and Heavy Oil Symposium and Western Regional Meeting, Bakersfield, California, USA. doi:10.2118/86989-MS

Li MT, Gou Y, Feng WT, Hou MZ (2015) Zweiter Zwischenbericht vom Projekt DGMK680-

IV, Goslar, germany

Li MT, Hou MZ, Gou Y, Feng WT (2016) Optimization of a Complete Fracking-operation for the Maximum Productivity from a Tight Gas Reservoir, DGMK/ÖGEW-Frühjahrstagung 2016, Fachbereich Aufsuchung und Gewinnung, Celle, Germany, DGMK-Tagungsbericht 2016-1, ISBN 978-3-941721-64-7

Li MT, Hou MZ, Gou Y, Feng WT (2017) History Matching and Preliminary Optimization of the Whole Process from Multiple Hydraulic Fracturing till Production in a Tight Gas Horizontal Well Using the Newly Developed THM-simulator FLAC3D<sup>plus</sup>-TMVOCMP, DGMK/ÖGEW-Frühjahrstagung 2017, Fachbereich Aufsuchung und Gewinnung, Celle, Germany, DGMK-Tagungsbericht 2017-1, ISBN 978-3-941721-73-9

Liu C, Liu H, Zhang YP, Deng DW, Wu HA (2015) Optimal spacing of staged fracturing in horizontal shale-gas well, Journal of Petroleum Science and Engineering, 132:(86-93). doi: 10.1016/j.petrol.2015.05.011

Liu Y (2006) Settling and Hydrodynamic Retardation of Proppants in Hydraulic Fractures (Dissertation), University of Texas at Austin

Martin Emanuel (2017) WHAT IS HYDRAULIC FRACTURING? Part A. http://allaboutshale.com/what\_is\_hydraulic\_fracturing\_emanuel\_martin.html. Retrieved 03 June 2017

Martins JP, Abel JC, Dyke CG, Michel CM and Stewart G (1992a) Deviated Well Fracturing and Proppant Production Control in the Prudhoe Bay Field, SPE 24858, presented at the SPE Annual Technical Conference and Exhibition, Washington, D.C., USA

Meyer BR (1989) Three-Dimensional Hydraulic Fracturing Simulation on Personal Computers: Theory and Comparison Studies, paper SPE 19329. doi: 10.2118/SPE-19329-MS

Meyer & Associates, Inc. (2012) User's Guide of Meyer Fracturing Simulators, 9th Edition

Minh CC, Freedman R, Crary S and Cannon D (1998) Integration of NMR with Other Openhole Logs for Improved Formation Evaluation, paper SPE 49012, presented at the SPE Annual Technical Conference and Exhibition, New Orleans, Louisiana, USA, doi: 10.2118/49012-MS

Mockovciakova A, Pandula B (2003) Study of the relation between the static and dynamic moduli of rocks, Metabk 42(1):37-39. ISSN:0543-5846

Montgomery, Carl T, Smith, Michael B (2010) Hydraulic fracturing - History of an enduring technology, JPT Online. Society of Petroleum Engineers, 62(12):26–41. Archived from the original (PDF) on 2011-09-27. Retrieved 06 May 2017. doi: 10.2118/1210-0026-JPT

Morales RH, Marcinew RP (1993) Fracturing of high-permeability formations: mechanical properties correlations, SPE Annual Technical Conference and Exhibition, 3-6 October, Houston, Texas, USA. doi:10.2118/26561-MS

Most T, Will J (2008) Metamodel of Optimal Prognosis - An automatic approach for variable

reduction and optimal metamodel selection, Presented at the Weimar Optimization and Stochastic Days 2008. Source: www.dynardo.de/en/library

Müller B et al. (2004) Spannungsreorientierung an geologischen Strukturen in Sedimentbecken, DGMK-Forschungsbericht 593-5, Hamburg

Nolte KG (1979) Determination of Fracture Parameters from Fracturing Pressure Decline, paper SPE 8341, presented at the SPE Annual Technical Conference and Exhibition, Las Vegas, Nevada, USA, doi:10.2118/8341-MS

Nolte KG (1982) Fracture Design Considerations Based on Pressure Analysis, paper SPE 10911, presented at the SPE Cotton Valley Symposium, Tyler, Texas, USA. doi: 10.2118/10911-MS

Nolte KG (1988a) Application of Fracture Design Based on Pressure Analysis, paper SPE 13393, SPE Production Engineering, 3(1): 31–42. doi: 10.2118/13393-PA

Nordgren RP (1972) Propagation of a vertical hydraulic fracture, SPE J, 12(4):306-314. doi: 10.2118/3009-PA

Paillet FL, Chang CH (1991) Acoustic Waves in Boreholes, CRC Press, Inc., Boca Raton, Florida, USA. ISBN:9780849388903

Palisch T, Duenckel R, Chapman M, Woolfolk S, Vincent MC (2009) How to Use and Misuse Proppant Crush Tests - Exposing the Top 10 Myths, SPE 119242, Hydraulic Fracturing Technology Conference, The woodlands, Texas. doi: 10.2118/119242-MS

Patra HP, Adhikari SK, Kunar S (2016) Borehole Geology and Well Logging, In: Groundwater Prospecting and Management. Springer Hydrogeology. Springer, Singapore. doi: 10.1007/978-981-10-1148-1\_5

Pearson CM, Bond AJ, Eck ME and Schmidt JH (1992) Results of Stress Oriented and Aligned Perforating in Fracturing Deviated Wells, SPE 22836, Journal of Petroleum Technology, 44(01): 10–18. doi:10.2118/22836-PA

Perkins TK, Kern LR (1961) Widths of hydraulic fractures, J Pet Tech, 13(9):937–949. doi:10.2118/89-PA

Phelps GD, Stewart G, Peden JM and HeriotWatt U (1984) The Analysis of the Invaded Zones Characteristics and Their Influence on Wireline Log and Well-Test Interpretation, paper SPE 13287, presented at the SPE Annual Technical Conference and Exhibition, Houston, Texas, USA. doi: 10.2118/13287-MS

Plahn SV, Nolte KG, Thompson LG, Miska S (1997) A Quantitative Investigation of the Fracture Pump-In/Flowback Test, paper SPE 30504, presented at the SPE Annual Technical Conference and Exhibition, Dallas, Texas, USA; also in SPE Production & Facilities, 12(01): 20–27. doi: 10.2118/30504-PA

Prats (1961) Effect of Vertical Fractures on Reservoir Behavior - Incompressible Fluid Case, 35th Annual Fall Meeting of SPE, Oct. 2 - 5, 1960, in Denver, SPE 1575-G

Pruess K, Battistelli A (2002) TMVOC-A numerical simulator for three-phase nonisothermal flows of multicomponent hydrocarbon mixtures in saturated-unsaturated heterogeneous media, LBNL-49375, Lawrence Berkeley Laboratory, Berkeley, CA

Rahim Z, AI-Anazi H, AI-Kanaan A, Habbtar A, AI-Omair A, Aramco S et al. (2012) IMPROVED GAS RECOVERY—2 (Conclusion): Productivity increase using hydraulic fracturing—expectation vs. reality, http://www.ogj.com/articles/print/vol-110/issue-5/drilling-production/improved-gas-recovery-2-conclusion-productivity-increase.html, Retrieved 03 June 2017

Rezaee R, Saeedi A, Clennell B (2012) Tight gas sands permeability estimation from mercury injection capillary pressure and nuclear magnetic resonance data, Journal of Petroleum Science and Engineering, 88-89:92-99. doi: 10.1016/j.petrol.2011.12.014

Romero J, Mack M, Elbel J (1995) Theoretical Model and Numerical Investigation of Near-Wellbore Effects in Hydraulic Fracturing, SPE 30506, Annual Technical Conference and Exhibition, Dallas, TX, USA. doi: 10.2118/30506-MS

Roussel NP, Sharma MM (2011) Strategies to minimize frac spacing and stimulate natural fractures in horizontal completions, SPE paper 146104. In: Proceedings of 2011 SPE Annual Technical Conference and Exhibition, 30 October - 2 November, Denver, Colorado, USA. doi: 10.2118/146104-MS

Sajjad N (2013) Structural restoration of Mesozoic rifting phases in the northern North Sea, Petroleum Geosciences, Norwegian University of Science and Technology

Saltelli A. et al. (2008) Global Sensitivity Analysis, The Primer. Chichester, England: John Wiley & Sons, Ltd. ISBN:978-0-470-05997-5

Sampath K, Keighin CW (1982) Factors affecting gas slippage in tight sandstones of Cretaceous age in the Uinta basin, Journal of Petroleum Technology, 34(11):2715-2720

Scheck M, Bayer U (1999) Evolution of the Northeast German Basin - inferences from a 3D structural model and subsidence analysis, Tectonophysics, 313(1-2):145-169. doi: 10.1016/S0040-1951(99)00194-8

Schlumberger (2014) Manual for Petrel E&P Software Platform 2014

Shlyapobersky J, Wong GK, Walhaug WW (1988b) Overpressure Calibrated Design of Hydraulic Fracture Simulations, paper SPE 18194, presented at the SPE Annual Technical Conference and Exhibition, Houston, Texas, USA. doi: 10.2118/18194-MS

Siebrits E, Peirce AP (2002) An efficient multi-layer planar 3D fracture growth algorithm using a fixed mesh, Int. J. For Numerical methods in Engineering, 53(3):691-717. doi: 10.1002/nme.308

Simo H, Pournik M, Sondergeld CH (2013) Proppant crush test: A new approach, paper SPE 164506, presented at the SPE Production and Operations Symposium, Oklahoma city, Oklahoma, USA. doi: 10.2118/164506-MS

Sneddon IN (1946) The distribution of stress in the neighbourhood of a crack in an elastic solid, Proc R Soc, 187:229–60. doi: 10.1098/rspa.1946.0077

Sneddon IN, Elliot AA (1946) The Opening of a Griffith Crack Under Internal Pressure, Quarterly of Appl. Math. 4(3):262 -267

Soliman MY, Craig D, Barko K, Rahim Z, Ansah J, Adams D (2005) New Method for Determination of Formation Permeability, Reservoir Pressure, and Fracture Properties from a Minifrac Test, Paper ARMA/USRMS 05-658

Staff (2013) State by state maps of hydraulic fracturing in US, Fractracker.org. Retrieved 10 May 2017

Starfield AM, Smith KA and Bleloch AL (1990) How to Model It - Problem Solving for the Computer Age, New York, New York, USA, McGraw-Hill. ISBN-10: 0070058970, ISBN-13: 978-0070058972

Taghichian A, Zaman M, Devegowda D (2014) Stress shadow size and aperture of hydraulic fractures in unconventional shales. J. Pet. Sci. Eng. 124:(209–221). ISSN:0920-4105

The Log Analyst (1996) Special Issue on NMR Logging, 37(6)

The Log Analyst (1997) Special Issue on NMR Logging, 38(2)

Thiercelin M, Desroches J, Kurkjian A (1994) Open Hole Stress Test in Shales, Proc., Eurock '94 Symposium, Delft, Netherlands, 921-928. doi: 10.2118/28144-MS

Thiercelin MJ, Plumb RA, Desroches J, Bixenman PW, Jonas JK, Davie WAR (1996) A New Wireline Tool for In-Situ Stress Measurements, Society of Petroleum Engineers, 11(01): 19-25. doi: 10.2118/25906-PA

Tip of the Mitt Watershed Council (2013) Oil and Gas Development Using High Volume Hydraulic Fracturing, https://www.watershedcouncil.org/hydraulic-fracturing.html, Retrieved 04 June 2017

Tittman J and Wahl JS (1965) The Physical Foundations of Formation Density Logging (Gamma/Gamma), Geophysics 30(2). doi: 10.1190/1.1439574

Van Everdingen AF, Hurst W (1949) The Application of the Laplace Transformation to Flow Problems in Reservoirs, Trans., AIME, 1(12):305–324. doi: 10.2118/949305-G

Van Wees JD (2000) On the origin of Southern Permian Basin, Central Europe, Marine and Petroleum Geology, 17 (1): 43–59. doi:10.1016/s0264-8172(99)00052-5

Wang Z (2000) Dynamic versus static elastic properties of reservoir rocks, in Z. Wang, and A. Nur, eds., Seismic and acoustic velocities in reservoir rocks; Volume 3: Recent developments: Geophysics Reprint Series

Ward JS, Morrow NR (1987) Capillary Pressure and Gas Relative Permeabilities of Low-Permeability Sandstone, SPIFE, SPE Paper 13882, 2(03):345-356. doi:10.2118/13882-PA

Wikipedia (2017 1) https://en.wikipedia.org/wiki/North German basin

STDK (2016) (Deutsche Stratigraphische Kommission, Hrsg.; Koordination und Gestaltung: Menning, M. & Hendrich, A.) Stratigraphische Tabelle von Deutschland 2016. – Tafel im B0-Format: 100x141 cm oder Falt-Tafel im A4-Format; Potsdam (Deutsches GeoForschungsZentrum). ISBN:978-3-9816597-7-1

Yew Ching H & Weng X (2015) Mechanics of Hydraulic Fracturing, 2nd Edition. Gulf Professional Publishing. ISBN: 978-0124200036

Zhang K, Yamamoto H, Pruess K (2007) TMVOC-MP: A Parallel Numerical Simulator for ThreePhase Non-isothermal Flows of Multicomponent Hydrocarbon Mixtures in Porous/Fractured Media, Earth Sciences Division - Lawrence Berkeley National Laboratory, Berkeley, CA. LBNL-63827

Zhou L, Hou Michael Z (2013) A new numerical 3D-model for simulation of hydraulic fracturing in consideration of hydro-mechanical coupling effects, International Journal of Rock Mechanics & Mining Sciences, 60:370–380. doi: 10.1016/j.ijrmms.2013.01.006

Zhou L, Hou Michael Z, Gou Y, Li MT (2014) Numerical investigation of a low-efficient hydraulic fracturing operation in a tight gas reservoir in the North German Basin, Journal of Petroleum Science and Engineering, 120:(119-129). doi:10.1016/j.petrol.2014.06.001

Zieger PA (1993) Late Palaeozoic - Early Mesozoic Plate Reorganization: Evolution and Demise of the Variscan Fold Belt, Pre-Mesozoic Geology in the Alps: 203–216

Zoback MD, Moos D, Mastin L and Anderson RN (1985) Wellbore breakouts and in situ stress, - J. Geophys. Res., 90(B7):5523-5530. Paper number:4B1300